

Seismic imaging in complex media with the Common Reflection Surface stack

Dissertation
zur Erlangung des Doktorgrades
der Naturwissenschaften im Department
Geowissenschaften
der Universität Hamburg

vorgelegt von
Mikhail Baykulov
aus Saratov, Russland

Hamburg
2009

Als Dissertation angenommen vom Department Geowissenschaften
der Universität Hamburg

auf Grund der Gutachten von Prof. Dr. Dirk Gajewski

und Dr. Claudia Vanelle

Hamburg, den 22. April 2009

Prof. Dr. Jürgen Oßenbrügge

Leiter des Departments Geowissenschaften

Contents

Abstract	9
Introduction	11
1 Theoretical background	15
1.1 General remarks and assumptions	15
1.2 Conventional CMP stack method	16
1.3 Common Reflection Surface stack	19
1.3.1 Kinematic wavefield attributes	19
1.3.2 CRS stacking procedure	22
1.4 NIP-wave tomography	26
1.4.1 Data and model components	26
1.4.2 Inverse problem	28
1.4.3 Inversion algorithm	29
1.4.4 Picking and editing of input data	30
1.5 Depth migration	32
1.5.1 Migration basics	32
1.5.2 Depth migration as diffraction summation	34
1.5.3 Kirchhoff depth migration	34
1.5.4 Practical aspects	38
2 Marine data example	43
2.1 Study area and acquisition geometry	43
2.2 Preprocessing	46
2.3 CRS processing	47
2.3.1 Automatic CMP stack	47
2.3.2 Automatic CRS stack	51
2.3.3 NIP-wave tomographic inversion	54
2.4 Depth migration	62
2.4.1 Poststack depth migration of the CRS stack	63
2.4.2 Prestack depth migration	64
2.5 Conclusions	64

3	Land data example	69
3.1	Study area and acquisition geometry	70
3.2	Preprocessing	71
3.3	CRS processing	74
3.3.1	Automatic CMP stack	74
3.3.2	Automatic CRS stack	75
3.3.3	NIP-wave tomographic inversion	80
3.4	Depth migration	83
3.4.1	Poststack depth migration of the CRS stack	86
3.4.2	Prestack depth migration	88
3.5	Conclusions	88
4	Partial CRS stack	93
4.1	Basic idea of partial CRS stacks	94
4.2	Calculation of partial CRS stacking surface	96
4.3	Synthetic data tests	97
4.3.1	Noise-free Sigsbee 2A dataset	97
4.3.2	Sigsbee 2A data with sparse traces	99
4.3.3	Sigsbee 2A data with noise	101
4.4	Application to land data and depth migration	106
4.4.1	PreSDM of CRS supergathers	106
4.5	Discussion and Conclusion	113
5	Summary and Outlook	115
5.1	Summary	115
5.2	Outlook	116
	Used software	119
	Acknowledgements	121
	References	123
	Erklärung	127
	Curriculum Vitae	129

List of Figures

1.1	Reflection seismic geometry	17
1.2	CMP stacking scheme	18
1.3	CRS stacking surface	20
1.4	Physical interpretation of the CRS stacking parameters	21
1.5	CRS stacking operator	25
1.6	Ray trajectories associated with a CRP and NIP points	26
1.7	Data and model components for the NIP-wave tomography	28
1.8	Quality control of input points for the NIP-wave tomography	31
1.9	Geometrical principle of migration	33
1.10	Diffraction summation method for a horizontal reflector	35
1.11	Flat common image gathers after PreSDM	41
1.12	Common image gathers after prestack depth migration	41
2.1	Marine data: study area	44
2.2	Marine data: generalised stratigraphic chart	45
2.3	Marine data: examples of CMP gathers	47
2.4	Marine data: stacking velocity model	48
2.5	Marine data: automatic CMP stack	50
2.6	Marine data: automatic CRS stack	52
2.7	Marine data: zooms of the salt plugs	53
2.8	Marine data: CRS semblance section	55
2.9	Marine data: angle of emergence, α	55
2.10	Marine data: radius of curvature of the NIP-wave, R_{NIP}	56
2.11	Marine data: radius of curvature of the N-wave, R_N	56
2.12	Marine data: number of traces used by the automatic CMP and CRS stacks	57
2.13	Marine data: input picks for NIP-wave tomography	59
2.14	Marine data: quality control of input picks for NIP-wave tomography	60
2.15	Marine data: depth velocity models after different tomographic iterations	61
2.16	Marine data: cost function	61
2.17	Marine data: final depth velocity model	65
2.18	Marine data: poststack depth migration of the CRS stack	66
2.19	Marine data: Kirchhoff prestack depth migration	67
2.20	Marine data: common image gathers	68

3.1	Land data: study area	71
3.2	Land data: examples of CMP gathers	72
3.3	Land data: stacking velocity model	73
3.4	Land data: automatic CMP stack	76
3.5	Land data: automatic CRS stack	76
3.6	Land data: zooms of the salt plug	77
3.7	Land data: CRS semblance section	78
3.8	Land data: angle of emergence, α	78
3.9	Land data, radius of curvature of the NIP-wave, R_{NIP}	79
3.10	Land data: radius of curvature of the N-wave, R_N	79
3.11	Land data: number of traces used by automatic CMP and CRS stacks	80
3.12	Land data: input picks for NIP-wave tomography	81
3.13	Land data: quality control of input picks for NIP-wave tomography	82
3.14	Land data: depth velocity models after different tomographic iterations	84
3.15	Land data: cost function	84
3.16	Land data: final depth velocity model	85
3.17	Land data: poststack depth migration of the CRS stack	87
3.18	Land data: Kirchhoff prestack depth migration	87
3.19	Land data: zooms of the salt plug	89
3.20	Land data: common image gathers	90
4.1	Partial CRS stacking surface	95
4.2	Partial CRS stack: tested hyperbolas	98
4.3	Sigsbee 2A data: the true interval velocity model and a CMP gather	99
4.4	Sigsbee 2A data: CRS parameter sections	100
4.5	Sigsbee 2A sparse data: CMP gather and CRS supergather	102
4.6	Sigsbee 2A sparse data: zooms of the CMP gather and the CRS supergather.	102
4.7	Sigsbee 2A sparse data: conventional CMP stack and CRS supergather stack	103
4.8	Sigsbee 2A data with noise: CMP gather and CRS supergather	104
4.9	Sigsbee 2A data with noise: zooms of the CMP gather and the CRS supergather	104
4.10	Sigsbee 2A data with noise: conventional CMP stack and CRS supergather stack	105
4.11	Land data: CMP bins and partially stacked CRS supergather	107
4.12	Land data: zooms of the CMP gather and the CRS supergather	108
4.13	Land data: conventional CIGs vs CIGs of CRS supergathers	109
4.14	Land data: zooms of conventional CIGs vs CIGs of CRS supergathers	110
4.15	Land data: PreSDM section of CRS supergathers	110
4.16	Land data: conventional PreSDM section in the salt plug area	111
4.17	Land data: PreSDM section of CRS supergathers in the salt plug area	111
4.18	Land data: comparison of depth migrations	112
4.19	Land data: CIGs of CRS supergathers	113

List of Tables

2.1	Marine data: acquisition parameters.	44
2.2	Marine data: CRS parameters.	49
2.3	Marine data: parameters of the NIP-wave tomographic inversion.	60
2.4	Marine data: processing parameters for depth migration.	63
3.1	Land data: acquisition parameters.	70
3.2	Land data: CRS parameters.	74
3.3	Land data: parameters of the NIP-wave tomographic inversion.	83
3.4	Land data: processing parameters for depth migration.	86
4.1	Sigsbee 2A data: CRS parameters.	99

Abstract

Reflection seismic is one of the most commonly used geophysical method for the oil and gas exploration. In this thesis I show the application of the Common Reflection Surface (*CRS*) stack technique to improve the quality of reflection seismic images. Conventional seismic imaging method based on the CMP stacking does not use the full potential of the dataset due to reflection point dispersal in the presence of dipping reflectors or laterally inhomogeneous media. Application of the CRS stack technique is advantageous in complex areas, since it involves information about the shape of seismic reflectors, i.e., dip and curvature, into processing. Moreover, a multiparameter formula allows to sum up more traces during the stack. All together, this leads to better imaging results, especially to an improvement of the signal-to-noise (S/N) ratio. Reflection events in the CRS stack sections appear clearer and more continuous compared to conventional CMP stack sections.

In two case studies I demonstrate the strength of the CRS stack technique applied to seismic reflection data of different quality. First, I apply the CRS stack method to a high-quality marine seismic data from the North Sea. This part of the thesis gives the overview of the typical CRS processing flow and shows the results of time and depth imaging.

Then, I perform the CRS stack processing on low-quality land data from Northern Germany. The potential of this dataset was not fully exploited by the conventional CMP stacking method. The CRS stack section shows new details, especially in the internal structural of the salt plugs that were not identified using conventional processing. Moreover, the CRS stack parameters obtained during the automatic search form the foundation for a robust reflection tomography for velocity model building. The obtained depth velocity model allows the prestack and poststack depth migration in the areas of the salt plugs. Resulting depth sections were previously not available for this dataset. They provide supplementary information for the geological interpretation. However, the CRS stack improves only the quality of the stacked sections. To provide a reliable control of migration velocities, and to generate an improved prestack depth migrated section, the S/N ratio and the regularity of input seismograms should be enhanced before prestack depth migration.

In this thesis I present the new **partial CRS stack** method, which allows to improve the quality of prestack seismic reflection data. The method is based on the multiparameter CRS traveltimes

formula, and uses the results of the automatic CRS stack. I introduce a method of effectively searching the partial CRS stacking operator. The algorithm is robust and easy to implement. The partial CRS stack uses the information about local dip and curvature of each reflector element, and sums up the amplitudes of all traces contributing to that element. The true reflector is locally approximated by the reflection surface. Depending on the chosen size of the surface, the number of traces used during the partial stacking may vary. Due to the constructive summation of coherent events, the partial CRS stack enhances the signal and attenuates random noise. Moreover, missing traces (e.g., acquisition gaps) can be generated and the acquisition can be regularised, if the approximating surface contains useful events from neighbouring traces. The latter can be considered as an improved interpolation technique using a simple and robust summation algorithm. This also allows generating regular traces with equidistant intervals, which may be helpful for further processing of the data, e.g., by wavefield methods. Partially-stacked CRS supergathers are superior to conventional CMP gathers in areas of complex geological behaviour. They are regularised and have a higher S/N ratio compared to the original seismograms. Reflections in CRS supergathers appear clearer and continuous, which is preferable for the velocity analysis and quality control of depth migration.

To test the potential of the partial CRS stack, I show two examples using synthetic data. Then, I apply the method on the real land dataset from Northern Germany. The results demonstrate the improvement of seismic images and provide the quality control of the depth migration, which was hardly possible using the conventional image gathers.

Introduction

The aim of this thesis is to provide a method for improvement of seismic reflection images in complex geological environments. Reflection seismic is one of the most commonly used geophysical method for the oil and gas exploration. It allows to image subsurface structures using indirect measurements carried out at the Earth's surface. A detailed image of the Earth's interior is the goal of investigations for academic research and for the oil and gas industry. Consistent images provided by the reflection seismic method help geologists to position exploration and production oil wells.

During reflection seismic measurements, energy in form of elastic waves generated by a source propagates into the subsurface. When a wave reaches a seismic boundary, characterised by a change of elastic parameters, it is partly transmitted and partly reflected. The reflected waves can be measured at the surface. Seismic data is usually acquired by receivers at the free surface (or by streamer in marine seismic), and is recorded in form of seismograms.

A main objective of seismic data processing is to transform the acquired data into the best possible image of the subsurface. Since the information about the elastic waves is recorded as amplitudes of seismic signal as a function of recording time, the first view on the subsurface structures can be performed by the interpretation of time sections. In a two-dimensional (2D) seismic survey the sources and receivers are placed along a profile line. In a horizontally-layered medium each subsurface point is repeatedly illuminated by a number of rays travelling from sources to receivers under varying angles. This so-called multi-coverage seismic recording provides redundant information about the illuminated subsurface points. During the processing this redundancy is used to produce the stacked sections, where each trace is the result of summation of many traces illuminating the same reflection points. As a result of constructive summation the amplitudes of signals in stacked traces are enhanced and the random (or incoherent) noise present in the data is attenuated.

An important part of seismic processing is the estimation of propagation velocities of seismic waves from the acquired data. Stacking velocities derived from the seismograms are used to simulate a seismic section, where source and receiver positions are coincident, which is called

the zero-offset (ZO) section. The generation of the ZO section is usually one of the early steps in the seismic processing routine. It provides a first image of the subsurface structures.

A conventionally applied method for simulating the ZO sections is the common midpoint (CMP) stack, formerly known as the Common Reflection Point stack (Mayne, 1962). This approach sums up the amplitudes of reflection events corresponding to midpoints between source and receivers. If the subsurface consists of the horizontally-layered boundaries, the CMP stack assigns the results of summation to common reflection points on a reflector, thus increasing the signal and attenuating the random noise. However, for dipping layers a summation of the CMP gathers would involve reflection energy originating from different subsurface points due to *reflection point dispersal* along a reflector interface (e.g., Yilmaz, 2001). This effect is conventionally corrected by using the dip moveout (DMO) process. Stacking of DMO-corrected CMP gathers yields a section that is a closer approximation to a ZO section than a conventional CMP-stacked section (Yilmaz, 2001).

Modern methods of stacking have been developed in the last decades to overcome the problem of dipping layers and to produce better imaging results. The Common Reflection Surface (CRS) stack (e.g., Müller, 1999; Jäger et al., 2001; Mann, 2002) and Multifocusing (e.g., Landa et al., 1999; Gurevich and Landa, 2002; Berkovitch et al., 2008) are superior to the conventional CMP stack since they include information about the reflector shape during the stacking. Instead of one unknown parameter, which is the stacking velocity in the CMP method, these new approaches operate with three parameters in the two-dimensional (2D) case, describing position, dip and curvature of reflector elements. Additionally, more traces are involved in the stacking process compared to the CMP stack, thus increasing the signal-to-noise (S/N) ratio of the stacked sections. Müller (1999) has shown, that in complex media the CRS stack approximates traveltimes of seismic reflection data more precisely than the NMO/DMO stack, thus improving the stacking results. Only when the shape of the true subsurface reflector is identical to the shape of the specific ZO isochrone, the NMO/DMO stack operates identical to the CRS stack (e.g., Müller, 1999; Jäger et al., 2001). The estimation of the CRS stacking parameters is carried out in an automatic mode with moderate human interaction; only the range of tested values and thresholds must be specified. The CRS stack method is particularly suited for improvement of quality of time stacks of irregular and noisy data. Successful application of the CRS stack method on real data has been demonstrated, e.g., by Pruessmann et al. (2004), Eisenberg-Klein et al. (2008), Pruessmann et al. (2008), Yoon et al. (2008a,b) and Baykulov et al. (2009).

Stacking parameters obtained during the automatic CRS stack provide a basis for the estimation of a depth velocity model consistent with the acquired data. Duveneck (2004) implemented the *NIP-wave tomographic inversion* to estimate a depth velocity model using the results of the automatic CRS stack. This inversion algorithm provides a smooth depth velocity model of the subsurface suitable for a conversion of data from the recorded (time) into the depth domain (*depth migration*).

Depth migration using a consistent velocity model corrects the effect of wave propagation through the medium and provides depth images, where reflectors are at their true positions (e.g., [Yilmaz, 2001](#); [Stolt, 2002](#)). Among the different existing migration classifications, one of the most important is the division into migration after stack and migration before stack. Depth migration after stack (poststack depth migration, *PostSDM*) operates on a simulated time-stacked section. This approach is quite fast and easy to implement, but provides errors in positioning of reflectors in case of strong lateral velocity variations in the media. On the contrary, prestack depth migration (*PreSDM*) operates on the seismograms before the simulation of a stacked section. Stacking of traces by the *PreSDM* is performed after the migration of seismograms. Lateral velocity variations are taken into account by migration, and reflectors are moved to their original position. Moreover, prestack depth migrated gathers, also referred to as Common Image Gathers (*CIG*), provide a quality control for a depth velocity model used by migration. If the velocities used by migration are consistent with the data, reflectors appear at the same depth flat and horizontal in the considered *CIGs*. If the velocities used by migration are too high or too low, the corresponding reflectors in the *CIGs* are not flat.

Migration of seismic data with very low quality, however, produces *CIGs* where reflector elements can be hardly identified. To overcome this problem, the S/N ratio and the regularity of traces should be improved before prestack depth migration. I, therefore, present a partial CRS stack method, which allows to improve the quality of prestack seismic reflection data. The method is based on the CRS traveltime formula and uses the kinematic wavefield attributes obtained during the automatic CRS stack. So far, the CRS stack was applied to improve the quality of stacked sections only. My strategy performs a partial stacking of recorded data beyond the generation of a stacked section. Partial CRS stacks simulate a new dataset where each trace is a result of the summation of several traces corresponding to one reflection element at an interface. Due to the summation of coherent energy the signal is enhanced and the random noise is attenuated. During the summation, information about the local reflector shape is taken into account, thus improving the results of partial stacking.

In the partially-stacked *CRS supergathers* reflections appear more continuous and can be easier identified compared to the conventional CMP gathers. Moreover, the simple summation algorithm allows to simulate traces at any position between the existing seismograms. Therefore, the method can regularise irregularly acquired traces, e.g., in areas of complex surface topography, close to production platforms, rivers, or other areas where data can not be acquired. Due to the simple summation used by the generation of *CRS supergathers* the partial CRS stack is very robust in the presence of incoherent noise. The S/N ratio of the prestack seismograms increases significantly by the partial summation of traces.

Since the partial CRS stack is applied before the generation of a ZO section, the resulting *CRS supergathers* can be used in conventional data processing instead of original CMP gathers. For example, usage of *CRS supergathers* instead of low-quality irregular data significantly improves the results of prestack depth migration. In many cases reflectors that were not visible using the

conventional CIGs can be identified in depth migrated CRS supergathers. This further improves the quality control of migration velocities based on the flatness of gathers.

To test the partial CRS stack method, I apply it on a synthetic dataset. I show the application of this approach on real data case study. The results show the potential of the new method to increase the S/N ratio of noisy data and the regularity of traces.

The thesis is structured as follows:

Chapter 1 reviews the conventional and new seismic imaging techniques used in this work. In particular, it introduces the CMP and CRS stack methods for time imaging, NIP-wave tomography for velocity model building, and depth migration.

Chapter 2 shows the results of the application of the CRS stack for time and depth imaging of high-quality marine seismic data from the Southern part of the North Sea. The area is characterised by complex salt tectonics. Time and depth stacked sections as well as the depth velocity model are the results of the processing. This chapter discusses the practical aspects of processing with the CRS stack.

Chapter 3 demonstrates the results of CRS stack re-processing on old low-fold land data from salt-rich areas of Northern Germany. Depth migration using the estimated NIP-wave tomography model provides depth images that were not available for the dataset before. The results contribute to the special project of the German Research Foundation (DFG) within the priority program SPP 1135 "Dynamics of Sedimentary Systems" ([Bayer et al., 2008](#)).

Chapter 4 introduces the new partial CRS stack method for the improvement of prestack data quality and describes the algorithm of stacking. In the first part numerical tests show the application of the method to synthetic data. The second part describes the application of the new approach to the real land dataset introduced in Chapter 3.

Chapter 5 summarises the results of the thesis and gives an outlook for promising future work with the partial CRS stack method.

Chapter 1

Theoretical background

1.1 General remarks and assumptions

This chapter overviews conventional and modern methods of seismic imaging. In the theoretical description of the thesis the following assumptions and approximations are made:

- **2D case.** Seismic imaging is in general a three-dimensional (*3D*) problem since the seismic waves propagate in three spatial dimensions simultaneously. However, the datasets used in this thesis were recorded using 2D acquisition profiles, i.e., the sources and receivers were placed along lines. Therefore, the theoretical descriptions of the seismic imaging method in this chapter is restricted to the 2D case only. This requires the assumption that the deviations of the seismic profiles from the straight lines are minor and that the elastic properties of the subsurface do not vary transversely to those lines. Nevertheless, one should always bear in mind that real 2D data can also contain events coming from outside of profile lines (so-called *out-of-plane* events). Obviously, neglecting these events may lead to errors during the interpretation of the results. The interpretation of seismic events was, however, not the main target of this thesis. The aim was the improvement of seismic images, assuming that there are no events generated from the directions perpendicular to the profile lines.
- **P-waves.** In the thesis I consider only the propagation of compressional waves; shear-waves are not taken into account. Anisotropic effects, i.e., the variations of properties of a material in different directions, are also not considered.
- **Hyperbolic approximation.** Throughout the thesis the hyperbolic second-order approximation of reflection traveltimes is used since it provides both the simplicity of calculations and suf-

ficient accuracy for most seismic data. This assumption, however, fails in complex areas with very strong velocity variations for long source-receiver offsets. Approximations of traveltimes of higher orders and ray tracing method (Červený, 2001) could be used to improve the results of imaging in these situations.

1.2 Conventional CMP stack method

In 2D seismic data acquisition sources and receivers are distributed along a line (e.g., Mayne, 1962; Sheriff and Geldart, 1995; Yilmaz, 2001). In the field, seismic data are acquired as common source (CS) gathers and later sorted into common midpoint (CMP) gathers. The CMP is defined as the midpoint between a source and a receiver. Its location on the seismic line is calculated from the source location S and the receiver location G by $(S + G)/2$. The distance between a receiver and a source is called *offset*. Often the half offset $h = (G - S)/2$ is used instead.

For a horizontally layered medium with constant velocity the reflections spread over an area of the reflector in a CS gather (see Figure 1.1(a)). A CMP gather includes all rays that illuminate the same point on a reflector (see Figure 1.1(b)), but have different offsets. Thus, a CMP gather contains redundant information about the subsurface. This is the basic idea for the CMP stack method (Mayne, 1962). Since the traces from different offsets contain information for a common point of the horizontal reflector, the redundant information can be summed up constructively to generate a stacked section of higher S/N ratio.

In a CMP gather, reflection events appear as a set of time responses aligned along a moveout curve (see, e.g., Yilmaz, 2001). Conventional CMP stacking involves summing the primary reflections along the calculated moveout curves which best approximate the actual reflection traveltimes. For small offsets the traveltimes are approximated by a hyperbolic formula (Hubral and Krey, 1980):

$$t^2(h, V_{NMO}) = t_0^2 + \frac{4h^2}{V_{NMO}^2}, \quad (1.1)$$

where t is the time of wave propagation from source to receiver, h is half-offset, t_0 is zero-offset traveltimes, i.e., the traveltimes measured for coincident source and receiver ($h = 0$), and V_{NMO} is the *moveout (or NMO) velocity*. For a single dipping layer the NMO velocity is given by

$$V_{NMO} = \frac{V}{\cos \phi}, \quad (1.2)$$

where V is the medium velocity and ϕ is the dip angle of the reflector. For several layers with arbitrary dips the definition of the NMO velocity becomes more complex. It depends on model parameters such as reflector positions and interval velocities.

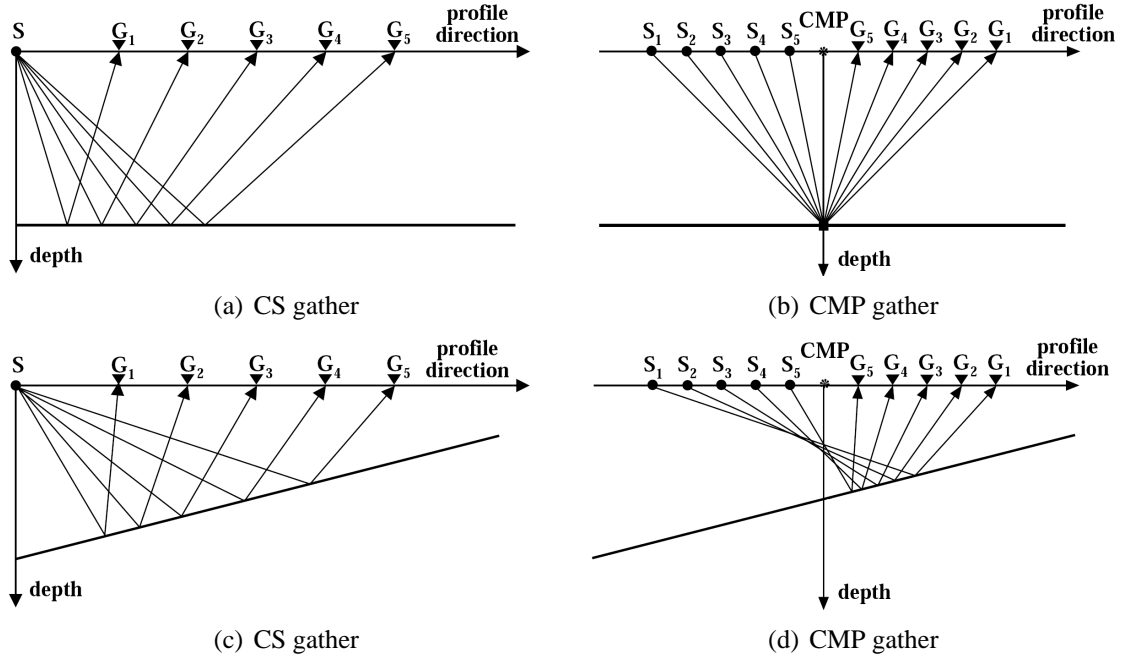


Figure 1.1: Reflection seismic geometry. The figure displays a common source (a, c) and a common midpoint (b, d) gather for the same profile. In a homogeneous and horizontally-layered model, all rays in a CMP gather reflect from the same depth point under varying angles. If a coincident source and receiver location exists in the acquisition geometry, a CMP gather contains a zero-offset ray that originates from the coinciding source-receiver pair at the CMP location (b). In a model with a dipping reflector one CMP gather contains rays reflected from different points on a reflector (d).

The hyperbolic approximation given by equation 1.1 should be distinguished from the formula providing the best stacking result:

$$t^2(h, V_{st}) = t_{0st}^2 + \frac{4h^2}{V_{st}^2}, \quad (1.3)$$

where V_{st} is the *stacking velocity* that allows the best fit of the traveltime trajectory on a CMP gather to a hyperbola within a spread length (Yilmaz, 2001). The optimum stacking hyperbola described by equation 1.3 is not necessarily the small-spread hyperbola given by equation 1.1. The two-way time t_{0st} associated with the best-fit hyperbola can be different from the observed two-way ZO time in equation 1.1. The difference between the stacking velocity and the NMO velocity is called *spread-length bias* (Hubral and Krey, 1980). From equations 1.1 and 1.3 follows that the smaller the half-offset h , the smaller the difference between V_{NMO} and V_{st} . In practice, when we refer to stacking velocity, we approximate it by the NMO velocity associated with the hyperbola given by equation 1.1.

For CMP stacking the NMO correction must be applied to the seismograms. NMO correction involves mapping non-zero offset traveltime t onto zero-offset traveltime t_0 . The hyperbolic

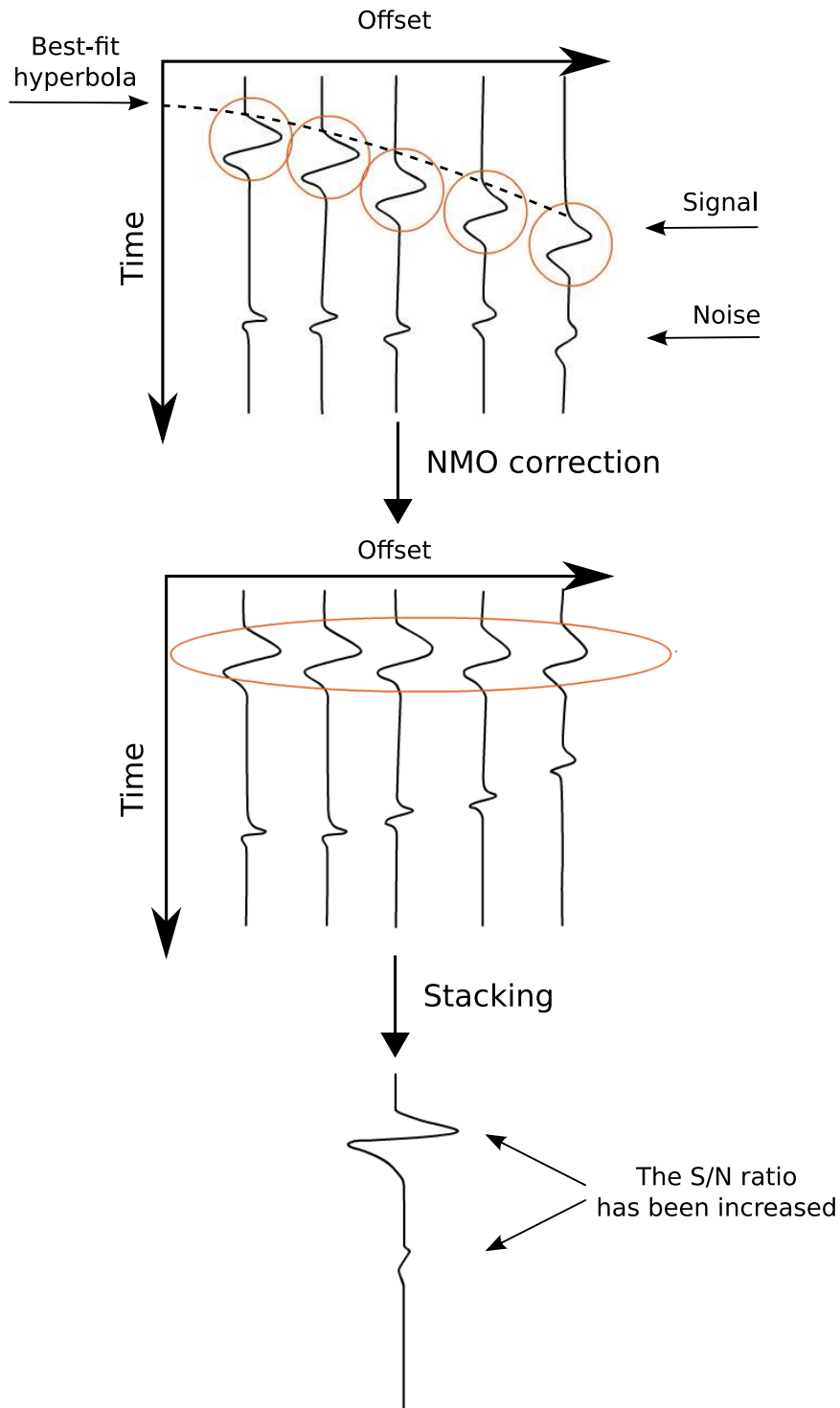


Figure 1.2: CMP stacking scheme. A stacking velocity analysis algorithm is applied to determine best-fit hyperbolas for reflection events in exemplarily chosen CMP gathers. Then, the NMO correction is applied to the seismograms, and the reflection becomes straightened. Summation of traces generates one stacked trace, where the signal is enhanced, and the noise is attenuated, i.e., the S/N ratio is increased.

traveltime curve defined by Equation 1.1 depends only on one unknown parameter – V_{NMO} . Velocity analysis algorithms allow to estimate this velocity from recorded data (either automatic or manually) without a priori knowledge. Standard velocity analysis applies NMO corrections to the CMP gathers with several velocity values in a given range, and finds the one velocity that best fits the moveout of the events. After the application of the NMO correction with the appropriate stacking velocity, the CMP gathers become straightened and can be summed to generate one ZO trace in a CMP stacked section (see Figure 1.2).

If the subsurface geometry is complex, the optimum stacking velocity depends on the shape of reflectors. Figures 1.1(c) and 1.1(d) show an example of a dipping layer model with a constant velocity. The source-receiver pairs (Figure 1.1(d)) having a common midpoint do not share the same common reflection point as in Figure 1.1(b). The reflection points are variable: they are shifted up-dip with increasing offset (*reflection point dispersal*) and distributed over the interface. Therefore, the CMP stacking involves reflection energy originating from different subsurface points, decreasing the quality of stacking (Yilmaz, 2001). This effect in time sections is conventionally corrected using the DMO process (e.g., Yilmaz, 2001). Alternatively, multiparameter stacking techniques developed in the last years can be used for better time stacking in case of dipping layers.

In this thesis, I use the Common Reflection Surface (CRS) stack for generating time sections of complex geological areas like the salt dome areas from Northern Germany. Müller (1999) has shown that the CRS stack, where the dip of reflector is incorporated, approximates the traveltimes of seismic reflection data better than the NMO/DMO stack in complex areas. Only for the rare case when the shape of the true subsurface reflector is identical to the shape of the specific ZO isochrone, the NMO/DMO stack describes the data identical to the CRS stack (e.g., Müller, 1999; Jäger et al., 2001).

1.3 Common Reflection Surface stack

1.3.1 Kinematic wavefield attributes

The CRS stack is a multi-parameter stacking technique (Müller, 1999; Jäger et al., 2001; Mann, 2002). The CRS stacking surface (see Figure 1.3) can be calculated using the approximation of the true subsurface reflector by a reflector element that locally has the same curvature as the true reflector. The traveltime t of reflection events is described by three parameters α , R_N and R_{NIP} in a hyperbolic formula:

$$t^2(m, h, P) = \left(t_0 + \frac{2 \sin \alpha}{V_0} m\right)^2 + \frac{2t_0 \cos^2 \alpha}{V_0} \left(\frac{m^2}{R_N} + \frac{h^2}{R_{NIP}}\right), \quad (1.4)$$

where h is half source-receiver offset, m is midpoint distance with respect to the considered CMP position, t_0 is the zero offset (ZO) two-way traveltimes (TWT) and $P = (\alpha, R_N, R_{NIP})$ defines the shape of the stacking surface. In the following text, the parameter triplets $(\alpha, R_N$ and $R_{NIP})$ are referred to as the *CRS parameters*.

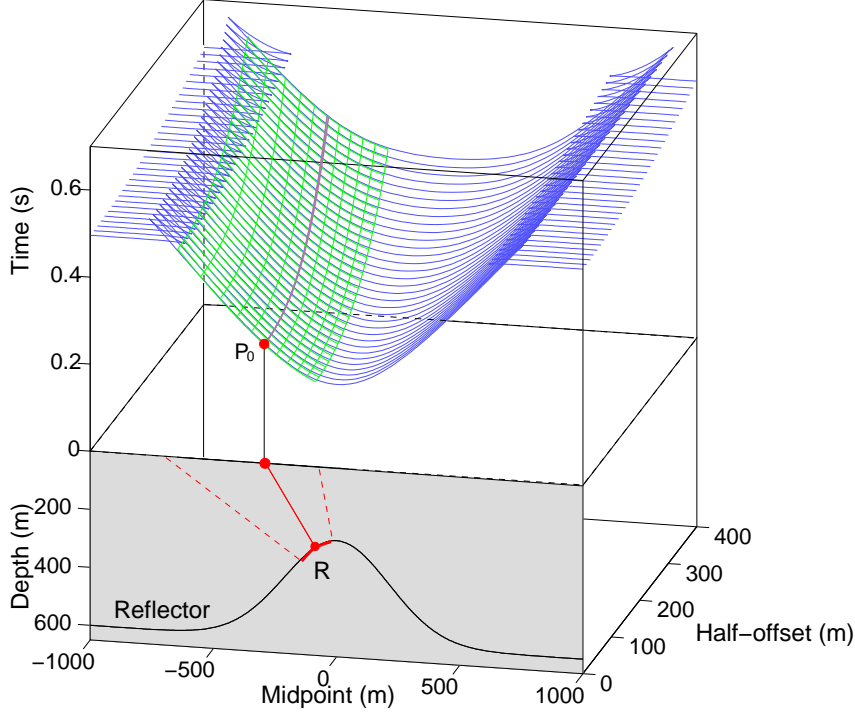


Figure 1.3: CRS stacking surface for a constant velocity 2-dimensional medium in a midpoint-offset-time (m, h, t) domain. The blue curves are the common-offset time responses of the curved subsurface reflector. The stacking surface results from approximating the true reflector by a reflector segment R that locally has the same curvature as the true reflector. The CRS stack sums the data along the green surface that coincides locally with the common-offset time response of the reflector, and assigns the result to the point $P_0 = (x_m, t_0)$, where x_m is the CMP coordinate and t_0 is the ZO traveltimes. Defined by the width of stacking surface in midpoint direction, the CRS involves more traces during the stacking compared to conventional CMP stack (magenta line).

In equation 1.4, α is the angle of emergence of the ZO ray, V_0 is the near surface constant velocity that has to be known, R_N and R_{NIP} are radii of curvature of the normal (N) wave and normal-incidence-point (NIP) wave, respectively. The N - and NIP -waves are generated by two hypothetical one-way experiments (see Hubral, 1983). The NIP -wave can be considered as a wave that propagates from a point source at the NIP for a specific reflector. The N -wave is a wave generated by an exploding reflector model, where dense point sources cover the common-reflector-surface (CRS) around the NIP and explode simultaneously. R_{NIP} can be associated with the distance from the reflector element to the observation surface, and R_N is a measure for the CRS 's curvature (Figure 1.4). However, for complex subsurface geometries, the true depth and

curvature of the reflector element deviate significantly from the measured R_N and R_{NIP} . Correct reflector positions can be reconstructed only by performing a seismic inversion procedure, e.g. using the NIP-wave tomography implemented by [Duveneck \(2004\)](#). From this point of view, the parameters (α, R_N, R_{NIP}) describe the kinematic properties of two hypothetical waves, and are often referred to as the *kinematic wavefield attributes*.

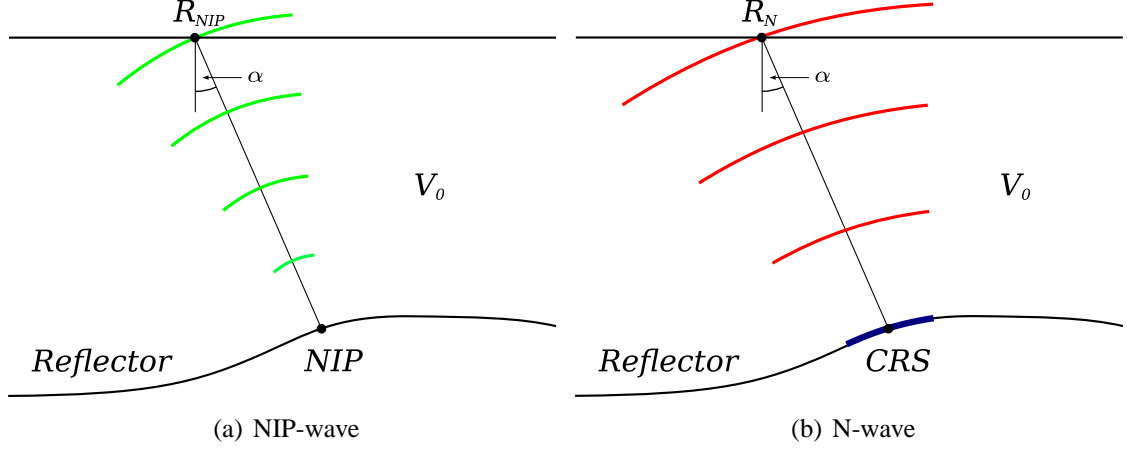


Figure 1.4: Physical interpretation of the CRS stacking parameters for a constant velocity model. The angle of emergence, α , defines the angular orientation of the CRS (blue colour). The radius of curvature of the NIP-wave (a) gives the distance from the NIP to the surface, while the radius of curvature of the N-wave (b) is a measure for the CRS curvature.

The CRS stack sums up amplitudes of all traces over the calculated CRS stacking surface, and assigns the result of summation to the considered ZO traveltimes of a stacked trace. Depending on the given maximum midpoint distance m from the considered CMP location, the CRS stacking surface (green grid in Figure 1.3) contains a larger number of traces than the number of traces used during the conventional CMP stack (magenta line in Figure 1.3). The choice of m is important for the resulting lateral resolution of the following processing results. The size of the first projected Fresnel zone that is an intersection of the first Fresnel volume with the reflector is a good guidance for m , which can be interpreted as the lateral extension of the stacking operator ([Mann, 2002](#)). The width of the first projected Fresnel zone can be estimated using the CRS parameters. However, the CRS parameters of seismic reflection data are initially unknown, and need to be found. Therefore, the first guess about the aperture size is usually made using the geological information available for the area of interest. Then, the automatic CRS parameter search provides all necessary information for updating the estimated width of the Fresnel zone. The halfwidth of the first projected Fresnel zone is calculated by

$$F_{HW} = \frac{1}{\cos \alpha} \sqrt{\frac{V_0}{2w \left| \frac{1}{R_{NIP}} - \frac{1}{R_N} \right|}}, \quad (1.5)$$

where w is the dominant frequency of the seismic signal. The CRS stack software updates the result of stacking using the aperture derived by equation 1.5. It follows from the geometry of

the CRS stacking surface, that the midpoint aperture defines the number of neighbouring CMP gathers used during the stacking to generate one ZO trace. However, if the maximum midpoint displacement m is set to zero, the stacking surface reduces to only one CMP, and equation 1.4 transforms into the classical CMP stacking formula (see the following section, equation 1.7).

1.3.2 CRS stacking procedure

To perform the stacking of seismic reflection data using the equation 1.4, the CRS parameters must be estimated. A simultaneous 3-parameter search for (α, R_N, R_{NIP}) would be computationally very expensive. The implementation of Jürgen Mann, used in this thesis, is based on three independent one-parameter searches, with the possibility of further optimisation of stacking parameters (Mann, 2002). Starting with the generation of an automatic CMP stack section, the parameters α , R_N and R_{NIP} are estimated step by step.

Automatic CMP stack

The first step in the search strategy is the generation of the automatic CMP stacked section. This procedure is similar to conventional CMP stacking, where the stacking velocities are picked manually with respect to highest coherence values between calculated hyperbolas and recorded data. The CRS stack uses the same criterion, i.e., the highest coherency value, but performs the picking automatically. For this reason, the simulated ZO section is referred to as the *automatic CMP stack*. The stacking trajectory is obtained by restriction of the CRS stacking surface to one CMP gather, i.e., by setting m to zero in equation 1.4:

$$t^2(m = 0, h, \alpha, R_{NIP}) = t_0^2 + \frac{2t_0 \cos^2 \alpha}{V_0} \frac{h^2}{R_{NIP}}. \quad (1.6)$$

Equation 1.6 can be written as

$$t^2(h, V_{NMO}) = t_0^2 + \frac{4h^2}{V_{NMO}^2}, \quad (1.7)$$

with the stacking velocity defined by

$$V_{NMO} = \sqrt{\frac{2V_0 R_{NIP}}{t_0 \cos^2 \alpha}}. \quad (1.8)$$

Therefore, equation 1.7 is the standard CMP formula, which is identical to equation 1.1, but the stacking velocity is written in terms of V_0 , α and R_{NIP} . This means that the CMP stack is a

special case of the CRS stack with the maximum midpoint aperture $m = 0$. In other words, the CRS stack is an extension of the CMP stacking in the lateral (m) direction.

Using equation 1.7 the CRS stack determines stacking velocities automatically for every time sample in the output ZO section. A discrete number of stacking velocities is tested. Each one defines a hyperbola in the CMP gather that is correlated with the prestack data. The velocity that yields the highest coherency between the calculated hyperbola and recorded data is stored as an initial value. The summation of prestack data along the defined hyperbola into the corresponding ZO time samples yields an automatic CMP stack section.

The automatic CRS stack method sums up all coherent events that can be described by the CRS parameters, among others multiples. In conventional manual velocity analysis, velocities of primaries are picked while the multiples are ignored. Since traveltimes of long-term multiples deviate significantly from traveltimes of primaries, they are easily identified in coherency stacks. Since apparent velocities of multiples are lower than velocities of primary events at a considered traveltime, the multiples become *undercorrected* after the NMO-correction with the proper velocity while the primaries become flat. By CMP stacking, summation of flat events will enhance flat primaries, and destructive summation will attenuate undercorrected multiples. If multiples can be described by the hyperbolic moveout formula 1.7, the automatic CMP stack will also find stacking parameters for these multiples. It is possible that the automatic algorithm will stack multiples instead of primaries if the coherence of multiples is higher at the considered traveltime.

However, the searching procedure can be constrained in order to suppress multiples during the automatic CMP stack. For this purpose, the automatic CMP stack uses a reference model of stacking velocities. Either a simple table of guide velocity values or the stacking velocity model obtained from conventional NMO analysis can be used as a reference to build a constrained velocity function. A given time-dependent window defines the maximum allowed deviation of estimated velocity values from the guide values. Velocity analysis during the automatic CMP stack is, therefore, constrained, and the multiples are attenuated by destructive summation like in the conventional CMP stack.

CRS parameter search

After the generation of the automatic CMP stack section, the CRS stack performs a parameter search using the zero-offset approximation of the CRS traveltime formula. Setting the half-offset h to zero, equation 1.4 reduces to

$$t^2(m, h = 0, \alpha, R_N) = \left(t_0 + \frac{2 \sin \alpha}{V_0} m \right)^2 + \frac{2 t_0 \cos^2 \alpha}{V_0} \frac{m^2}{R_N}. \quad (1.9)$$

This traveltime formula depends only on two unknown parameters α and R_N . In short-offset approximation equation 1.9 can be further simplified to yield a one-parametric equation, setting $R_N = \infty$ (Müller, 1999):

$$t_{par}(m, \alpha) = t_0 + \frac{2\sin\alpha}{V_0}m. \quad (1.10)$$

This equation depends only on the unknown angle of emergence α . Using equation 1.10, an initial angle of emergence is determined for every ZO time sample. Similar to the automatic velocity scan, a discrete number of angles of emergence is tested. For each test parameter the traveltime is calculated from equation 1.10 and is correlated with the automatic CMP stack section. The angle of emergence that yields the highest coherency between the calculated and recorded data is stored as the initial value of α .

After the V_{NMO} and α are estimated, the R_{NIP} is defined through equation 1.8 as

$$R_{NIP} = \frac{V_{NMO}^2 t_0 \cos^2 \alpha}{2V_0}. \quad (1.11)$$

Now, the parameters α and R_{NIP} are found, and R_N can be estimated using equation 1.9 by testing the range of values and correlating the resulting traveltime curve with the CMP stack section.

Finally, the search algorithm provides the CRS parameters $P = (\alpha, R_N, R_{NIP})$ for every ZO time sample in the target zone. Each triplet defines a CRS stacking surface in the (m, h, t) domain (Figure 1.3). Summing up the prestack data along these surfaces and assigning the summation result to the respective ZO time sample yields the *initial* CRS stacked section.

Aperture considerations and optimisation

The validity of the approximation 1.4 for the description of reflection traveltimes generally decreases with increasing distance in the midpoint and offset directions from the considered zero-offset location, i.e. with increasing parameters m and h . The apertures in midpoint and offset directions used during the CRS stack must be chosen appropriately to obtain optimum CRS parameters and stacked sections. For large apertures, the hyperbolic traveltime approximation may no longer be valid, whereas a small aperture may decrease the quality of the CRS parameter estimation. The proper choice of the offset and midpoint apertures depends on the characteristics of the dataset under consideration, and is usually done after performing some numerical tests with the data. Furthermore, apertures for the CRS parameter search and for the actual stacking might be chosen independently. Larger apertures may improve the results of CRS parameter estimation, whereas using smaller apertures can help to avoid smearing effects by stacking.

The apertures in m and h directions are called *CRS apertures* in the following. The implementation of the CRS stack used in this work operates with time-dependent tapered apertures. Thus, the stacking operator is defined as an elliptical surface in the (m, h) domain (Mann, 2002) for a certain ZO traveltime (Figure 1.5).

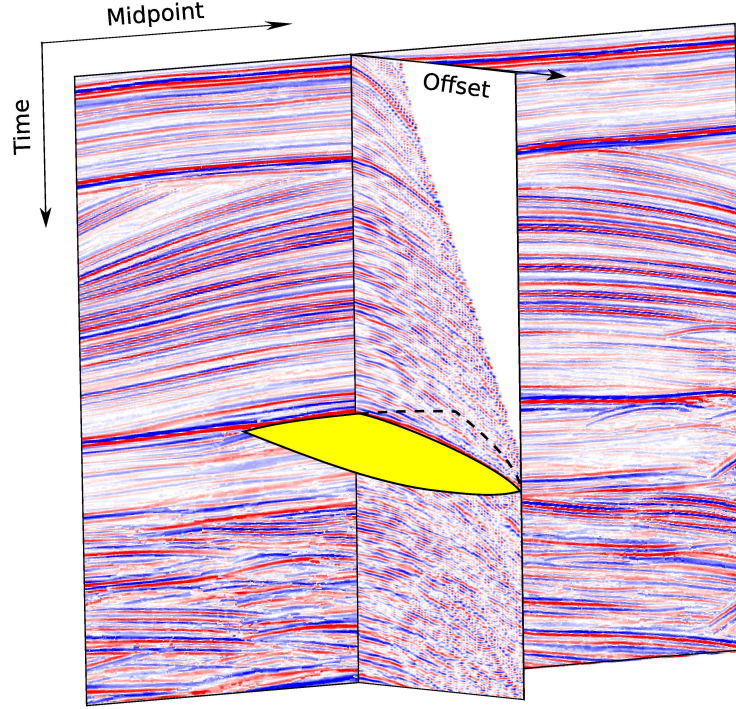


Figure 1.5: CRS stacking operator for seismic reflection data. The operator (yellow colour) is defined for every ZO point in a midpoint-offset domain as a surface of 2nd order that is limited by the time-dependent CRS apertures.

The so-defined initial values of CRS parameters can be further updated using the available optimisation algorithm based on a local simultaneous 3-parameter search (Mann, 2002). However, if the CRS apertures are chosen properly during the initial CRS stack, the results of the initial and optimised CRS stack are very similar. The optimisation is, however, a very time consuming process, and, therefore, was not used in this work. Therefore, the initial CRS parameters are used as *CRS parameters*, and the initial CRS stack as the *CRS stack* in the following.

1.4 NIP-wave tomography

The CRS stack process described in the previous section can be regarded as a tool for automatically extracting traveltimes information from the seismic data in the form of kinematic wavefield attributes. If the traveltimes of reflection events in the data are well described by the hyperbolic formula 1.4, the information contained in the CRS attributes can be used for the determination of a laterally inhomogeneous depth velocity model by an *inversion process*.

Ray segments of the specular rays connecting sources and receivers on the measurement surface with a common reflection point (CRP) in the model (Figure 1.6(a)) are geometrically identical to ray trajectories associated with a hypothetical emerging wave due to a point source at the NIP (Figure 1.6(b)). Therefore, the imaging of the associated reflection signals to a common reflection point in the model is equivalent to the focusing of the NIP-wave at zero traveltime at that point (Figure 1.6(c)). The NIP-wave tomographic inversion is based on the following criterion: in a correct depth velocity model all considered NIP waves, when propagated back into the earth along the normal ray, focus at zero traveltime (Duveneck, 2004).

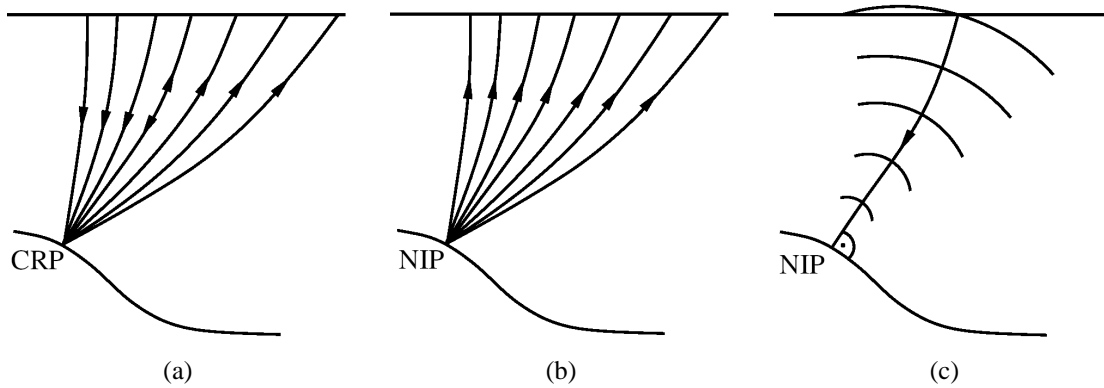


Figure 1.6: Ray trajectories associated with a CRP and NIP points. (a) Ray segments of specular rays reflect at a CRP in the subsurface. (b) Geometrically, ray trajectories associated with a hypothetical wave due to a point source at the NIP coincide with the CRP ray segments. (c) In a consistent velocity model, the NIP-wave focuses at the NIP at zero traveltime, when they are propagated back into the subsurface.

1.4.1 Data and model components

The NIP-wave tomography operates in the ZO domain approximated by the generated CRS stack section. In a CRS stack section each point (t_0, x) , where t_0 is TWT and x is distance, can be associated with a CRP in the subsurface. The second-order kinematic multioffset response of

the CRP is defined through the corresponding CRS attributes R_{NIP} and α . Instead of R_{NIP} , the quantity

$$M_{NIP} = \frac{\cos^2 \alpha}{V_0 R_{NIP}} \quad (1.12)$$

is used (Duvenceck, 2004), where V_0 is the near-surface velocity. The quantity M_{NIP} can be associated with the second spatial derivative of the NIP wave traveltime of a ZO ray in the direction normal to the ray at x ($\partial^2 t / \partial x^2$), and α is the estimated emergence angle. Identification of M_{NIP} with the NIP-wave's second spatial derivative is possible using the NIP-wave theorem, given by Hubral and Krey (1980). It states that to second order in the offset coordinate the CMP reflection traveltime coincides with the traveltime of hypothetical rays passed from the source to the receiver through the NIP of the ZO ray on the reflector. Therefore, the traveltime of a reflection event in a CMP gather can be calculated as a sum of the traveltimes along the two rays connecting the NIP with the source and with the receiver. M_{NIP} can be calculated along a ray by dynamic ray tracing. If the ray is started at the NIP, it is given by

$$M_{NIP} = \cos^2 \alpha \frac{P_2}{Q_2}, \quad (1.13)$$

where P_2 and Q_2 are elements of the ray propagator matrix in ray-centered coordinates (e.g., Červeny, 2001; Duvenceck, 2004). The formula approximates the CRP response in the vicinity of a normal ray at any location along the ray.

The input for the inversion consists of a number of points picked in the ZO section (e.g., the CRS stack section), defined by their values of t_0 and x together with the associated values of α and M_{NIP} , calculated from the corresponding CRS parameters. The input data are given by

$$\mathbf{d} = \left(\frac{t_0}{2}, M_{NIP}, \alpha, x \right)_{i=1}^n, \quad (1.14)$$

where n is a number of picked data points.

Using the focusing properties of NIP-waves, a direct way for velocity model estimation would be to propagate the NIP-wave back into the subsurface and check if they focus at $t_0 = 0$. Focusing means that the radii of curvature of the NIP-wave R_{NIP} becomes zero. However, all picked data must be expected to have noise or measurement errors. An inversion that does not allow these errors is unstable. This is taken into account using the dynamic ray tracing started in the subsurface at the respective CRPs. Since their true subsurface positions and local dips are initially unknown, they must be estimated together with the unknown velocity distribution. The optimum model is found when the misfit between modelled and measured values of \mathbf{d} is minimised.

The NIP-wave tomography exploits the concept of a smooth velocity model defined by discrete B-spline coefficients (Duvenceck, 2004). The use of such defined models in velocity estimation methods leads to some advantages, as it allows the formulation of inversion algorithms which do not assume continuous reflectors in the model. Pick locations in the stacked zero-offset section

can be independent of each other, which simplifies the picking process: the picks required for this approach do not have to follow continuous reflection events in the data, but may be located on events that are only locally coherent. In particular, the determination of velocity models becomes possible also in the areas of complex salt plugs, where it is difficult to follow reflection events continuously along the seismic section.

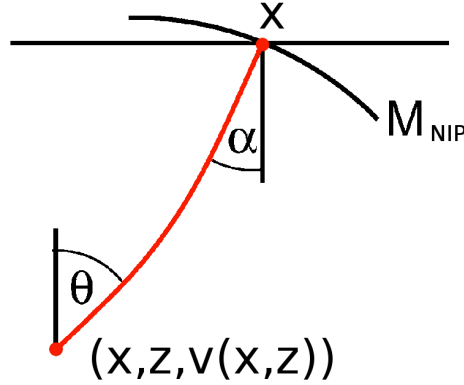


Figure 1.7: Data and model components for the NIP-wave tomographic inversion.

The 2D NIP-wave tomography defines each CRP by its location in the subsurface (x, z) and its local dip angle θ , which also gives the direction of the normal ray (see Figure 1.7). The smooth velocity model itself is described on a grid with n_x and n_z nodes in the horizontal and vertical directions accordingly by

$$v(x, z) = \sum_{i=1}^{n_x} \sum_{j=1}^{n_z} (v_{ij} \beta_i(x) \beta_j(-z)), \quad (1.15)$$

where β_i and β_j are the B-spline basis functions, and the coefficients v_{ij} are the velocity model parameters to be determined during the inversion procedure.

1.4.2 Inverse problem

The problem of estimating the correct velocity model consists of finding a vector of model components \mathbf{m} defined as

$$\mathbf{m} = [(x, z, \theta)_{i=1}^n, v_{ij}], \quad (1.16)$$

that minimises the misfit between the picked data \mathbf{d} (defined in expression 1.14) and the modelled values

$$\mathbf{d}_{mod} = f(\mathbf{m}). \quad (1.17)$$

Here, the nonlinear operator f symbolises the dynamic ray tracing in the given model. The implementation of [Duveneck \(2004\)](#) uses the least-squares norm as a measure of misfit. Thus, the inverse problem becomes one of minimising a cost function:

$$S(\mathbf{m}) = \frac{1}{2} \|\mathbf{d} - f(\mathbf{m})\|_D^2. \quad (1.18)$$

This inverse problem is, however, ill-posed, because not all model components are sufficiently constrained by the data alone, i.e., the number of parameters describing the data might be less than the number of parameters describing the model. To regularise this problem, the NIP-wave tomographic inversion needs additional constrains. These constrains describe the smoothness of the model, since the smooth model is the simplest one that explains the data. This criterion also ensures the applicability of the dynamic ray tracing used for the forward modelling. To apply the mentioned constrains, a term depending on the B-spline coefficients is added to the cost function:

$$S(\mathbf{m})_{reg} = S(\mathbf{m}) + c(vij) = \frac{1}{2} \|\mathbf{d} - f(\mathbf{m})\|_D^2 + c(vij), \quad (1.19)$$

where $c(vij)$ is a measure for the model smoothness.

Because of the nonlinearity of f , a global nonlinear optimisation method is required. For computational reasons, however, NIP-wave tomography uses an iterative search of velocities. The modelling operator f can be locally linearised. Therefore, a minimum of the cost function S is found by iteratively applying least-squares minimisation to the linearised problem ([Duveneck, 2004](#)). Starting with a first-guess model \mathbf{m}_0 , tomographic inversion generates a sequence of model updates which, when properly performed, converges to the global minimum of S .

1.4.3 Inversion algorithm

First, the inversion algorithm sets up an initial velocity model by defining B-spline nodes in the horizontal and vertical directions and assigning initial values to the velocity coefficients. As an initial model a constant gradient model is usually used, described as

$$V(z) = V_0 + gz, \quad (1.20)$$

where V_0 is the surface velocity, g is the velocity gradient, and z is the depth. Alternatively, a priori velocity information can constrain the initial velocity model.

For each of the picked data points with the corresponding attributes of vector \mathbf{d} (expression 1.14), kinematic ray tracing in the downward direction of the starting velocity model yields initial elements of vector \mathbf{m} (expression 1.16). Using these values, dynamic ray tracing in the upward

direction is performed until the rays reach the measurement surface to obtain the elements of model vector \mathbf{d}_{mod} (1.17). Then, the cost function is calculated using equation 1.19, which characterise the misfit between picked and modelled data. The linear system of equation using the least-square method is solved, and the model update vector is obtained. Then the current model is updated, and the forward dynamic ray tracing is repeated using the new model. If the cost function increases, the model update vector decreases, and the cost function is recalculated; otherwise, the next iteration is started. The process of iterative model updates and forward dynamic ray tracing is stopped, when the data misfit reaches the specified minimum, or when the given maximum number of iterations is reached, or when the minimum of the cost function is found, i.e., the further decreasing of the model update vector does not lead to the decrease of the cost function. The characteristic decrease of the model update vector during the inversion has the effect of the determination of the long-wavelength features during the first iterations, while more and more details can be resolved in further iterations. This effect is shown in the examples with real data in Chapters 2 and 3.

1.4.4 Picking and editing of input data

Picking of zero-offset points, required for the determination of the input data vector \mathbf{d} (expression 1.14) is performed after the estimation of the CRS parameters and generation of the CRS stack section. For this purpose the automatic CRS stack section and corresponding coherence section that is a by-product of the CRS stack can be used. The picking can be carried out either manually or in the automatic mode. The pick locations do not need to follow the interpreted horizons, but they have to be located on primary reflection events. If in a given seismic dataset multiples are attenuated, the automatic picking algorithm provides reliable results. The picking program uses the CRS coherence section with additional constrains like a coherence threshold, a minimum separation in space and time of pick locations and others. For complex geologies like in areas with salt plugs, manual picking of events on the salt flanks is sometimes more reasonable than automatic picking. Examples of manual and automatic picking of input data for the NIP-wave tomography are shown in Chapters 2 and 3.

After the picking has been performed and the coordinates $(t_0, x)_i$ associated with each point are defined, the data attributes M_{NIP} and α are automatically extracted from the corresponding CRS parameter sections and assigned to the picked points. Thus, the initial components of the data vector \mathbf{d} are completely defined, and the inversion could be started. However, prior to the inversion process, the input data must be checked for the presence of outliers, multiples and other noise, and, when necessary, edited. Such contaminated data can be identified by plotting the data components M_{NIP} and V_{NMO} as a function of traveltimes.

If subsurface structures are relatively simple, the data points most likely related to multiples can be identified in a way similar to the conventional velocity analysis. Substituting the R_{NIP} from

equation 1.11 in the data component M_{NIP} defined by equation 1.12 yields

$$M_{NIP} = \frac{\cos^2 \alpha}{V_0 R_{NIP}} = \frac{2}{t_0 V_{NMO}^2}. \quad (1.21)$$

Since R_{NIP} associated with the reflector depth monotonously increases with the traveltimes, the value of M_{NIP} should decrease with increasing t_0 . Thus, the characteristic decrease of V_{NMO} , as normally observed for multiple reflections, can result into a corresponding increase of M_{NIP} at the considered traveltimes. In the plots of M_{NIP} for all picked data points against t_0 , the picks deviating significantly from the main trend can be associated with multiples and should be eliminated from the inversion (see examples in Figure 1.8(a)). The multiples can also be identified using the plot of V_{NMO} , computed from input data by equation 1.8, as a function of t_0 . The process is similar to the conventional stacking velocity analysis: the data with too low velocities at considered traveltimes are associated with multiples and should be removed (Figure 1.8(b)).

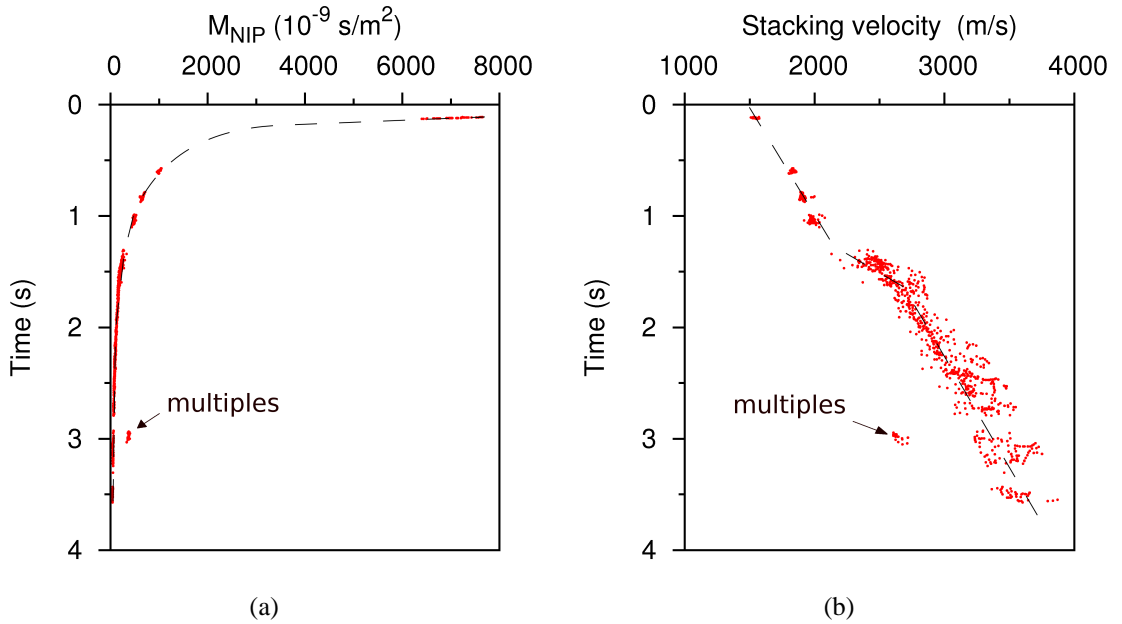


Figure 1.8: Quality control of input points for the NIP-wave tomography. (a) The data component M_{NIP} and (b) stacking velocities are computed for each picked ZO point from the corresponding CRS parameters. The picks deviating significantly from the main trend (dashed lines), most likely correspond to multiples (or other noise), and should be removed.

1.5 Depth migration

1.5.1 Migration basics

Seismic data is generated by elastic waves propagating through the subsurface. The time image obtained by the reflection seismic method is in general a distorted image that does not correctly reflect the true geometry of the subsurface structure. While a horizontal reflector in depth will appear as a horizontal reflector on the time section, a dipping reflector is incorrectly positioned on the time stacked section. This effect is demonstrated for a constant velocity medium in Figure 1.9. The true position of the reflector in depth differs from its position on the time section. The lateral and vertical positions are different, as well as the dip of the reflector. The wave propagation process is characterised by the rays normal to the reflector that propagate from the surface to the reflector and back. On a ZO time section the events associated with the normal rays are plotted vertically at the position where the ray emerges at the surface (receiver location). As a result, the apparent time dip of the reflection is smaller than the true dip, and the reflector itself appears longer.

The task of migration is to take into account the effects of the wave propagation through the medium and to correct the reflector position in the recorded data. As a result, migration steepens dips, shortens dipping events, and moves events updip. In addition to the geometrical distortions, the wave propagation process creates diffractions from sharp edges as well as amplitude changes due to the geometrical spreading. Migration with consistent velocity models collapses diffractions, focuses energy, and positions the diffraction events at their correct locations. The effect of depth migration with a consistent velocity model can be summarised, but not limited, to the following points:

- migration moves dipping reflectors updip to their true position;
- migration removes effects of reflector curvature such as increased anticlines, decreased synclines and "bow-tie" structures (Stolt, 2002);
- migration focuses diffractions from faults, bed truncations, and other discontinuities;
- depth migration removes distortions due to lateral velocity variations. If the lateral changes of medium velocity are rapid enough, the diffraction pattern can depart significantly from the hyperbolic shape. Conventional stacking or time migration algorithms using the hyperbolic approximation can lead to errors both in velocity estimations and imaging.

Furthermore, prestack depth migration can be used as a tool for velocity model estimation and for the quality control of the migration velocities using the CIGs.

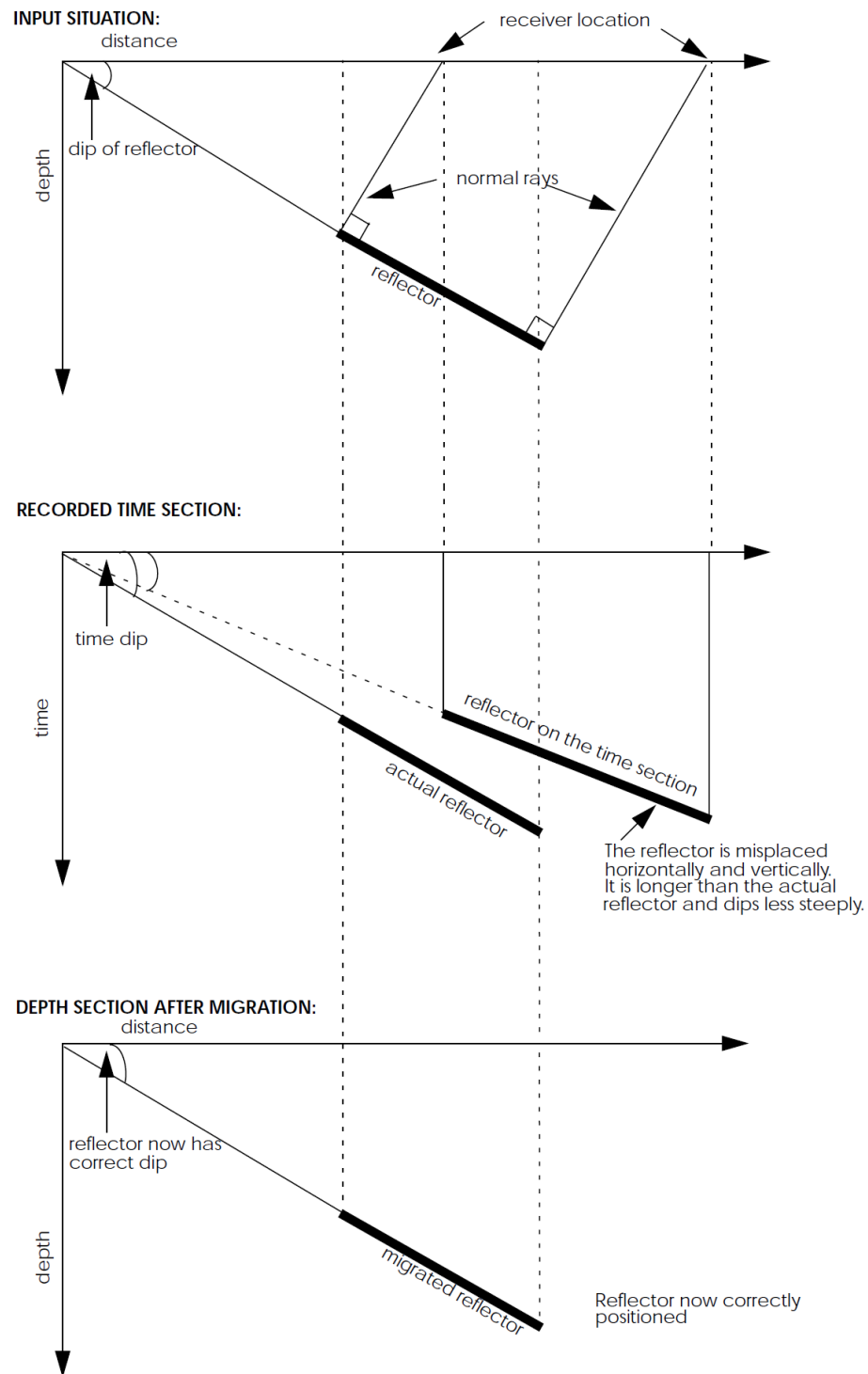


Figure 1.9: Geometrical principle of migration for a constant velocity medium with a dipping reflector. The true position of the reflector in depth differs from its position on the time section. Depth migration corrects this effect and moves the reflector to its original position in space.

1.5.2 Depth migration as diffraction summation

Poststack migration by the *diffraction summation* can be described using the *exploding reflectors concept*. Consider closely-spaced exploding sources that are located along the reflecting interfaces (Loewenthal et al., 1976). Also, consider one receiver located on the surface at each CMP position. The sources explode in unison and send out waves that propagate upward. The earth model described by this experiment is referred to as the *exploding reflectors model*. With this model, the seismic section is represented by the wavefield that is recorded on the surface. In other words, the seismic section is described by function

$$f(x, z = 0, t), \quad (1.22)$$

where x is the lateral position (CMP coordinate), t is one-way traveltime, and z is depth. The objective of migration is to reconstruct the situation that existed at the time $t = 0$ when the wave propagation process from the exploding reflectors began. Therefore, the initial situation is expressed by the function

$$f(x, z, t = 0), \quad (1.23)$$

and the migration process is defined by the transformation

$$f(x, z = 0, t) \xrightarrow{\text{migration}} f(x, z, t = 0), \quad (1.24)$$

which is performed using wavefield extrapolation techniques, e.g., diffraction summation. Using this principle, migration can be considered as a mapping of the data from the recorded time domain to the initial time ($t = 0$). The mapping is obtained by deriving the wavefield $u(x, z, t)$ from the recorded data $u(x, z = 0, t)$, which is called *extrapolation*, and further restricting to $u(x, z, t = 0)$, referred to as *imaging*.

Migration by a diffraction summation method uses the exploding reflector model and calculates the diffraction traveltime corresponding to the closely spaced diffractor points on a reflector. Each point on a migrated section is treated independently from other points. Imaging is performed by summing the amplitudes along a diffraction curve in a unmigrated section and assigning the result to the diffractor point in a migrated section (Figure 1.10). The resulting migrated section is a superposition of all contributions from diffraction points. The image is built as the envelope of all curves by constructive interference. The edges of the curves are cancelled due to destructive interference (see Figure 1.10).

1.5.3 Kirchhoff depth migration

The diffraction summation that incorporates the obliquity factor, which describes the angle dependence of amplitudes, and the spherical spreading factor, is called the Kirchhoff summation,

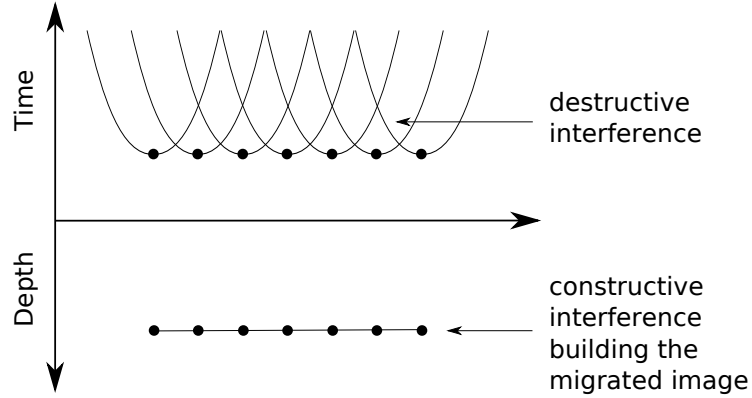


Figure 1.10: Diffraction summation method for a horizontal reflector. The depth image is obtained by constructive summation of time responses for closely spaced diffraction points.

and the migration method based on this summation is called the Kirchhoff migration. In this work I describe the main concepts of the Kirchhoff depth migration without going too deep into the technical details. The detailed description of the method can be found in numerous publications, e.g., by [Schneider \(1978\)](#); [Schleicher et al. \(1993\)](#); [Stolt and Benson \(2001\)](#); [Yilmaz \(2001\)](#).

Typically, for performing the depth migration, one wants to find the solution of the acoustic wave equation in 3D described by

$$\frac{\partial^2 u}{\partial x^2} + \frac{\partial^2 u}{\partial y^2} + \frac{\partial^2 u}{\partial z^2} = \frac{1}{V^2} \frac{\partial^2 u}{\partial t^2}, \quad (1.25)$$

where $u(x, y, z, t)$ is the pressure wavefield as a function of the three orthogonal Cartesian coordinates (x and y are two profile coordinates, z is depth) and t as time. The inhomogeneous subsurface model is represented by the propagation velocity of seismic waves as a function of coordinates, $V = V(x, y, z)$. As mentioned above, the seismic reflection datasets used in this work were recorded using a 2D acquisition. Therefore, I consider only the 2D case in the following.

For 2D we assume no change of velocity along one profile coordinate (e.g., y), and the term $\partial^2 u / \partial y^2$ in equation 1.25 is zero. First, the constant velocity case is considered. The problem formulation reduces to finding the solution of the scalar wave equation with the constant velocity V_c :

$$\frac{\partial^2 u}{\partial x^2} + \frac{\partial^2 u}{\partial z^2} = \frac{1}{V_c^2} \frac{\partial^2 u}{\partial t^2}. \quad (1.26)$$

This equation can be rewritten using the Laplacian operator ∇ as

$$\nabla^2 u = \frac{1}{V_c^2} \frac{\partial^2 u}{\partial t^2}, \quad (1.27)$$

where

$$\nabla^2 u = \left(\frac{\partial^2 u}{\partial x^2} + \frac{\partial^2 u}{\partial z^2} \right) \quad (1.28)$$

In these terms, the wavefield observed at the surface ($z = 0$) is described by the function

$$u(x, z = 0, t), \quad (1.29)$$

which is the boundary value of the wavefield

$$u(x, z, t), \quad (1.30)$$

propagating from a reflector in the subsurface upwards for $t > 0$.

The problem of *extrapolation* consists of determining the wavefield $u(x, z, t)$ for $z > 0$. Using the wave equation 1.27, $u(x, z, t)$ is computed from $u(x, z = 0, t)$ that is measured at the surface. This procedure is known as "*downward continuation*". *Imaging* is achieved by restricting the wavefield to the case $u(x, z, t = 0)$. In the following the most commonly used solution of the wave equation using the "*Kirchhoff formula*" is introduced.

Suppose that we wish to solve a boundary value problem for the scalar wave equation on the interior of a closed surface F in two dimensions, with boundary conditions specified on a smooth boundary ∂F . Now, using the Huygens' principle that every point on a wavefront can be considered a secondary source of a cylindrical wave, we are synthesising a general solution of the wave equation from the cumulative effects of an infinite number of point sources. This can be made mathematically by computing an impulse response function, or *Green's function* $G(\mathbf{r}, \mathbf{r}')$, which is the solution of the inhomogeneous Helmholtz equation

$$\nabla^2 G + k^2 G = -4\pi\delta(\mathbf{r} - \mathbf{r}'), \quad (1.31)$$

where vector $\mathbf{r} = (x, z)$ defines the diffractor point, \mathbf{r}' defines the receiver, and $\delta(\mathbf{r} - \mathbf{r}')$ is Dirac's delta function. The Green's function, therefore, depends on both source and receiver coordinates.

Using the Fourier transformation with respect to travelttime

$$u(x, z, t) = \frac{1}{2\pi} \int_{-\infty}^{\infty} U(x, z, w) e^{iwt} dw \quad (1.32)$$

and

$$U(x, z, w) = \int_{-\infty}^{\infty} u(x, z, t) e^{-iwt} dt, \quad (1.33)$$

where w is frequency, the second-order time derivative of the wavefield transforms as

$$\frac{\partial^2 U}{\partial t^2} \xrightarrow{\text{FT}} -w^2 U. \quad (1.34)$$

Substitution of the function $U(x, z, w)$ into the wave equation 1.27 yields the Helmholtz equation

$$\nabla^2 U + \left(\frac{w}{V_c}\right)^2 U = \nabla^2 U + k^2 U = 0, \quad (1.35)$$

with k being the wavenumber.

Using the solution for the inhomogeneous Helmholtz equation 1.31 in the frequency domain in form of Green's function, the solution of the wave equation 1.27 is obtained by the *Kirchhoff formula* in 2D:

$$U(\mathbf{r}, w) = -\frac{1}{4\pi} \oint_{\partial F} \left[U(\mathbf{r}', w) \frac{\partial G(\mathbf{r}, \mathbf{r}', w)}{\partial n'} - G(\mathbf{r}, \mathbf{r}', w) \frac{\partial U(\mathbf{r}', w)}{\partial n'} \right] ds'. \quad (1.36)$$

Here, ds' and dn' define the size and normal of the linear element of the boundary S that limits the surface F , containing the point (x, z) . To apply the equation 1.36 for migration, some transformations are made, which finally yield the solution of the scalar wave equation in form of

$$u(x, z, t) = \int_{-\infty}^{\infty} \frac{\partial u(\xi, 0, t)}{\partial t} * W(x, z, \xi, t) d\xi, \quad (1.37)$$

where W is a *weight-function* and $*$ indicates convolution.

Migration uses this solution with specified imaging conditions. The final 2D Kirchhoff migration formula describes the depth migrated section

$$M(x, z) = \frac{1}{\sqrt{2\pi}} \int_{-\infty}^{\infty} u_F(\xi, 0, t_I + \frac{r}{V_c}) \frac{\cos \phi}{\sqrt{V_c r}} d\xi \quad (1.38)$$

with the following parameters:

- the time $t_I + \frac{r}{V_c}$ describes the traveltime curve of the diffraction point located in (x, z) ;
- the factor $\sqrt{V_c r}$ describes the geometrical spreading of a cylinder wave propagating from the point $(\xi, 0)$ to (x, z) ;

- the angle ϕ is the emergence angle of the ray at the receiver;
- the function u_F describes the high-pass filter of the time section, which is also denoted as the *half-derivative* of the input wavefield $u(x, z = 0, t)$ in the time domain (e.g., [Bleistein et al., 2000](#)).

The classical Kirchhoff algorithm uses the solution with Green's functions for a constant velocity medium. By giving up the requirement that the Green's function be computed analytically, the Kirchhoff solution is extended to variable velocity media. The modified Kirchhoff method uses traveltimes of waves travelling from each point in the subsurface to each source/receiver location, instead of the hyperbolic traveltimes description of diffraction events in a homogeneous medium.

A direct method for calculating time response for diffractor points is *ray tracing* through a specified depth velocity model. Traveltime computations can also be performed using different techniques, e.g., a finite difference (FD) approximation to the Eikonal equation ([Reshef and Kosloff, 1986](#)), Gaussian beam ray tracing ([Červený, 2001](#)), direct wavefront construction methods (e.g., [Vinje et al., 1993](#); [Ettrich and Gajewski, 1998](#); [Coman and Gajewski, 2001](#)), dynamic ray tracing ([Červený, 2001](#)) and others.

Ray tracing is a commonly used approach since it is less expensive in time and easier to apply. A bundle of rays emerging from a source location can be traced down into the earth to the subsurface taking the velocity variations and refractions at layers boundaries into account. The traveltimes from the source point to the reflector point and from the reflector point to the receiver are then calculated along both raypaths, and summed to produce the traveltime from the source to the receiver. Dynamic ray tracing additionally provides the computation of the amplitudes, taking the geometrical spreading into account. Green's function obtained by the dynamic ray tracing form the basis for an amplitude-preserving depth migration (e.g., [Schleicher et al., 1993](#)). Alternative traveltime-based approach without the dynamic ray tracing was introduced by [Vanelle et al. \(2006\)](#).

1.5.4 Practical aspects

Poststack depth migration

So far I have discussed the principles of depth migration only in the context of mapping seismic sections from the time to depth domain. In practice, this means that the seismic reflection data is first corrected for the normal moveout, then stacked, and finally migrated. This method, known as depth migration after stack or *poststack migration*, *PostSDM*, produces the correct image of

reflectors only for simple media without strong lateral velocity variations. Poststack migration assumes that the stacked data correctly represents the ZO section, i.e., where the source and receivers coincide. The CRS stacked sections are better approximations of the ZO sections than the conventional NMO/DMO stacks, as shown by Müller (1999). Therefore, in this work I use the simulated ZO CRS stacked sections as input for poststack depth migration.

Nevertheless, any method of time stacking applied to seismic reflection data does not take strong lateral velocity variations into account due to the hyperbolic traveltimes assumption (equations 1.1 and 1.4). When the subsurface structure is complex, reflection moveout becomes non-hyperbolic and can not be correctly described by the hyperbolic traveltime formulas. The stacking process does not work well, producing distorted stacked image as output. These situations can be solved by migration before stack, which is known as *prestack migration*, *PreSDM*. It migrates the unstacked seismograms directly into the depth domain and then performs stacking in order to generate the depth image.

Prestack depth migration

Prestack Kirchhoff depth migration operates on every offset of the data separately. For each common-offset section the Kirchhoff summation procedure is applied. Migration focuses diffractions and moves reflectors to their true positions in every common-offset section. In other words, prestack depth migration with a consistent velocity model results in a number of sections, having different offsets, where the reflector depth is identical.

Results of migration in the common-offset domain allow the quality control of the depth velocity model. First, the focusing of diffraction events can be used to confirm the correctness of the model. If the diffraction curves are collapsed, the velocity model fits the data. Remaining diffractions usually observed at salt-sediments boundaries, faults, and other discontinuities, indicate that the depth velocity model is not consistent with the data. More powerful is the quality control scheme based on the depth migrated CIGs. CIGs result from sorting the depth migrated data into gathers having common reflection points. Each CIG corresponds to one CMP location in the data. Since the events in the prestack data are moved towards their true lateral position after migration, each CIG contains traces describing one reflection point at the considered depth. When the velocity model is correct, each offset plane is correctly migrated, and the reflector in every common-offset section appears at the same position. Therefore, the CIGs become horizontal (Figure 1.11). However, if the velocity model does not fit the data, an over- or undercorrection is observed in the CIGs (Figure 1.12). This phenomenon can be explained as follows: when the velocity is too low, the computed traveltime along the ray is too high, and the imaging condition is fulfilled for points at shallower depth. The effect increases with growing offset. Therefore, the CIG is overcorrected, and the reflector is shifted upwards (Figure 1.12(a)). If the migration velocity is too high, the result is an undercorrected gather, where the reflector is shifted downwards

(Figure 1.12(b)).

Prestack depth migration, therefore, is very sensitive to the accuracy of the velocity model used during the depth migration. This fact can be used for the migration velocity analysis using the CIGs if the CIGs are not horizontal. The residuals are picked, and the velocity model is updated. Usually this process is performed iteratively, every time picking the residuals, updating the velocity model, and migrating the data using the updated model until the residuals are below a defined threshold. Once the CIGs are horizontal, they can be stacked along the offsets to generate a depth migrated section, where the reflectors are at their true positions.

In this work the seismic reflection data were migrated with Kirchhoff prestack depth migration using maximum amplitude ray tracing since it allows to generate the most accurate depth images of the subsurface in complex areas. The resulting CIGs are used for quality control of the migration velocity model obtained by NIP-wave tomography (see Section 1.4).

Migration aperture

The migration formula 1.38 uses the infinite integral solution of the wave equation. In practice, the seismic profile length is finite, and the integral is limited by the migration aperture. The aperture width is defined in the common-offset domain as the length of the summation operator. The choice of the aperture is very important for depth imaging of real seismic data. Whereas small apertures can produce a poor image due to the destruction of steeply dipping events and can organise random noise signals as horizontal events, the large apertures unnecessarily increase the run time and produce artifacts and migration noise. Yilmaz (2001) described numerous examples of different aperture effects by migration. The value of apertures must be chosen according to many factors including, but not limited to, the acquisition geometry, the complexity of the subsurface and the chosen migration algorithm. From the geometrical aspect of migration follows that larger apertures are better suited for steeply dipping events, and shorter apertures should be used for smaller inclination angles. The aperture must be large enough to include all rays travelling downwards from a source to a reflector and upwards from the reflector to a receiver. The lateral position of the reflection points for dipping reflectors deviates from the midpoint position, and this difference increases with larger reflector dips. Therefore, large apertures width must be used for steeply inclined reflectors.

The optimum migration aperture can be estimated from data (Schleicher et al., 1997). The criterion for the minimum migration aperture is that the difference of traveltimes of the computed diffraction curve and the reflection curve should be less than half a period $T/2$ of the signal, thus providing the constructive summation. This criterion also defines the first Fresnel zone. The difference between two approaches is that the minimum migration aperture is defined at the surface, whereas the first Fresnel zone is defined on the reflector. In practice, the proper choice

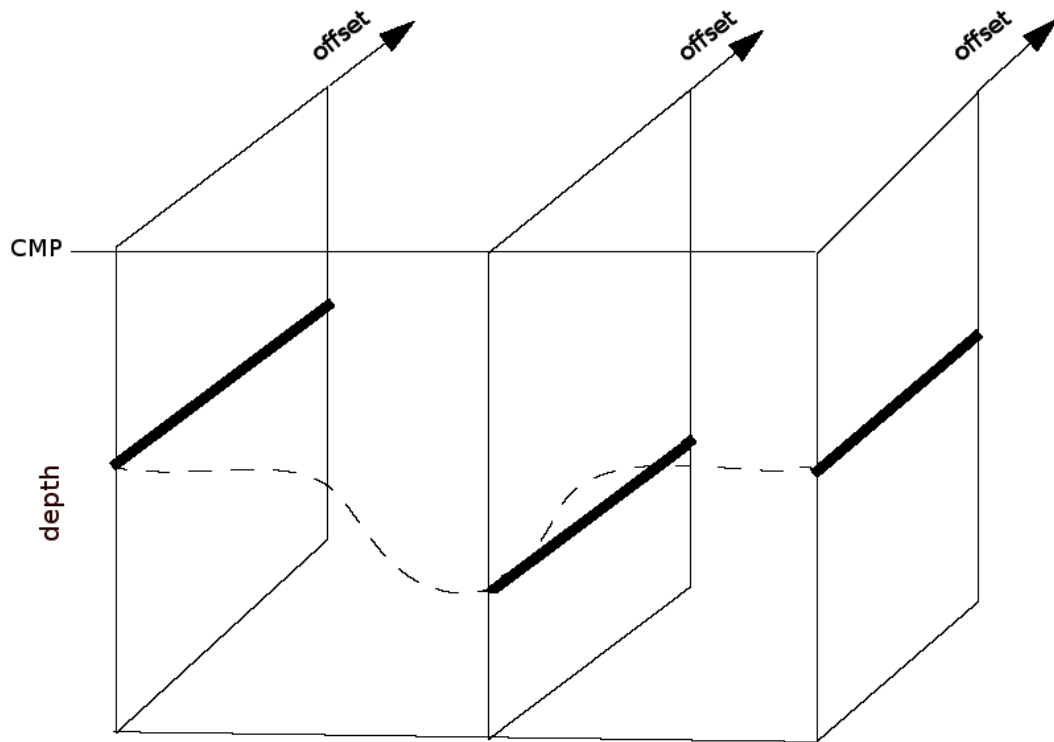


Figure 1.11: Flat common image gathers after prestack depth migration.

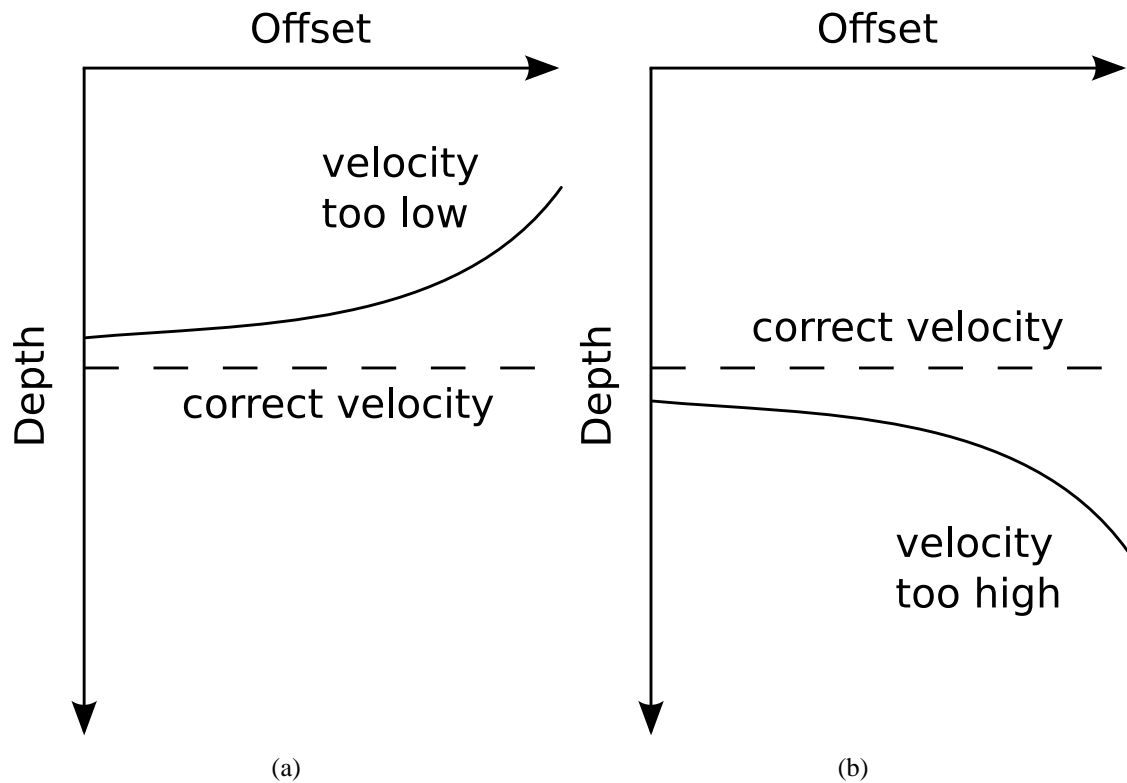


Figure 1.12: Common image gathers as a result of prestack depth migration. (a) When the migration velocity is lower than the true velocity, the CIG is over-corrected, and the reflector is shifted upwards from its original position. (b) When the velocity is higher than the true velocity, the CIG is under-corrected and the reflector is shifted downwards.

of migration aperture is usually achieved after a series of migration experiments with different values, finally choosing the one that produces the best depth image of the data.

Chapter 2

Marine data example

In order to investigate the behaviour of the CRS stack method on seismic data with complex geology, I apply it to a marine dataset from the North Sea. The dataset was kindly provided by BP with the assistance of RWE Dea AG (Hamburg). The main targets of the CRS processing of these data is the improvement of the quality of time-stacked sections in the areas of salt plugs and the reconstruction of a depth velocity model followed by depth migration.

2.1 Study area and acquisition geometry

The study area is located in the North Sea close to the German coast line (see Figure 2.1). Salt structures and complex fault systems characterise the region. The area is a part of the intracratonic Southern Permian Basin formed at the end of the Variscan orogeny (Ziegler, 1990). The orogeny occurred in Paleozoic times (from ~ 390 to ~ 310 mya). It reflects the continental collision between Laurasia and Gondwana to form the supercontinent of Pangea (see, e.g., Mohr et al., 2005).

The sedimentation process started in the Upper Rotliegend (see Figure 2.2) and continued to the evaporites of the Zechstein Group, which reached up to 800 m. Different phases of salt movements that started in Triassic time formed the salt structures of the region. Each phase is characterised by changing tectonic regimes and different kinds of diapirism (see Mohr et al., 2005).

A part of the data consisting of 4243 CMP gathers with a total line length of ~ 26.5 km was

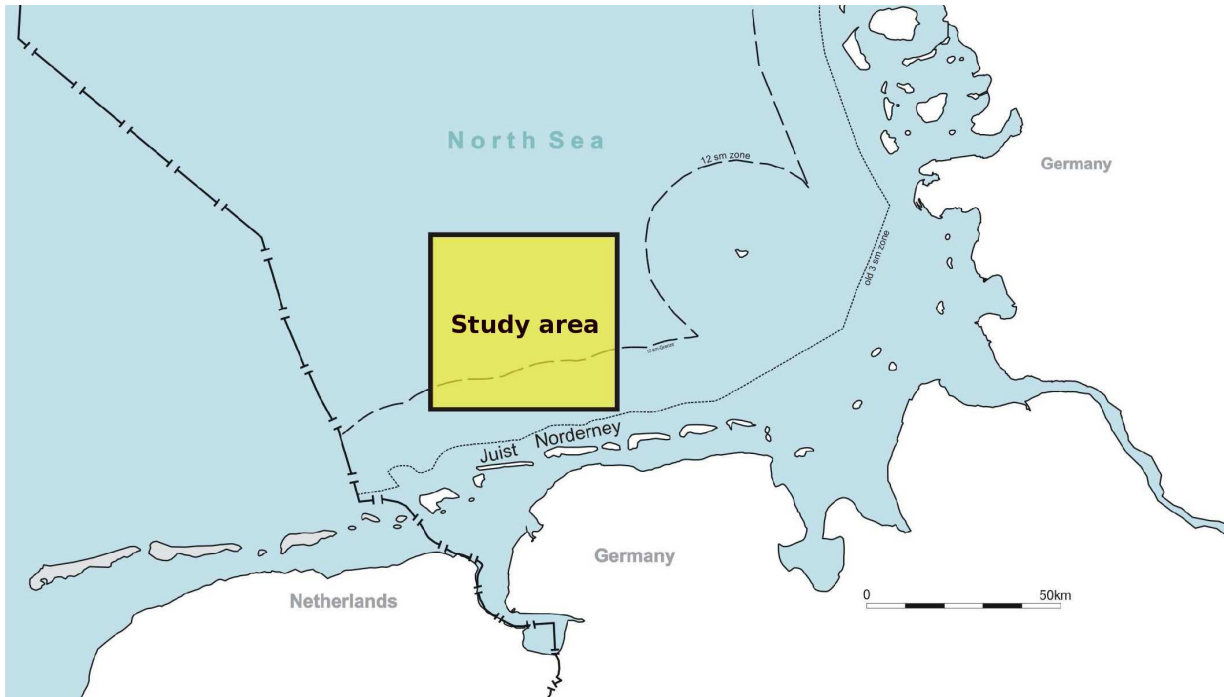


Figure 2.1: Marine data. The study area is located in the southern part of the North Sea approximately 30 km north of the German coast line (Kindly provided by RWE Dea AG, Hamburg).

Line length	~26.5 km	Acquisition type	end-on
Recording time	7 s	Receivers per shot	240
Time sample rate	2 ms	Receiver group spacing	12.5 m
Number of shots	1055	Source-receiver offset range	[-3238 m; -250 m]
Source spacing	25 m	Number of CMPs	4243
Source type	Airgun	CMP spacing	6.25 m
Source depth	6 m	Maximum CMP fold	60

Table 2.1: Marine data: acquisition parameters.

chosen for the CRS processing. Seismic reflection data were acquired in a 2D marine survey carried out in 1988 on behalf of ARCO (later acquired by BP). The acquisition parameters are summarised in Table 2.1. An airgun generated the seismic signal at 6 m depth. The shotpoint spacing was 25 m. A 240-channel streamer with 3000 m active length and 250 m lead-in with hydrophones towed at 7.5 m water depth was used. The receiver group spacing was 12.5 m. The acquisition geometry leads to 6.25 m of CMP spacing and a maximum CMP fold of 60. The record length was 7 s with 2 ms sample rate. No well information was available, but the stacking velocities were provided with the dataset.

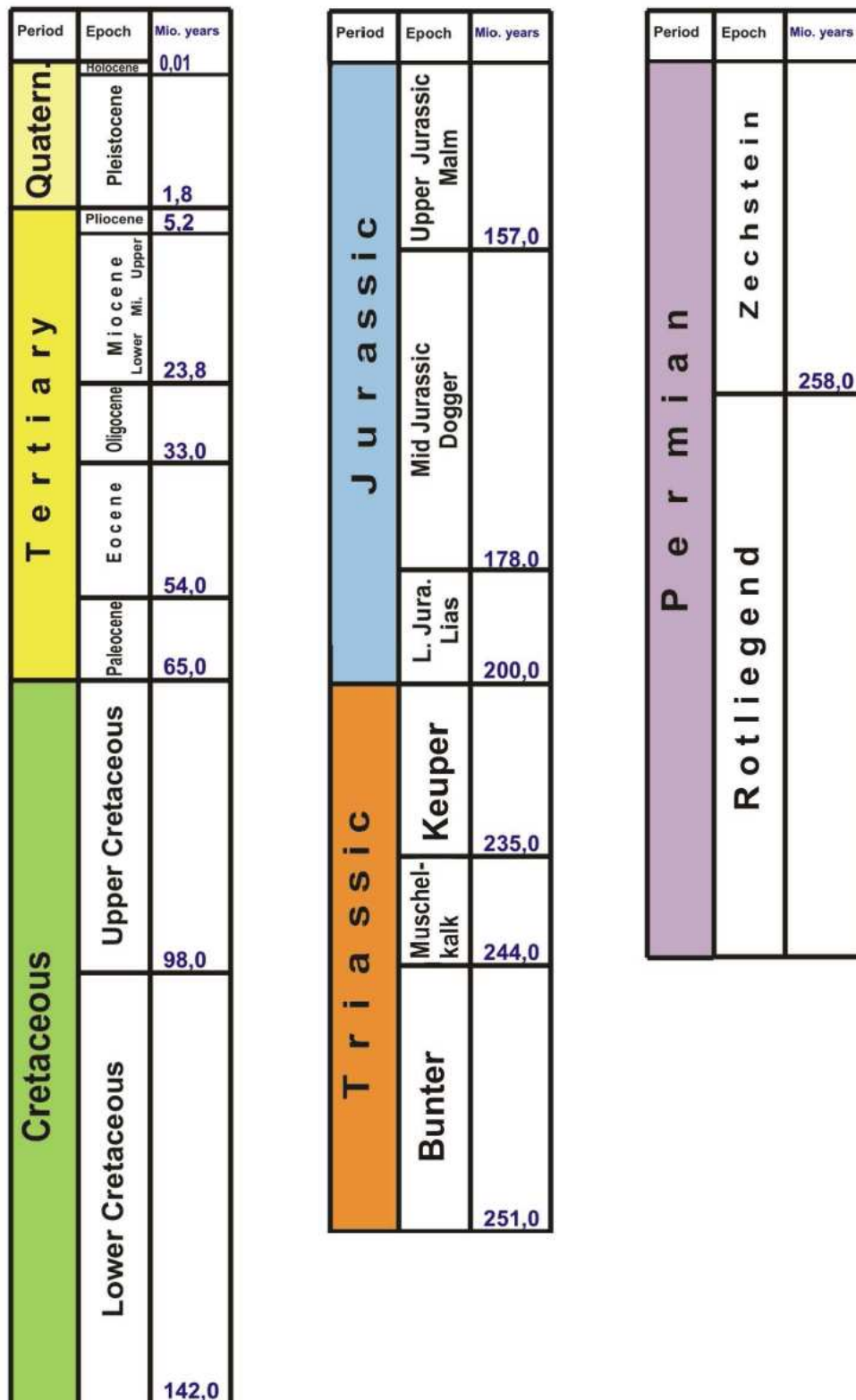


Figure 2.2: Marine data: generalised stratigraphic chart of study area (kindly provided by RWE Dea AG, Hamburg).

2.2 Preprocessing

The seismograms were preprocessed by Petrologic Geophysical Service GmbH (Hannover) in 2002. All preprocessing steps were performed using ProMAX software of Halliburton (Houston). The main targets were the Rotliegend sandstones, placed below the salt domes. The preprocessing consisted of the following steps:

1. Spherical divergence correction. The amplitude loss was recovered using a spherical divergence correction described by $1/(tV^2)$, where t is TWT, and $V(t)$ – root-mean-squared (RMS) velocity of the primary reflections.
2. Editing. Spikes and noise-bursts were estimated statistically, and, when necessary, edited.
3. $\tau - p$ transformation for the reduction of noise. Improvement of S/N ratio was achieved by the transformation of the data into the $\tau - p$ domain. The transformation was performed using 501 p -values. Aliasing effects were considerably attenuated through the weighting of traces with low p -values. After deconvolution the traces were transformed back into $x - t$ domain.
4. Deconvolution for recovering high frequencies. The deconvolution was applied in two time gates 200–2500 ms and 2400–4200 ms. The parameters for deconvolution were chosen for optimum resolution of the Rotliegend sediments with an operator length of 140 ms, prediction interval of 20 ms, and prewhitening of 1%.

Examples of the preprocessed seismograms are shown in Figure 2.3. Figure 2.3(a) shows a CMP gather located in the area between salt plugs. Reflections are visible for all traveltimes from 0 to 2.5 s. No AGC correction was applied to the seismograms. Therefore, the amplitudes of events below 3 s TWT are comparably low. In the CMP gather from the middle of a salt plug (Figure 2.3(b)), reflections are clearly visible only from 0 to 2 s TWT.

Tables of stacking velocities for specific CMP positions were kindly provided with the dataset by RWE Dea AG. I applied an interpolation scheme to obtain velocities between the provided points, smoothed, and saved them for every CMP and every time sample. The resulting model describes the stacking velocities in the dimensions of the stacked domain (CMP-TWT) shown in Figure 2.4(a). In the upper part of the model (0–1.5 s TWT) lateral velocity variations are minor. The stacking velocities are varying from 1.8 km/s at the surface to 2.7–3 km/s at 1.5 s TWT. Since the geological structure of the study area is complicated by the presence of salt, strong vertical and lateral velocity variations are visible at later times. Between CMP 1500 and 2000 the velocity increases up to 3.5 km/s, which corresponds to the salt plug in the left part of the profile as presented in the CMP stacked section (Figure 2.5). A similar velocity increase is

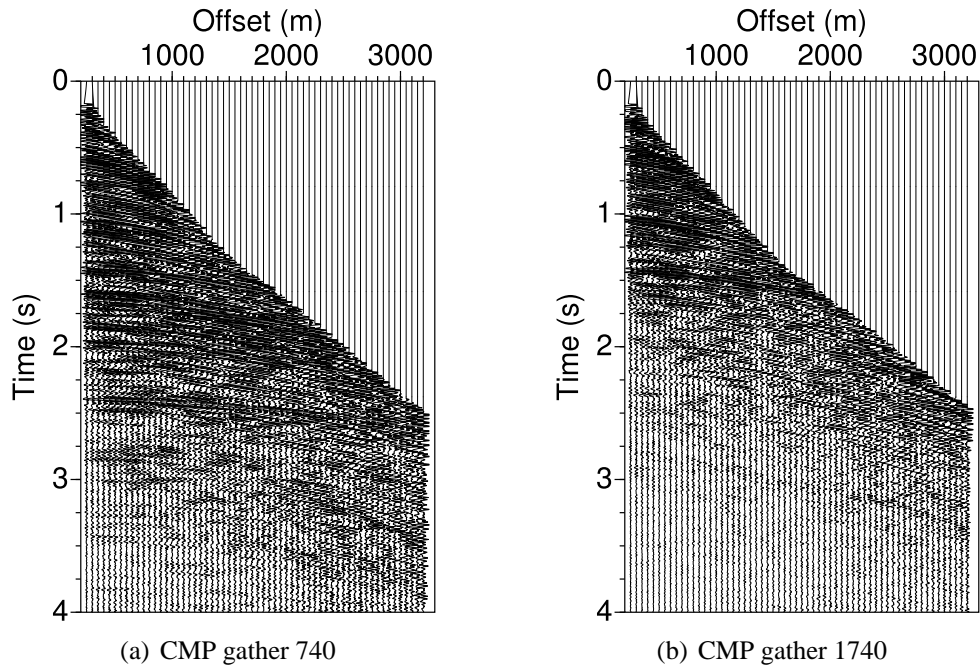


Figure 2.3: Marine data: examples of CMP gathers (a) from the area between salt plugs and (b) from a centre of a salt plug.

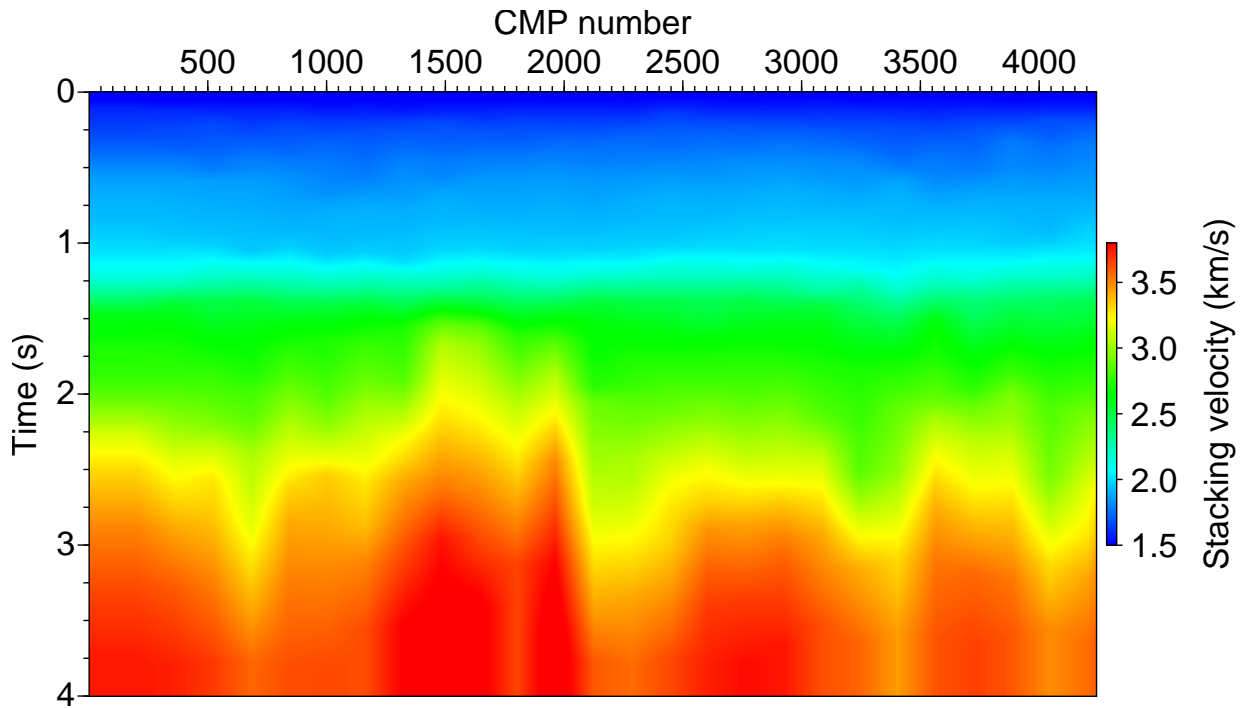
visible in the right part of the model, at CMPs 3500–3700. In the deeper parts of the model the stacking velocities increase monotonously and reach the values of 3.5–3.7 km/s at 4 s TWT.

2.3 CRS processing

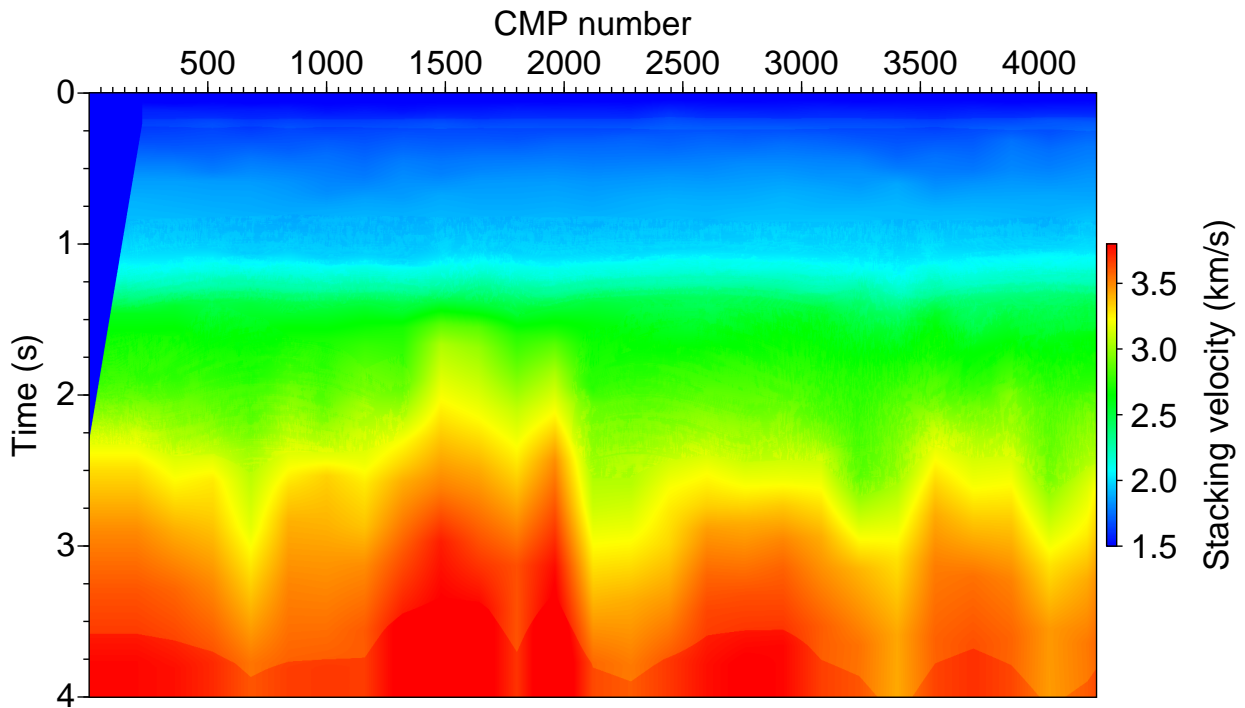
CRS processing of the dataset started with the search for the CRS parameters. As the simultaneous 3-parameter search would be computationally very expensive, I used the approach based on three one-parameter searches as described in Müller (1999), Jäger et al. (2001) and Mann (2002). The most important parameters for the automatic searches are summarised in Table 2.2. The maximum midpoint aperture was chosen according to the tests carried out by Petrologic. The following sections describe the results of the automatic CRS stack process.

2.3.1 Automatic CMP stack

In order to generate a CMP stacked section, the automatic search estimates the best-fit stacking velocities for the preprocessed CMP gathers. Since the information about the stacking velocities



(a) Model of stacking velocities provided with the dataset



(b) Model of stacking velocities obtained during the automatic CMP stack

Figure 2.4: Marine data: model of stacking velocities (a) provided with the dataset and (b) obtained from the automatic CMP stack. Velocities provided by the industry were used as guide functions for the stacking velocity search. Since only 1% of deviation from the guide values was allowed, the differences between the models are visible only in the deepest part (3.5–4 s TWT). In the upper and middle parts the models are almost identical.

Surface velocity	1500 m/s
Maximum deviation from reference stacking velocity model	1%
Maximum dip angle	60°
Minimum offset aperture	400 m at 0.2 s
Maximum offset aperture	3200 m at times > 2.3 s
Maximum midpoint aperture	500 m

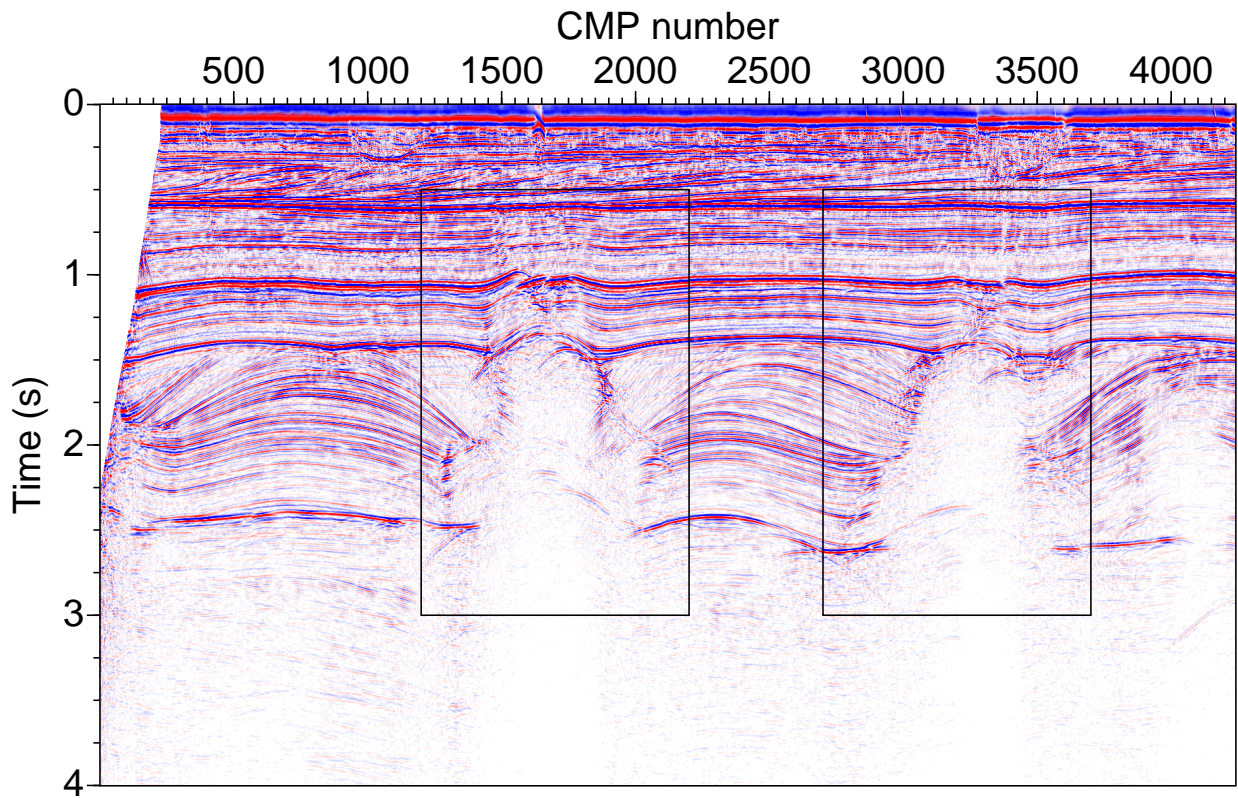
Table 2.2: Marine data: processing parameters used for the automatic CRS stack.

was provided by the industry, the search was constrained. The computation time was, therefore, significantly reduced. The stacking velocity model obtained from the provided velocity tables (for details see Section 2.2) was used as a guide. The range of tested velocities was restricted to 1% maximum deviation from the reference value, i.e., the search was carried out in the interval $[0.99 V_{NMO}; 1.01 V_{NMO}]$, where V_{NMO} is the stacking velocity in the reference model.

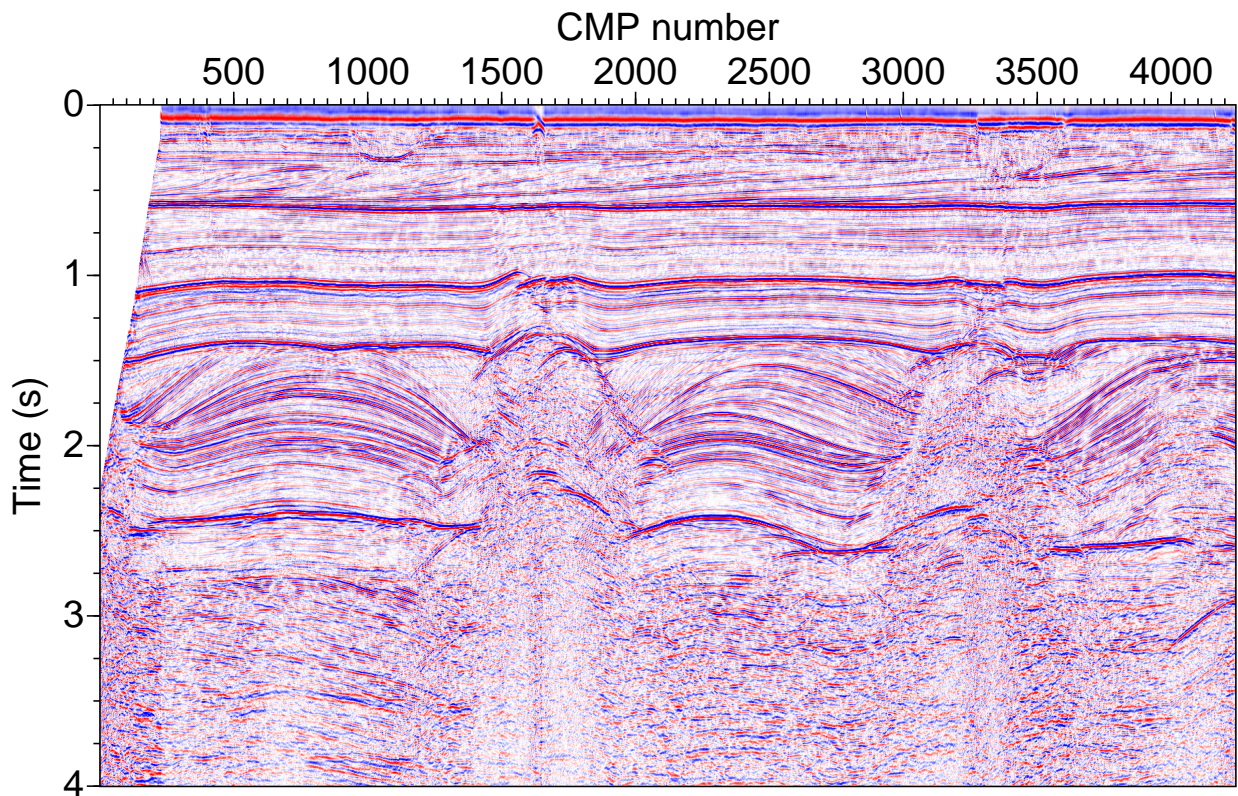
Figure 2.4(b) shows the final stacking velocity model obtained by the automatic search. Since only 1% of velocity variations from the guide values were allowed, there are only minor changes in the model compared to the reference model (Figure 2.4(a)). The deepest part of the model (3.5–4 s TWT) shows some fluctuations from the guide values. In the middle and upper parts both models are almost identical, which provides the result of automatic CMP stacking identical to the conventional CMP stack section.

CMP stacking of the preprocessed CMP gathers with the obtained velocity model provided the ZO time section shown in Figure 2.5(a). In order to improve the visibility of late-arriving events, an AGC with a 500 ms time window was applied to the stacked section (see Figure 2.5(b)). The amplitudes were balanced, making it possible to identify the reflections down to 4 s TWT. However, the AGC enhances the amplitudes of noise as well, so reflection events should be interpreted carefully, taking both sections without and with AGC into account.

The images of the most prominent reflections in the CMP stacked section (Figure 2.5) have good quality at the time levels 0–2 s TWT. Almost horizontal reflections at 0.5 s and 1 s TWT, corresponding to the Tertiary, are visible throughout the entire section. These horizons have continuous structure, and can be easily identified and correlated due to strong impedance contrasts. A set of dipping layers complicates the shallow part of the section at 0–0.5 s TWT. The base of Tertiary at 1 s TWT has a pull-up at CMP 1500–1700 crossed by a set of faults. The image of the middle part of the section at 1.5–2.5 s TWT is influenced by the presence of salt, and is complicated for the interpretation of the salt boundaries and reflections below. The base of Upper Cretaceous (1.5 s TWT) was deformed during the salt movements in the areas of CMP 1400–1900 and 2900–3500. Since the salt distorts the sediments above its top, the images of the top of salt are sometimes unclear. The images of Jurassic-Keuper-Muschelkalk sediments



(a) CMP stack



(b) CMP stack with AGC

Figure 2.5: Marine data: automatic CMP stack (a) without and (b) with AGC. The rectangles show the areas of the salt plugs, which are enlarged in Figure 2.7.

(1.5–2.5 s TWT) have anticline character between the salt plugs. The definition of the accurate position of the salt flanks in the unmigrated sections is complicated. Because of dipping layers, salt domes appear wider in the unmigrated sections than they are in reality. Moreover, a lot of conflicting dip situations are present at the salt-sediment boundaries.

The base of Zechstein (2.5 s TWT) is well imaged and well correlated. Below the anticlines the almost horizontal structure is only interrupted below the salt bodies. However, the correct position of the base Zechstein in the areas of the salt plugs (CMP 1500–1900 and 2900–3300, 2.3–2.5 s TWT) can be determined only after the depth migration. Prestack depth migration usually provides the best results for imaging of salt flanks and sub-salt structures.

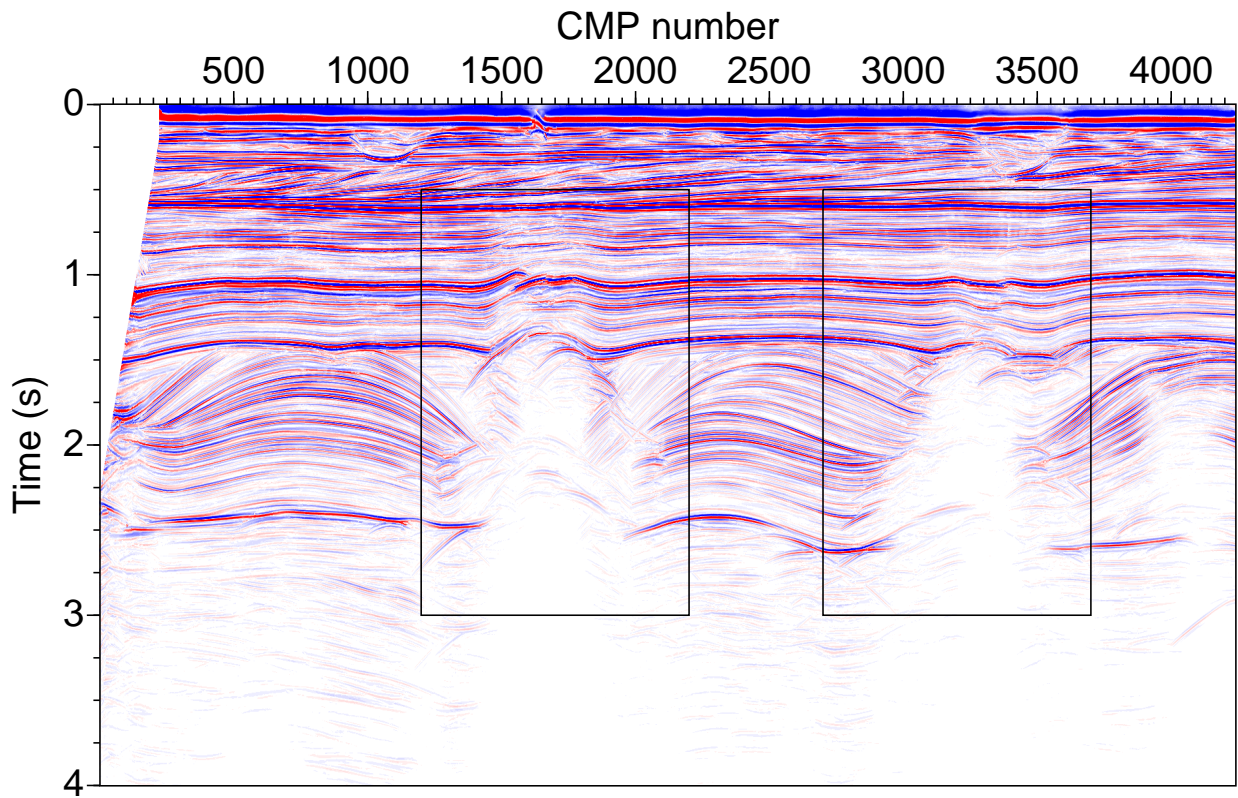
Reflections below 2.5–3 s TWT in the CMP stack section are poorly imaged as the S/N ratio is relatively low. Energy dispersal within the salt bodies leads to an increased noise. Moreover, reflections that most likely belong to multiples complicate the definition of sedimentary boundaries in the deeper part. Because of the energy loss with depth the correlation of horizons is complicated in the areas below 3 s TWT.

2.3.2 Automatic CRS stack

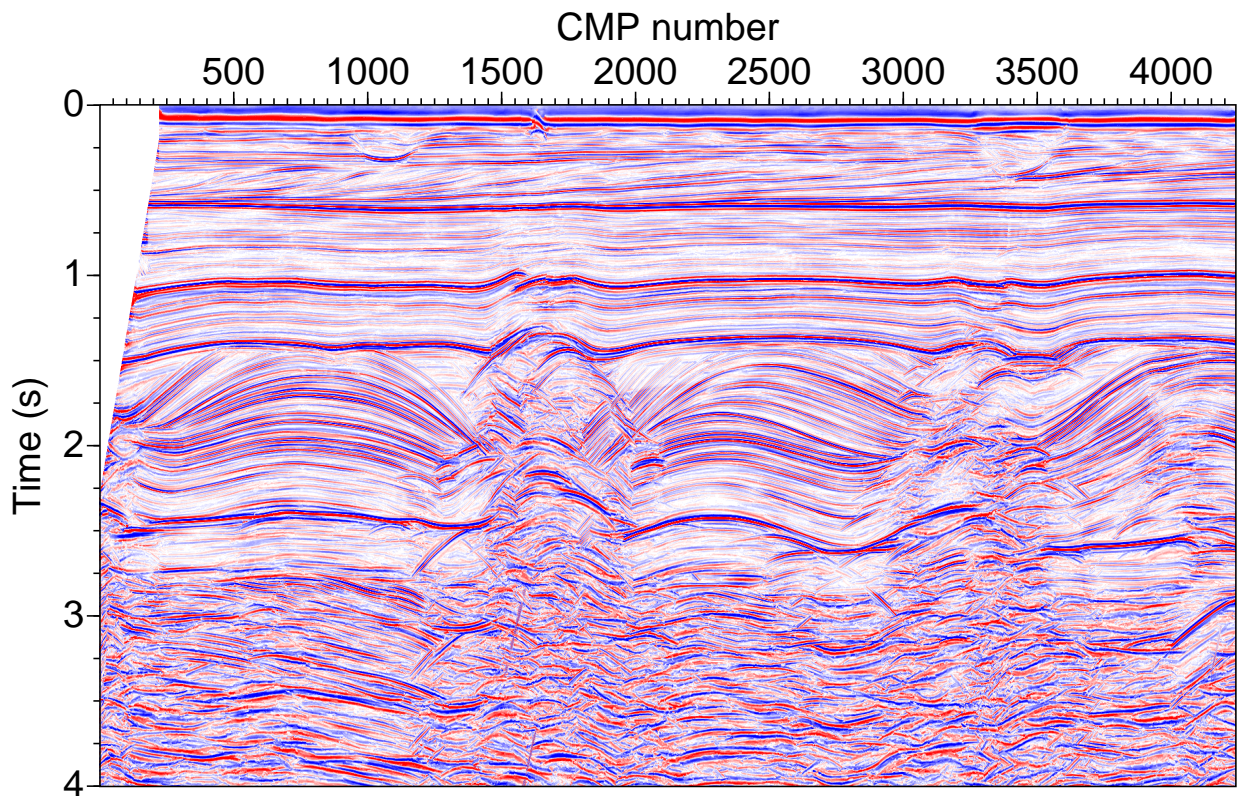
After the generation of the CMP stacked section, the automatic searches provided the CRS stacking parameters for the generation of the CRS stack section. Figure 2.6 shows the resulting automatic CRS stack section without and with AGC correction. The results should be compared with the conventional CMP stacked sections as presented in Figure 2.5.

Most significantly, the continuity of reflection events in the CRS stack sections increased greatly, and the S/N ratio appears much higher compared to the CMP stacked sections. This quality improvement is observed at the top of the salt plugs and in deeper parts (> 2.5 s TWT) as well as in the interior of the salt plugs. Although the precise definition of the salt flanks position is still complicated, the images of the sediments surrounding the salt are greatly improved in the CRS stack section (compare zoomed images in Figure 2.7) even permit the interpretation of the salt-sediment interfaces in the non-migrated time sections. The images of seismic events below 2.5 s TWT in the CRS stack section are improved compared to the CMP stack section.

Figures 2.8 to 2.11 display the CRS semblance section and three CRS parameter sections. Most reflections visible in the CMP and CRS stacked sections can be identified in the CRS semblance section as well (see Figure 2.8). With increasing recording time the semblance decreases because of the lower S/N ratio and geometrical spreading loss. However, the reflection events can be distinguished from the noise for times 0–2.5 s TWT. The areas of salt plugs have lower semblance because of energy dispersal, but the bottom of the salt and the horizons around the salt flanks are



(a) CRS stack



(b) CRS stack with AGC

Figure 2.6: Marine data: automatic CRS stack. The S/N ratio is increased compared to the automatic CMP stack (Figure 2.5). The rectangles are enlarged in Figure 2.7.

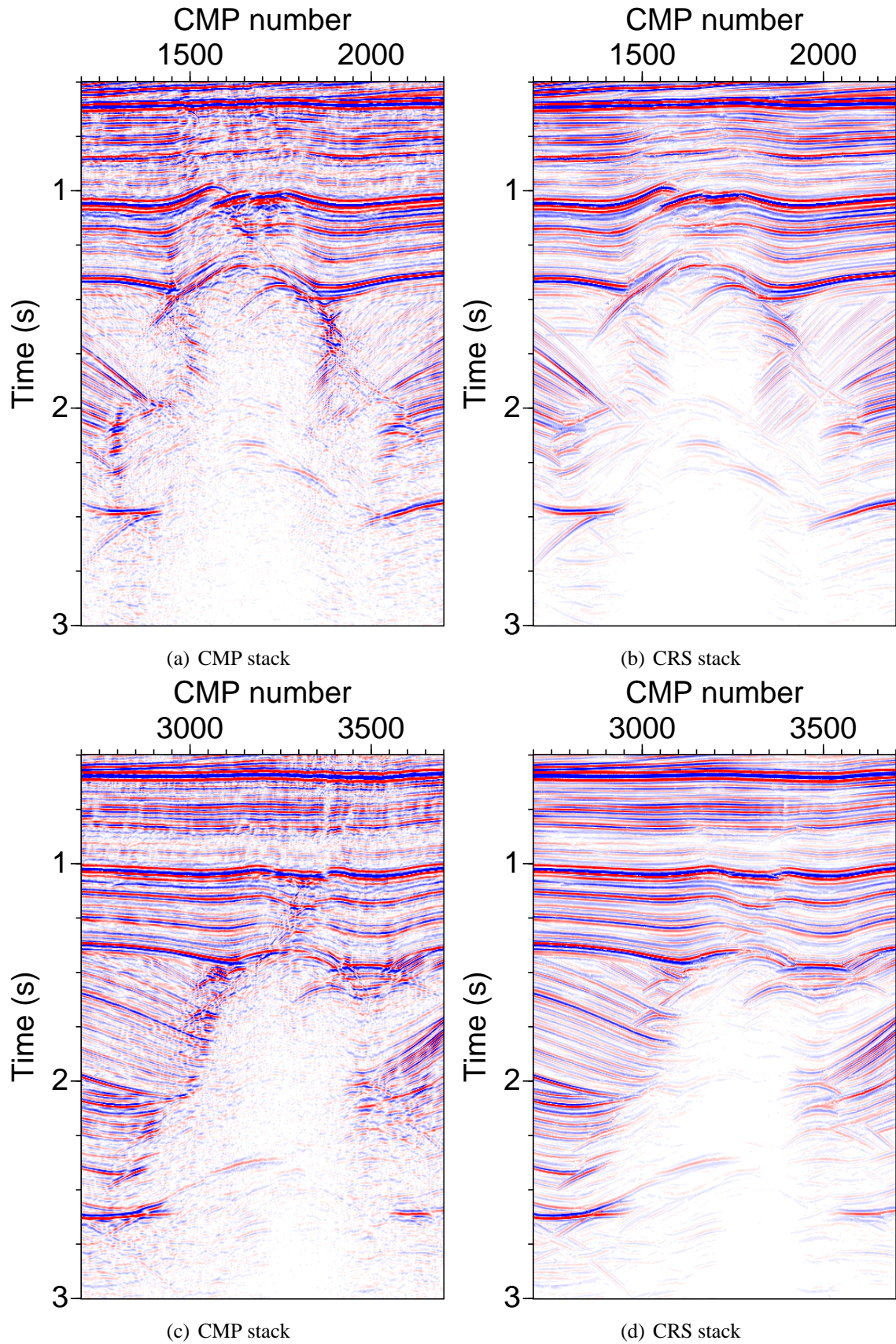


Figure 2.7: Marine data: zooms of the salt plugs as presented in Figures 2.5 and 2.6. The automatic CRS stack (b) and (d) provided images with higher S/N ratio. Reflections appear more continuous and the salt-sediments boundaries are easier to identify compared to the CMP stacked section (a) and (c).

clearly visible.

Figure 2.9 displays the angle of emergence, α , from -10° to 10° . The upper part of the data contains almost horizontal reflections with angles of emergence around 0° . At the flanks of the anticline structures and in the areas around the salt plugs the angles increase up to $\pm 10^\circ$. The diffractions in the semblance section below 3 s TWT lead to higher values of emergence angle up to 20° – 40° , but these values were clipped for displaying in order to show the slight variations in the upper part of the section. However, the diffractions are visible within and below the salt around CMP 1500 at times 1.5–4 s TWT as a set of bright red and blue stripes.

Figure 2.10 shows the radius of curvature of the NIP-wave, R_{NIP} . In a constant velocity medium this parameter is associated with the reflector depth, so R_{NIP} is increasing smoothly with increasing TWT. However, the complexity of the data with the presence of anticline structures and salt plugs results in values of R_{NIP} significantly different from the expected reflector depth. The true reflector position can be reconstructed only after a seismic inversion procedure, e.g., using the NIP-wave tomography followed by depth migration.

Figure 2.11 depicts the radius of curvature of the N-wave, R_N . As a measure of reflection curvature, large values of R_N correspond to almost plane reflectors. Most of the reflections in the upper part of the section are almost flat and, therefore, have very large values of R_N . In order to show the reflections in the deeper part of the section, clip values of $\pm 30km$ were used for display.

Finally, Figure 2.12 illustrates the number of traces used by the CMP and CRS stacks to simulate one sample in the ZO sections. The CRS stack used up to 120 times more traces compared to the CMP stack. This significant difference resulted in the increased S/N ratio of the CRS stack section.

2.3.3 NIP-wave tomographic inversion

After the estimation of CRS parameters (α , R_{NIP} , R_N) and the generation of the CRS stacked section, I prepared the input data for the NIP-wave tomographic inversion. This approach, as described in Duveneck (2004), operates with CRS parameters of ZO points picked in the stacked domain. In order to obtain the ZO points, I picked the most important primary reflections in the CRS stack section per hand. An automatic picking procedure was not applied to the marine dataset, but an example of its practical usage can be found below in Chapter 3. Picking per hand provides the flexibility in choosing low-coherent events at the salt-sedimentary boundaries and also in the sub-salt areas. After the picking the CRS parameters corresponding to the chosen ZO points were automatically extracted by the software provided by the WIT consortium.

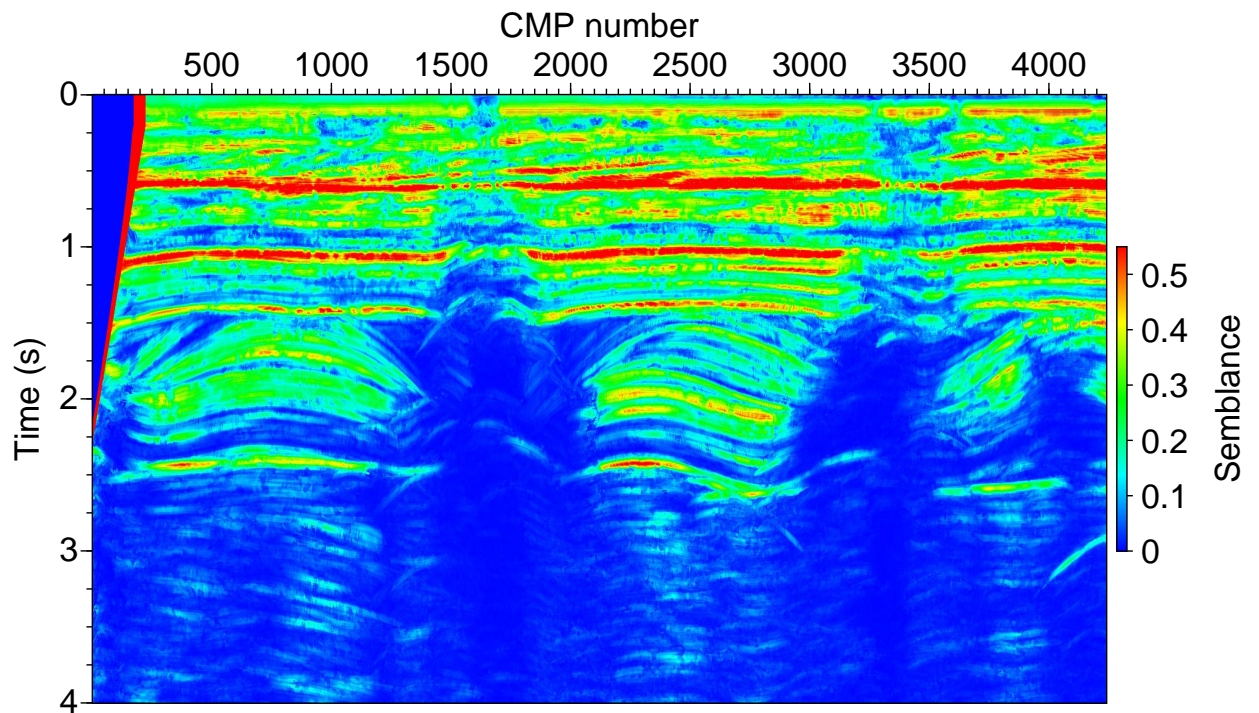
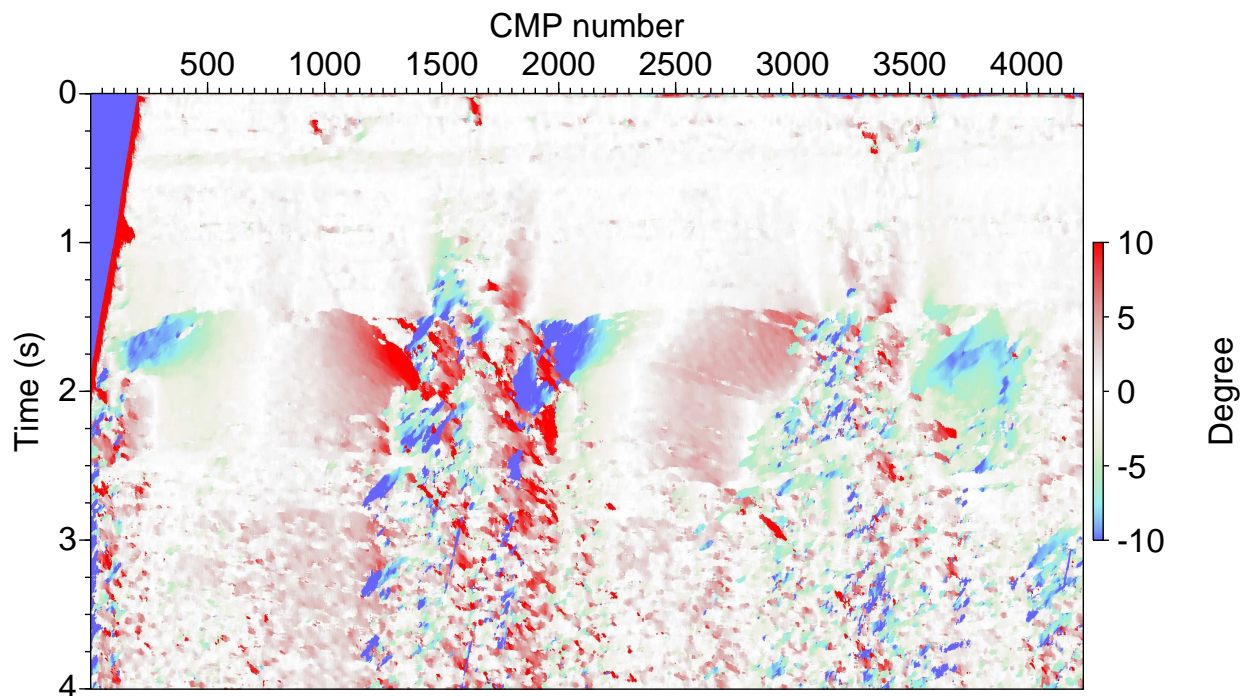


Figure 2.8: Marine data: CRS semblance section.

Figure 2.9: Marine data: angle of emergence, α .

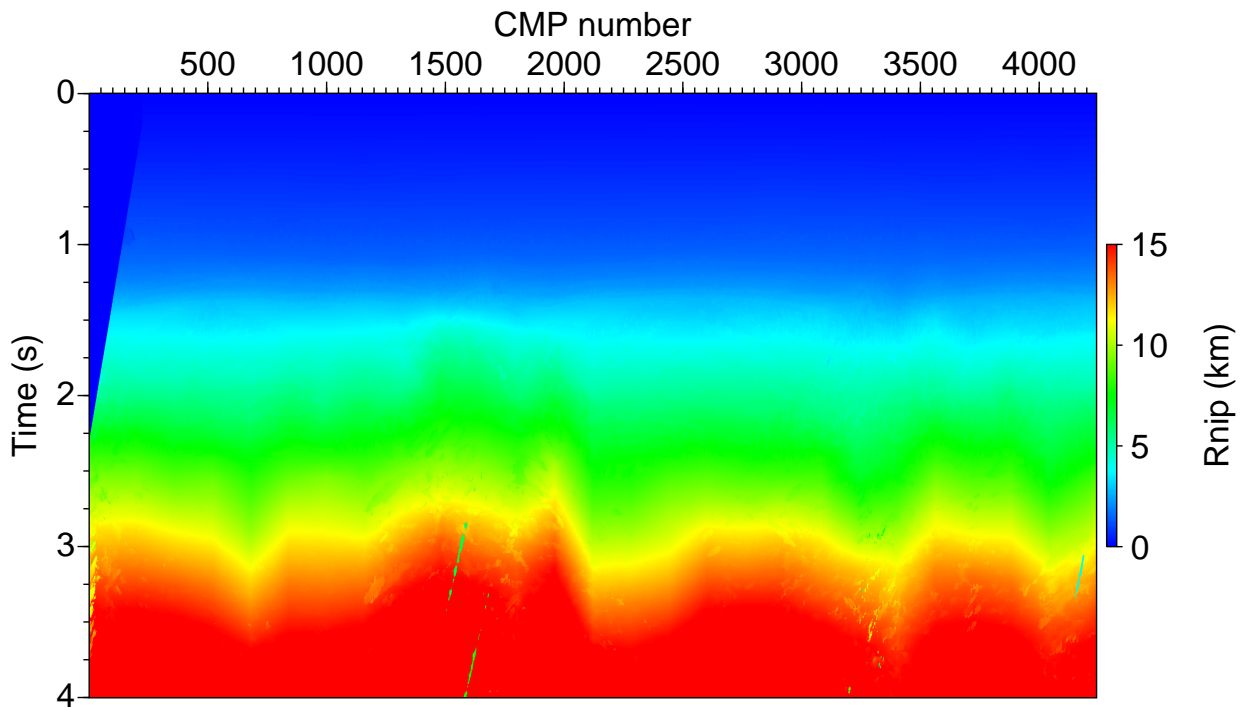


Figure 2.10: Marine data: radius of curvature of the NIP-wave, R_{NIP} .

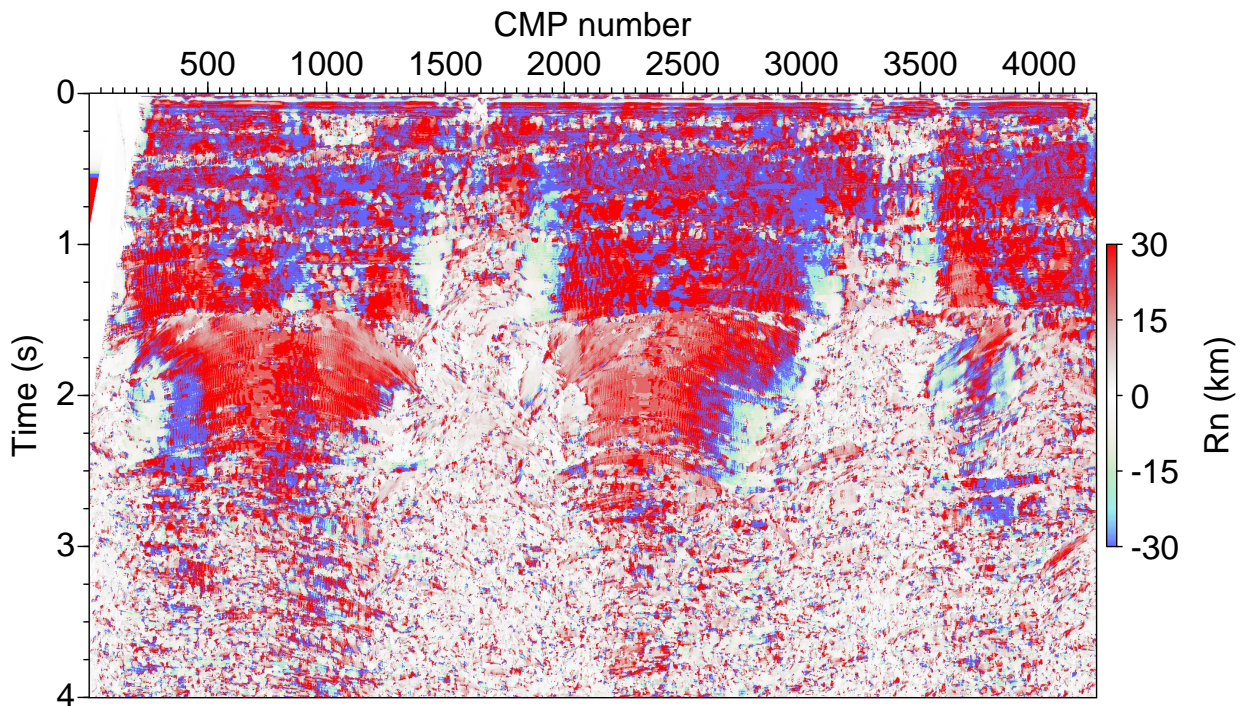


Figure 2.11: Marine data: radius of curvature of the N-wave, R_N .

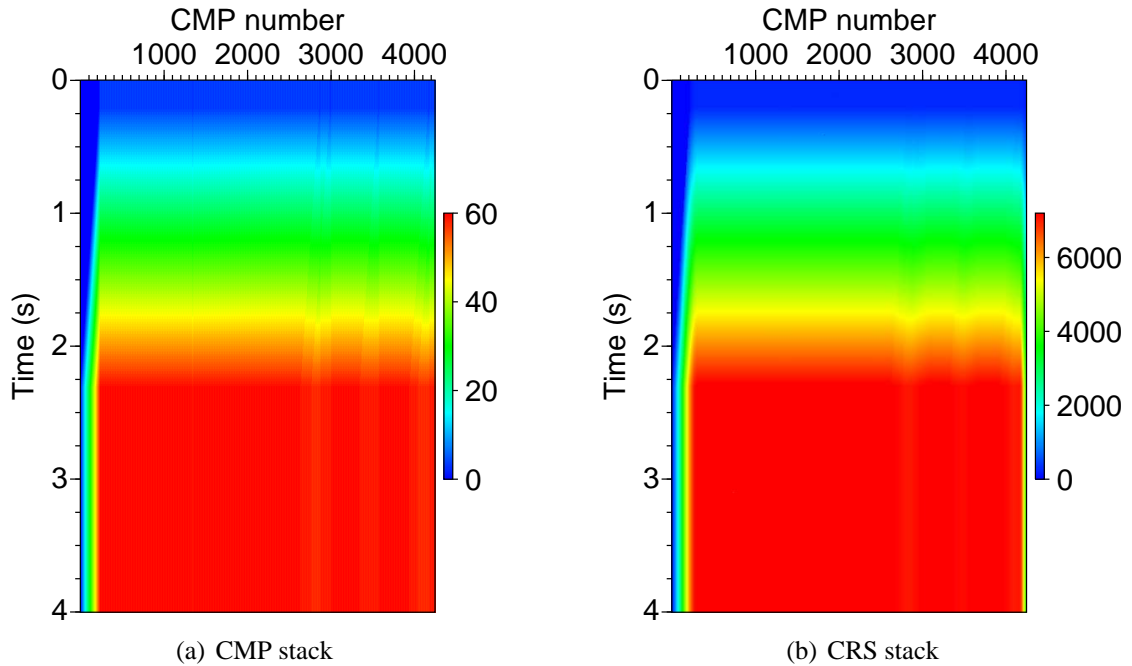


Figure 2.12: Marine data: number of traces used by the automatic CMP and CRS stacks to image one ZO time sample. Note the different scales. In the bottom of the section the CRS stack comprises up to 120 times more traces compared to the CMP stack.

Although the ZO points were picked manually, the input data for the tomographic inversion needed to be tested with respect to the reliability of the corresponding CRS parameters (see Chapter 1 for details). After removing outliers, about 1000 points remained. The resulting ZO points are shown in Figure 2.13. Figure 2.13(b) shows the distribution of picked ZO points over the geological structures where the most prominent reflections were chosen for picking. Starting from the sea bottom at ~ 0.1 s TWT the base Miocene at 0.5 s TWT, base Tertiary at 1 s TWT, and base of Upper Cretaceous at 1.5 s TWT were picked. Since these horizons are almost horizontal and are only rarely interrupted by faults, the precise picking of these reflections was easy. Picking of the top of salt and salt flanks, however, was complicated by the presence of faults, diffractions, and conflicting dip situations. The benefit of the NIP-wave tomography in these areas is that it is not necessary to follow the horizons continuously, but independent reflection elements may be chosen for the inversion. Therefore, the bottom of the salt at CMP 1700–1900 CMP and 3000–3500, 2.5 s TWT was picked separately, without exact correlation with the neighbouring horizons.

Most characteristic events within the anticline structures at 1.5–2 s TWT were picked without the precise correlation of the stratigraphy, but with respect to the highest coherency and maximum amplitudes. The aim of picking these events was to follow the shape of the anticline structures with approximately constant pick spacing, which is preferable for stable tomographic inversion. Since the S/N ratio of the data decreases with increasing recording time, the picking of reflec-

tions is much more complicated below 2.5 s TWT in the CRS stacked section. Therefore, only sparse points with the highest values of semblance and amplitude in the deeper part of the data were picked. For more precise picking the section with AGC-corrected amplitudes was used, as presented in Figure 2.5(b).

The final check of picked data was carried out with respect to the reliability of CRS parameters. The picks corresponding to multiples and other noise must be identified and, if necessary, removed. The quality of input data is very important for the NIP-wave tomographic inversion. The data were quality controlled using the plots of the parameter M_{NIP} (see Chapter 1) and stacking velocities with respect to the traveltimes (see Figure 2.14). A characteristic decrease of V_{NMO} , as normally observed for long-path multiples, may result into a corresponding increase of M_{NIP} value at the considered time. Therefore, the plots of M_{NIP} against traveltimes that deviate significantly from the main trend can be considered as multiples. Figure 2.14(a) shows, however, excellent point distribution along the main trend, and the picks do not need any further editing. This is partly the result of the manual picking procedure. Also the preprocessing of the data, carried out by the industry, significantly attenuated the multiples in the upper part of the section. The empty areas in Figure 2.14(a) between the clouds of picks are the results of manual picking when sparse horizons are chosen in the ZO section (see Figure 2.13(b)). Since there are no ZO points picked between 0.1 s and 0.5 s TWT, 0.6 s and 0.7 s TWT etc, these time intervals contain no data in Figure 2.14. Figure 2.14(b) outlines the stacking velocities corresponding to all picked events against traveltimes. The plot shows a very good velocity distribution for the first four picked horizons down to the base Tertiary at ~ 1 s TWT. Starting from 1.5 s to longer traveltimes, there are some velocity fluctuations around the main trend, but no areas of significantly lower velocities are found, which confirms the absence of multiples. Therefore, the picked data were suitable as input for the NIP-wave tomographic inversion.

The depth velocity model estimated during the tomographic inversion was defined on a grid of 55 x 41 nodes with a constant lateral spacing of 500 m and depth spacing of 200 m. A near surface velocity of 1700 m/s and a constant velocity gradient of 0.5 s^{-1} were chosen as an initial model for the inversion. The thin water layer of about 20 m does not influence the model significantly, so the velocities of the sub-water sediments was taken for the near-surface. The parameters of the NIP-wave tomographic inversion are summarised in Table 2.3. A total of 10 iterations were carried out. After every iteration the input ZO points were *back-propagated* to their corrected position in space. Figure 2.15 shows the depth velocity models plotted together with the corresponding back-propagated picks after exemplarily chosen iteration steps.

After every iteration the cost function S was determined that represents the deviation of the predicted data from the picked data. Figure 2.16 shows that the cost function decreases continuously. After the seventh iteration the changes in velocities were minor. The velocity model obtained after ten iterations was taken as a final model for depth migration.

Figure 2.17 represents this final NIP-wave tomography model with corresponding back-propagated

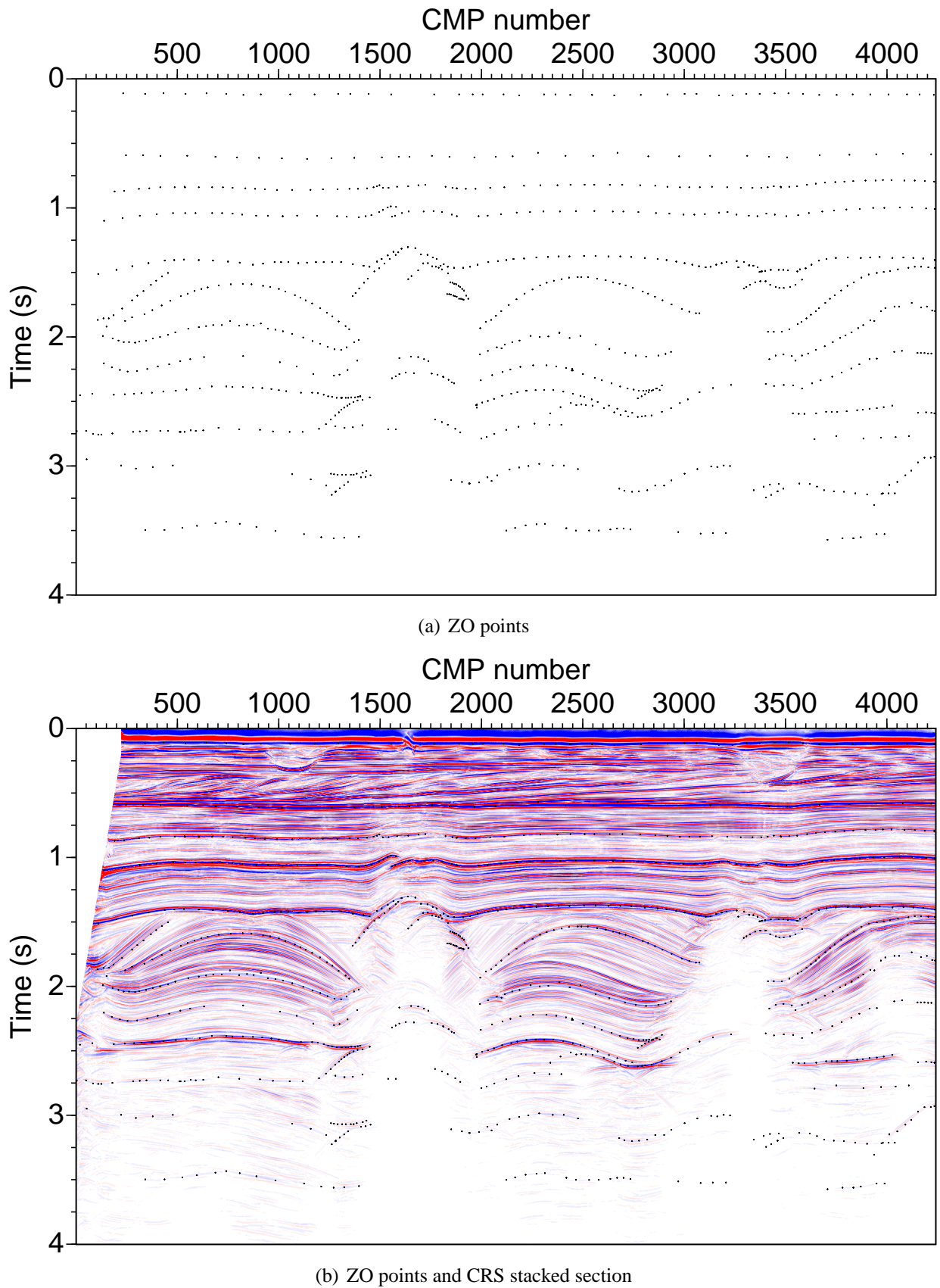


Figure 2.13: Marine data. (a) Input picks (black dots) for the NIP-wave tomographic inversion. (b) The CRS stacked section was used for manual picking of reflection events.

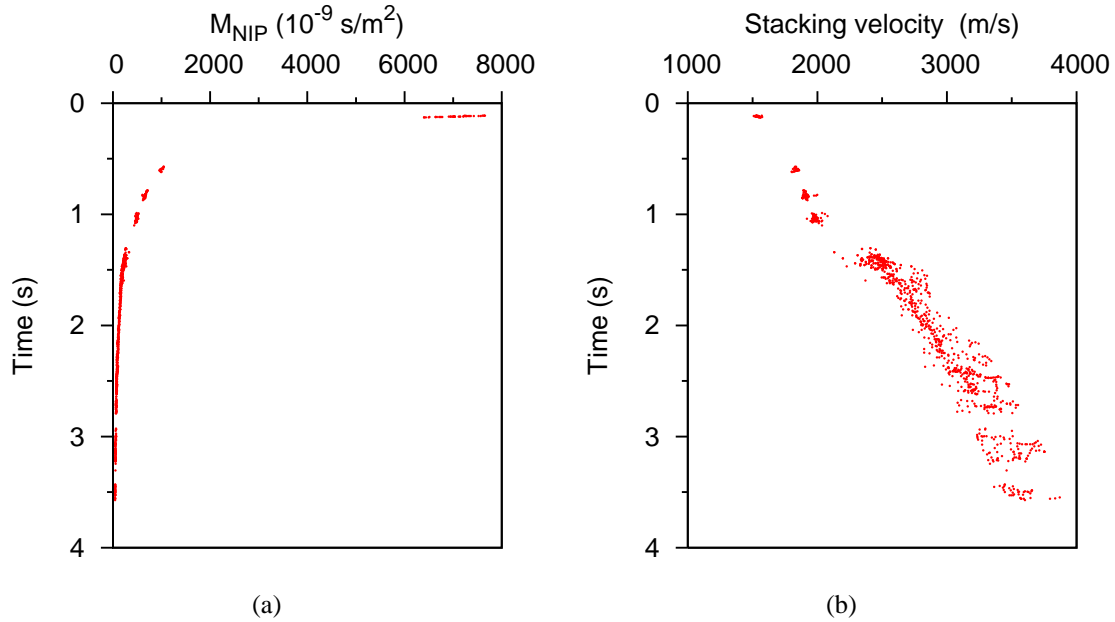


Figure 2.14: Marine data: quality control of input picks for NIP-wave tomography. (a) The parameter M_{NIP} and (b) stacking velocities are computed for each picked ZO point from the corresponding CRS parameters. Fluctuations of velocities of up to 500 m/s for the picks at later traveltimes correspond to the lateral variations in the stacking velocity model (Figure 3.3(b)). Significant deviation from the main trends of points distribution is not observed, which confirms the reliability of picked data and the absence of picks corresponding to long-path multiples.

Lateral grid spacing	500 m
Depth grid spacing	200 m
Number of nodes in lateral direction	55
Number of nodes in depth direction	41
Initial model:	
surface velocity	1700 m/s
gradient	0.5 s^{-1}
Number of tomographic iterations	10

Table 2.3: Marine data: parameters of the NIP-wave tomographic inversion.

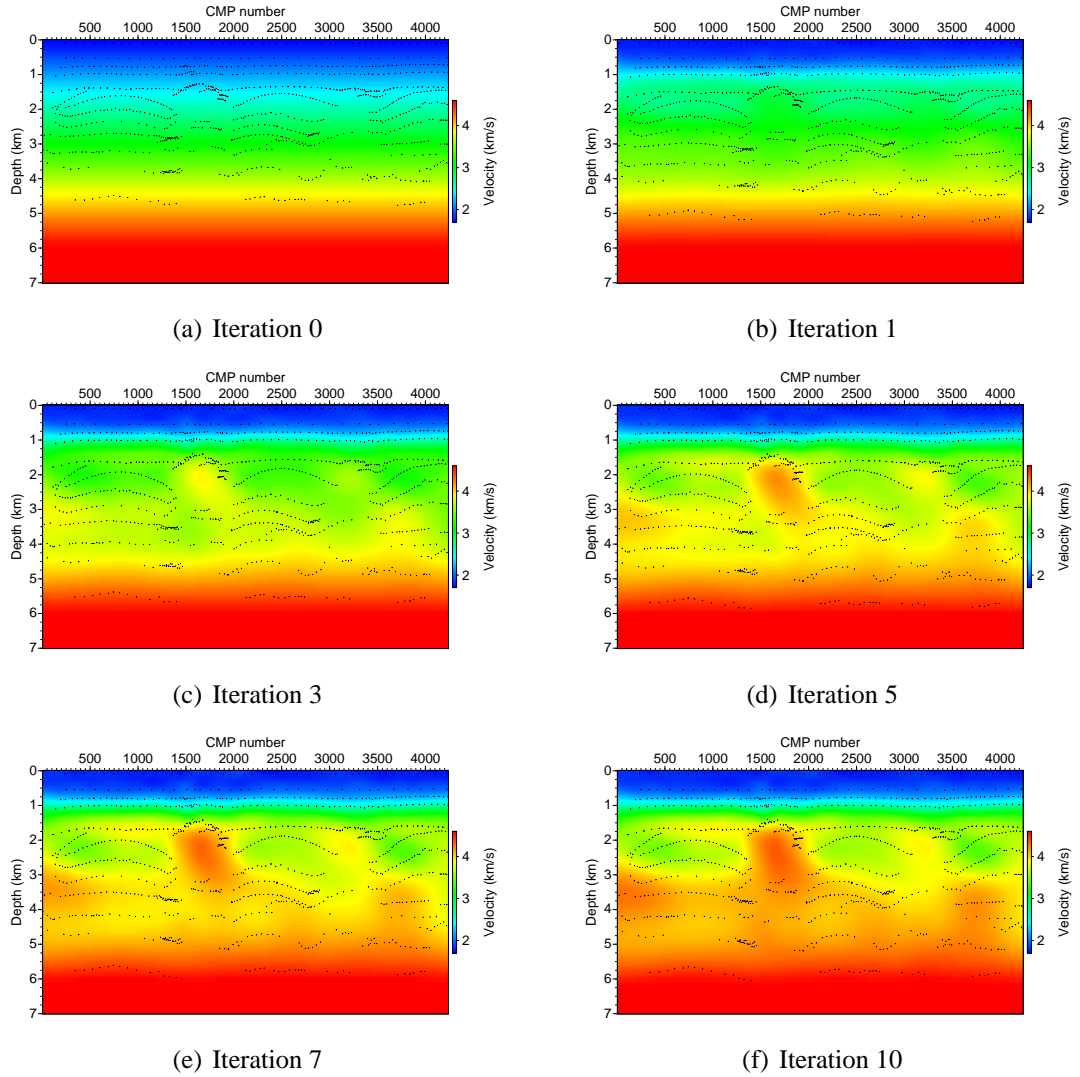


Figure 2.15: Marine data: depth velocity models with corresponding back-propagated picks computed after exemplarily chosen iteration steps. Starting from the initial gradient (a), the model is continuously updated after every iteration. The final model obtained after 10 iterations is enlarged in Figure 2.17.

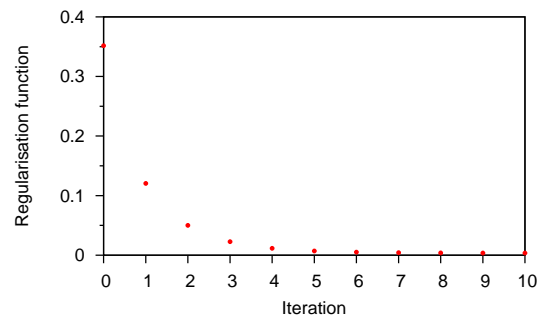


Figure 2.16: Marine data: value of the cost function S computed after every tomographic iteration. The changes after the seventh iteration are minor.

picks. As the model is described by B-splines it appears smoothed in contrast to conventional layer-based models. However, the main geological structures can be recognised in Figure 2.17. Starting with the initial velocities of ~ 1.7 km/s at the surface, the values smoothly increase up to 2.1–2.3 km/s at ~ 0.9 km depth and reach 2.7–2.9 km/s for the base Tertiary located at ~ 1 km depth. The interval from 1 km to 1.8 km depth corresponding to the base Upper Cretaceous – base Tertiary is described by a velocity increase to 3.5–3.8 km/s. Slight lateral velocity variations are visible in the upper part of the model. The deeper part from 1.8 km to 4 km is influenced by the presence of salt domes and anticline structures. From CMP 1300 to 2000 at 1.6 to 4 km depth a high velocity zone is observed with velocities reaching 4.3–4.4 km/s. This zone corresponds to the left salt plug as presented in Figures 2.5 and 2.6. The salt plug located in the right part of the sections is characterised by velocity values up to 3.8–3.9 km/s around CMP 3300.

It must be mentioned that the velocities obtained by NIP-wave tomographic inversion may differ from the interval velocities of the corresponding sediments. For example, interval velocities of 4.5–4.6 km/s, typical for salt, are not observed in the model, which is the result of smoothing and the presence of sediments in the salt. Therefore, this model should not be used for a geological interpretation. It is suited for the depth migration of seismic data. However, around the salt plugs at the depth 1.8–3 km the NIP-wave velocities are close to the expected interval velocities of corresponding sediments (Bunter to Upper Cretaceous), reaching 3.3–3.5 km/s. Deeper sediments down to base Zechstein are characterised by velocities of 4–4.2 km/s. Sparse distribution of input picks used by the tomographic inversion leads to minor lateral velocity variations in the deeper part of the model. A zone of slightly lower velocity values compared to the surrounding sediments is observed between 3.5–5 km depth. The deeper part up to 5 km is characterised by the values of velocities that coincide with the initial gradient model used by tomography.

Despite the fact that the NIP-wave tomography model should not be used for exact interpretation, it certainly provides complementary information. The distribution of back-propagated picks plotted over the model in Figure 2.17(b) shows an approximate depth of reflector elements.

2.4 Depth migration

Kirchhoff depth migration of the marine dataset was carried out using the ProMAX software. Poststack depth migration of the CRS stacked section as well as prestack depth migration of the CMP gathers were carried out. The CMP spacing of the output depth-migrated sections is 6.25 m, the same as of the time-stacked sections. The seismograms were migrated up to maximum frequencies of 65 Hz and maximum 7 km depth with the depth sample interval of 6 m, which was the same as used by the industry. Maximum amplitude ray tracing was used to produce the Green's functions. The maximum emergence angle was 70° . For the migrations, the NIP-wave tomography model as presented in Figure 2.17 was used. The aperture width of the prestack

CDP spacing in output field	6.25 m
Maximum frequency	65 Hz
Depth sampling interval	6 m
Maximum depth to migrate	7000 m
Migration aperture	1800 m for PostSDM 3600 m for PreSDM
Maximum emergence angle to trace rays	70°
Velocity model sample interval	100 m
Method for generating the Green's function	Maximum amplitude ray tracing

Table 2.4: Marine data: processing parameters for depth migration.

depth migration was 3600 m, which is the value used by the industry, whereas the aperture of the poststack depth migration of the CRS stack was reduced to 1800 m, in order to reduce migration artifacts. The depth migration parameters are summarised in Table 2.4.

2.4.1 Poststack depth migration of the CRS stack

Figure 2.18(a) shows the poststack depth migration of the CRS stack using the NIP-wave tomographic model. The shape of the salt structures corresponds to the distribution of back-propagated picks as presented in Figure 2.18(b). All picked reflectors above the salt plugs coincide exactly with the picks. The base Zechstein at about 3.5–4 km depth is also well correlated. However, the salt flanks sometimes contradict the back-propagated picks. This is most likely the result of the smooth velocity description used in tomographic inversion with coarse node spacing (500 m in lateral and 200 m in vertical directions), which is not small enough to describe such strong velocity variations. Also, non-hyperbolic reflections at the salt-sedimentary boundaries may result in these deviations.

As expected, both salt plugs appear laterally compressed in the poststack depth-migrated section compared to the time sections (see Figures 2.5(a) and 2.6(a)). Since the depth migration process handles lateral velocity variations, the images of complex structures are corrected with respect to their actual lateral position. Depth migration collapses diffractions; so the areas of salt flanks where a lot of noise is present in the time sections are better imaged in the depth migrated section. The images of reflectors close to the top of salt plugs are improved compared to the time-stacked sections.

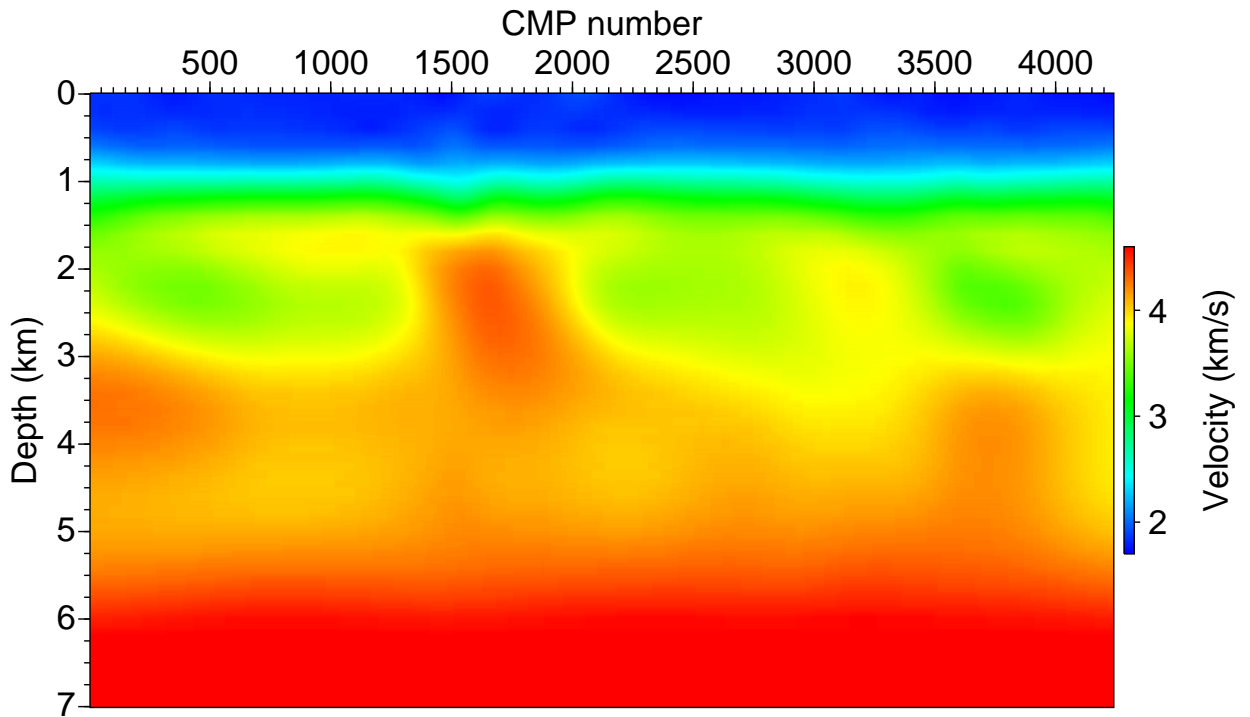
2.4.2 Prestack depth migration

Figure 2.19 shows the Kirchhoff prestack depth-migrated section. Although the poststack depth-migrated section has higher S/N ratio compared to the prestack result, the latter shows much more details that are important for interpretation. Despite the fact that some reflectors appear less continuous compared to the poststack depth migration, areas of improvement are visible. The fault systems located above both salt diapirs at 1–1.8 km depth around CMP 1600 and 3300 are clearly identified in the PreSDM section. The images of salt diapirs, their flanks and the internal salt structures are greatly improved. PreSDM takes the strong lateral velocity variations into account to generate the prestack depth migrated gathers (CIGs). Therefore, stacking of the CIGs usually produces better images than the poststack depth migration. Moreover, the accuracy of the velocity model used by migration is estimated by the flatness of events in the CIGs.

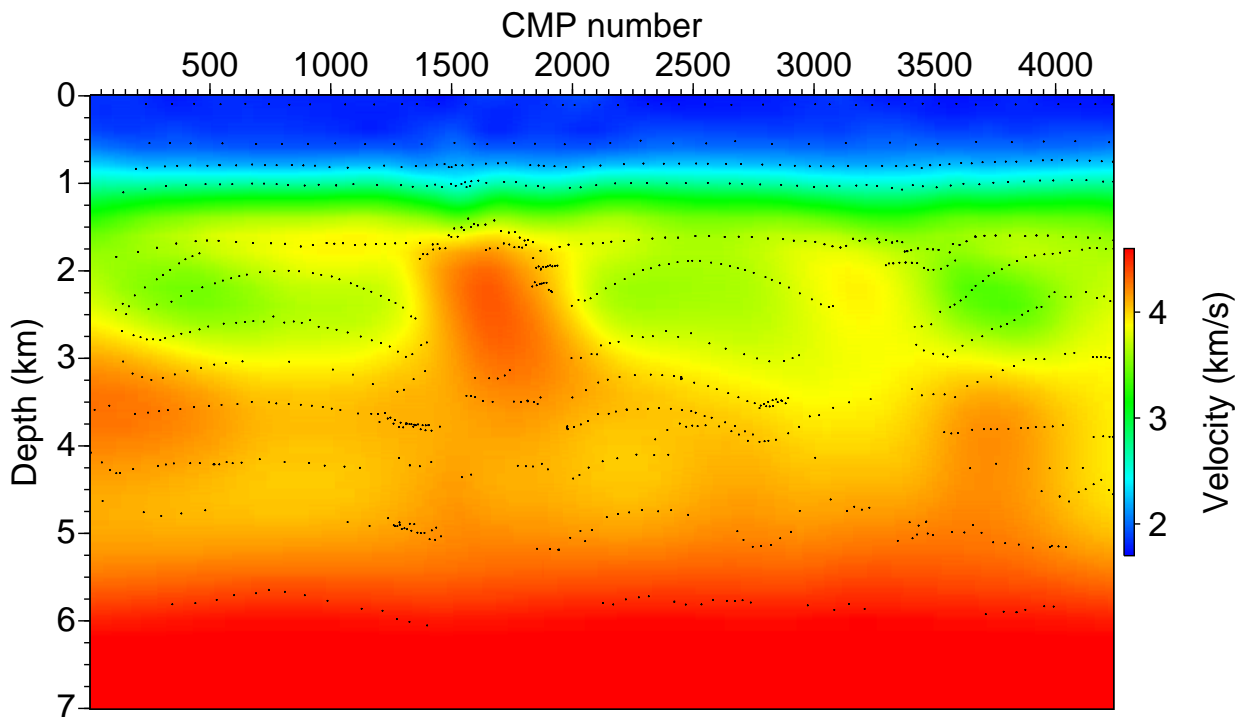
Figure 2.20 shows the CIGs of the marine dataset migrated with the NIP-wave tomographic model. The result shows very good flatness of gathers at 0.5 to 3.5 km depth. It must be noticed that the seismograms are plotted up to 3200 m offset, and up to 7 km depth, so the vertical/horizontal ratio of each CIG is approximately 10:1. Using this scale, the residual moveouts are overemphasised. The positive residual moveout observed at base Tertiary at ~ 1 km depth can be associated with a too high initial velocity gradient used by the tomographic inversion, which does not fit the upper part of the section perfectly, but is suited for the middle part of the section from 1.5 to 3.5 km depth. In other parts of the CIGs, residual moveout is not visible, which confirms the consistency of the depth velocity model with the data.

2.5 Conclusions

The presented CRS technique has demonstrated the potential to produce high-quality images of marine seismic data. The automatically-generated CRS stack shows a higher S/N ratio and improved images of salt plugs compared to the conventional CMP stack sections. Moreover, the CRS parameters estimated during the automatic searches can be used to construct a depth velocity model suitable for depth migration. The model was estimated by the NIP-wave tomographic inversion. Picking of input data for the inversion was performed in the CRS stacked section with its high S/N ratio. Reflector elements were picked independently, which is a great benefit when working with complex salt structures. Poststack depth migration of the CRS stack and prestack depth migration produced high-quality sections that can be used as a supplementary material for a geological interpretation. Therefore, CRS stack and NIP-wave tomography techniques provide fast generation of time and depth images of complex geological environment.

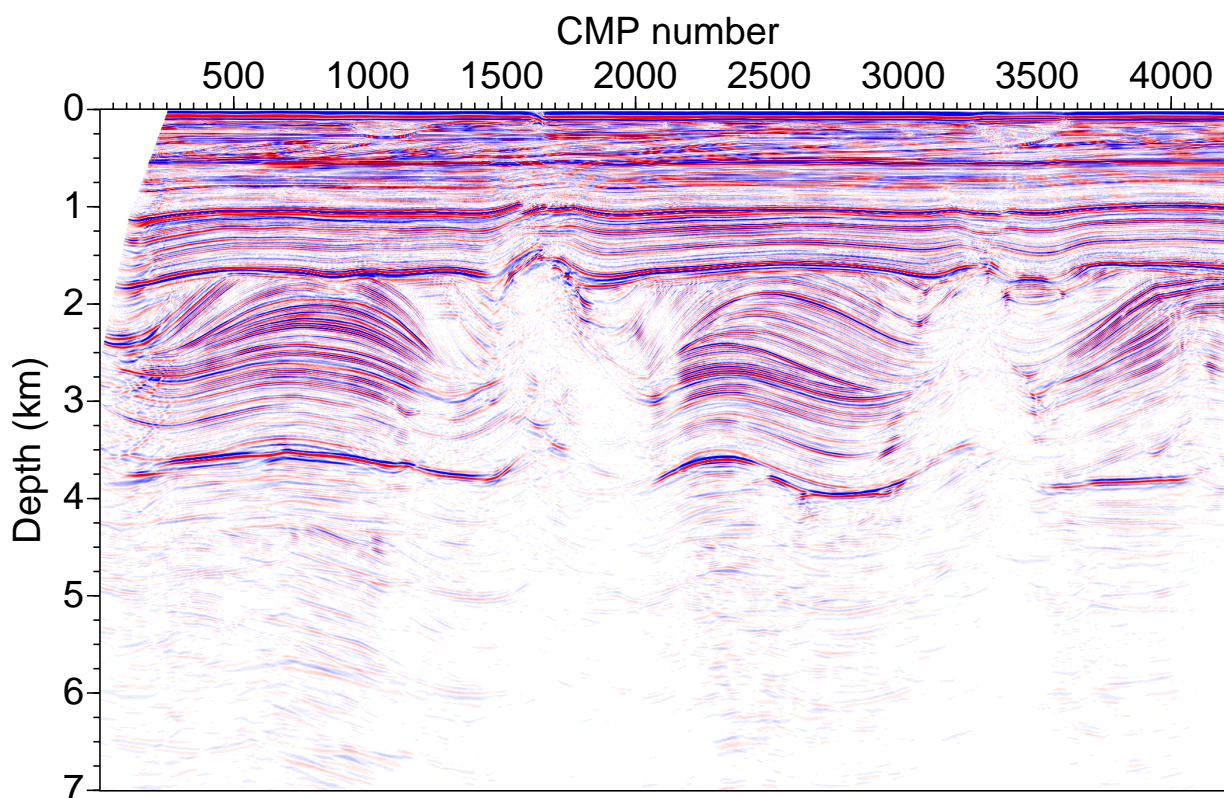


(a) Depth velocity model

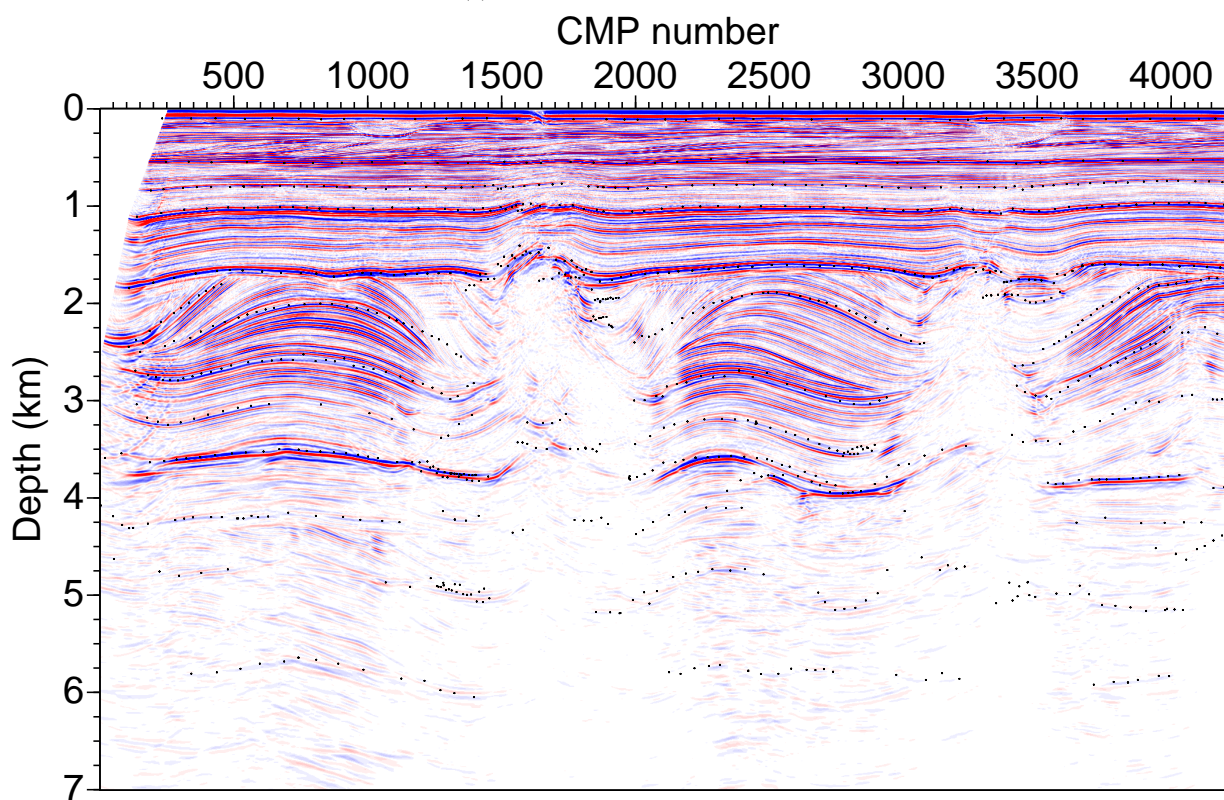


(b) Depth velocity model with back-propagated picks

Figure 2.17: Marine data: reconstructed smooth velocity model with back-propagated picks, obtained after ten NIP-wave iterations. The picks coincide with the discontinuities in the velocity model. Two zones of high velocity values reaching 4–4.3 km/s in the middle part of the model (CMPs 1500 and 3200) correspond to the salt plugs as seen in the stacked sections (Figures 2.5 and 2.6). The model is used for the depth migration of the seismograms.

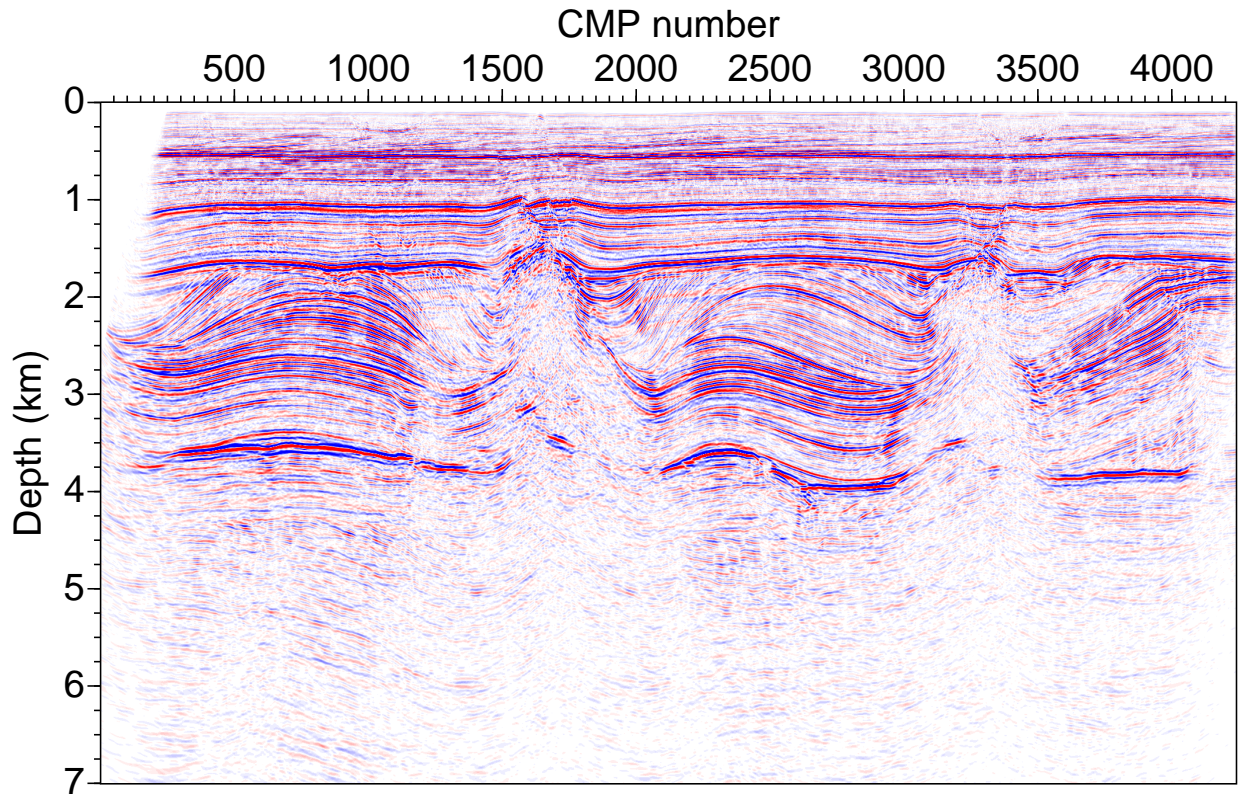


(a) PostSDM of the CRS stack

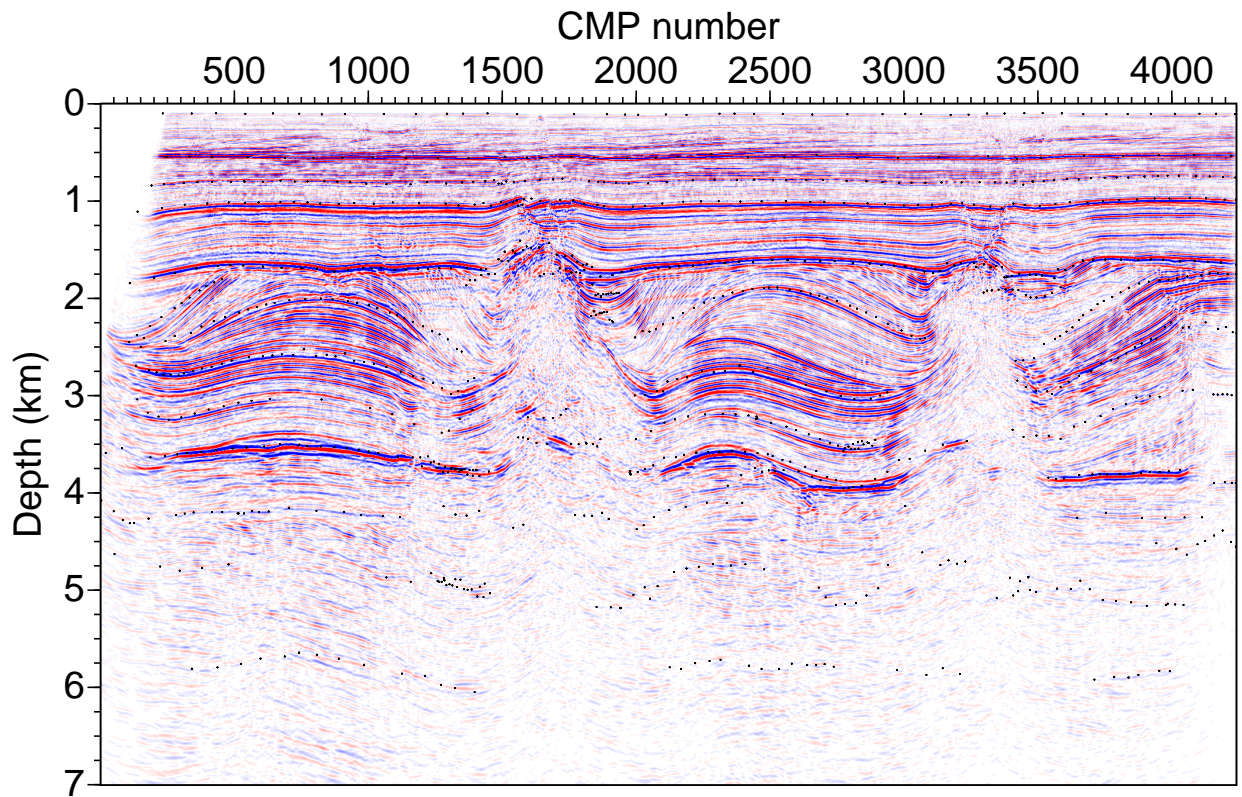


(b) PostSDM of the CRS stack with back-propagated picks

Figure 2.18: Marine data: poststack depth migration of the CRS stack with back-propagated picks. Migration corrected the images of the salt plugs and moved them towards their original position in space as compared to the time stacked sections (Figures 2.5 and 2.6). Diffractions present in the time-stacked sections are focused and the boundaries of the salt plugs can be better identified.



(a) PreSDM



(b) PreSDM with back-propagated picks

Figure 2.19: Marine data: Kirchhoff prestack depth migration with the back-propagated picks. The images of salt plugs, salt-sediments boundaries, and fault structures are greatly improved compared to the time-stacked sections. The corresponding common image gathers are shown in Figure 2.20.

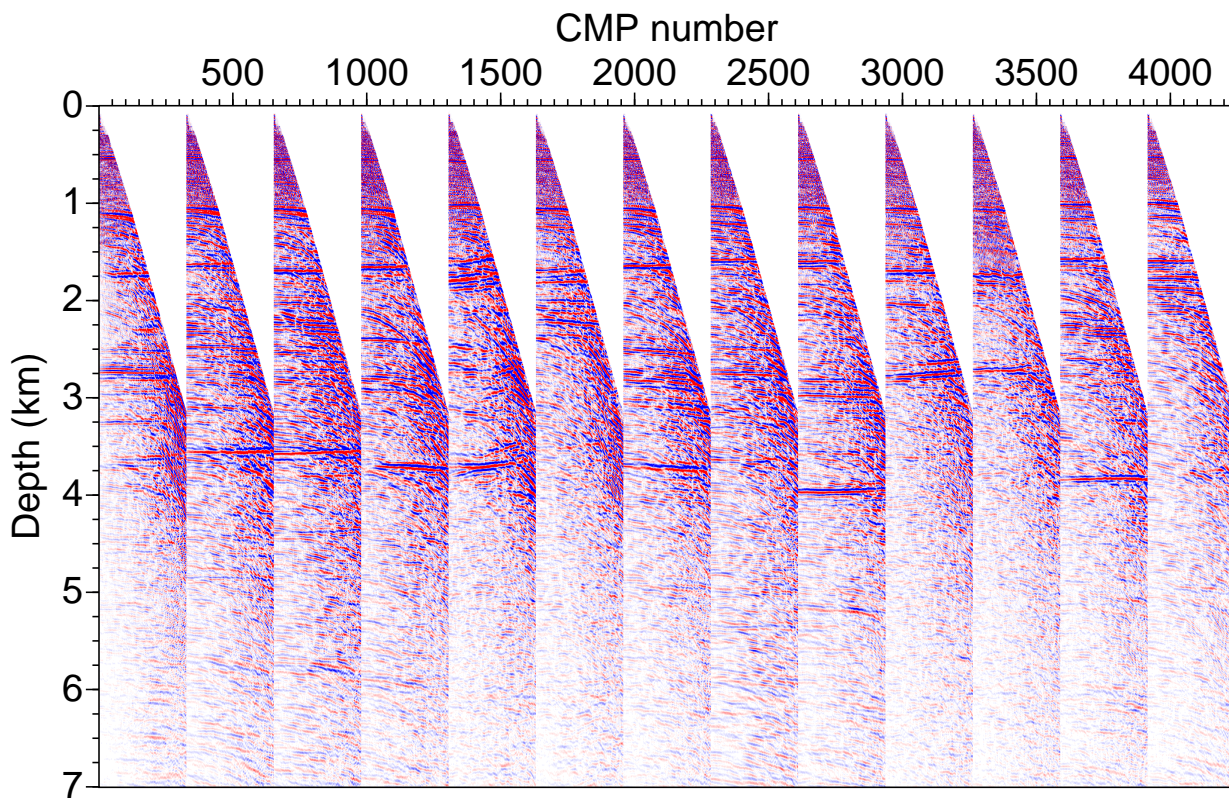


Figure 2.20: Marine data: common image gathers resulting from PreSDM with the NIP-wave tomographic model as presented in Figure 2.17. The images of most reflectors are almost horizontal, which confirms the consistency of the velocity model with the data.

Chapter 3

Land data example

This chapter shows the results of the application of the CRS technique to low-fold land data from Northern Germany. In 2002, the industry provided seismic reflection data to the scientific community and opened new opportunities to have a more detailed look on the salt stocks of the area. The data were acquired and processed in the 1980s. Compared to contemporary reflection acquisitions, the fold of these data is low (about 20). The processing in the 1980s provided basically stacking velocities and the CMP stacks. Velocity model building, time and depth migration were not applied to these data. Due to the structural complexity combined with the low fold severe imaging challenges were met.

The functional dependence of the individual Northern German salt structures on salt stock families was outlined by [Sannemann \(1968\)](#) and their history was described by [Jaritz \(1973\)](#). [Trusheim \(1957\)](#) introduced the term *halokinesis*. In the explanations of the formation of salt plugs and the development of salt plug families, these authors presumed density instabilities for the North German area between underlying light salt and overlying heavy sediments to be the major force of the buoyancy-driven halokinetic processes. This assumption was already theoretically investigated in the early past by [Hunsche \(1978\)](#) and, using analogue experiments, by [Heye \(1978\)](#). Nowadays, there are new concepts of salt tectonics, e.g., by [Mohr et al. \(2005\)](#) for NW Germany and by [Hudec and Jackson \(2007\)](#) for general concepts, based on complex multiphase salt tectonic evolution in changing regional stress field. Earlier, however, [Brink \(1984, 1986, 1987\)](#) and [Brink et al. \(1992\)](#) have reported several non-supporting observations for such concepts. Processing and interpretation of seismic reflection lines, gravity data, and density logs in boreholes raised severe doubts about the validity of the concept of [Mohr et al. \(2005\)](#), at least for the early stages (i.e. Lower Triassic, Bunter) of the halokinesis in Northern Germany. To address these doubts the structural settings of the study area were revisited. [Yoon et al. \(2008a,b\)](#) have re-processed these data using the CRS stack with the focus on time imaging of the lower crustal structures as well as the Moho-topography. [Baykulov et al. \(2009\)](#) have applied the CRS stack

and NIP-wave tomography and built a depth velocity model for a Jurassic salt plug located in the area of the Glückstadt Graben. This model allowed the application of prestack and poststack depth migration. The obtained depth images provided details not seen before, motivating an alternative view on the structural setting of the area.

The provided datasets were reprocessed within the priority programme SPP 1135 "Dynamics of Sedimentary Systems" (Bayer et al., 2008), sponsored by the German Research Foundation (DFG). The seismic reflection data were provided through the German Society for Petroleum and Coal Science and Technology (DGMK). The CRS stack technique is particularly suited for these low-fold data. The larger number of traces used by stacking leads to an improved S/N ratio, compared to the classical CMP processing. In this chapter, the results of the CRS processing and depth migration are shown on the example of a seismic profile from the area of the Glückstadt Graben.

3.1 Study area and acquisition geometry

The reprocessed profile is located north of the river Elbe. It almost coincides with the so called Elbe-Line, and crosses the Central Triassic Graben and its deepest part, i.e., the Glückstadt Graben, perpendicular to the graben axis (see Figure 3.1). Salt domes consisting of different kinds of salt from Rotliegend to Zechstein age cross the study area in NS direction.

The dataset consists of 771 shot gathers recorded to 13 s time. Explosive sources were used with an average shot spacing of 120 m. For every shot gather, 120 channels with a receiver group spacing of 40 m were used. Irregular shooting geometry led to a varying CMP fold with an average of 20. These and other important acquisition parameters are summarised in Table 3.1. This study, which focuses on the sedimentary structure and salt plugs, considers the time interval from 0 to 6 s TWT.

Line length	~93 km	Acquisition type	end-on
Total record time	13 s	Receivers per shot	120
Time sample rate	2 ms	Receiver group spacing	40 m
Number of shots	771	Source-receiver offset range	[40 m; 4800 m]
Source spacing	~120 m	Number of CMPs	4649
Source type	explosive	CMP spacing	20 m
Total charge size	3-5 x 5-20 kg	Maximum CMP fold	30
Shot depth	22-42 m	Mean CMP fold	20

Table 3.1: Land data: acquisition parameters.

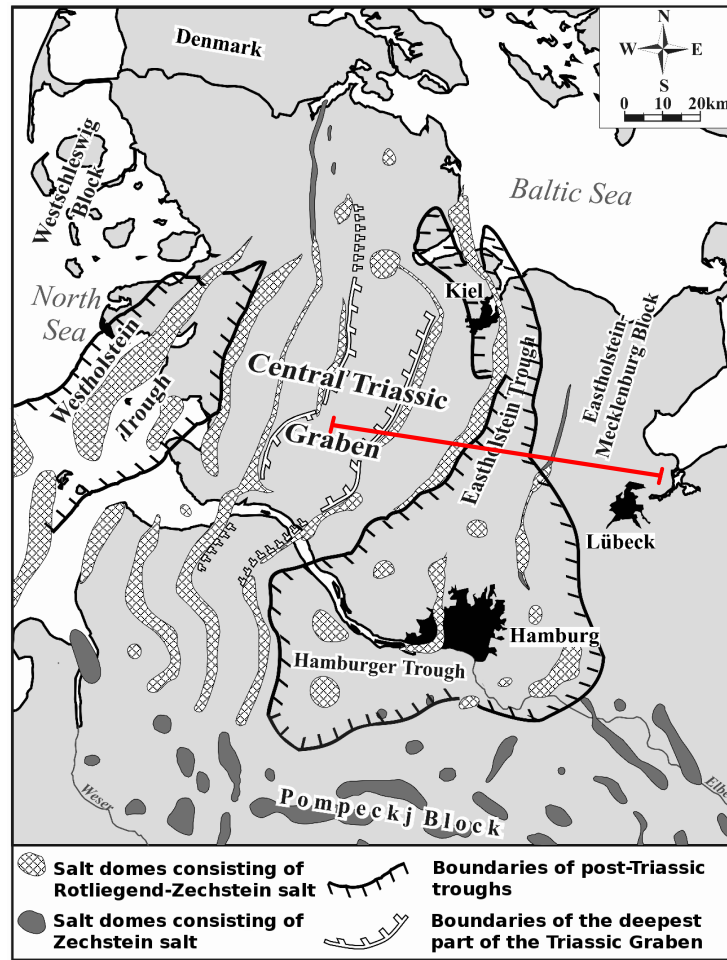


Figure 3.1: Land data: map of Northern Germany displaying major geological units as well as the distribution of salt plugs modified after [Maystrenko et al. \(2005\)](#). The deepest part of the Central Triassic Graben is also known as Glückstadt Graben. The reprocessed profile (red line) crosses the Glückstadt Graben and salt structures perpendicular to the graben axis. The total line length is about 93 km.

3.2 Preprocessing

I used the FOCUS software of Paradigm in order to enhance the quality and S/N ratio of the seismograms and to prepare the data for the CRS stack. The preprocessing sequence started with setting up the field geometry and applying the field static provided with the data. Then, manual trace editing was carried out, e.g. elimination of dead and noisy traces and high-frequency bursts in the shot gathers. After the trace editing, top muting was applied to remove the direct and refracted waves. Also bottom muting was used to eliminate the strong instrument noise present in some shot gathers at later times. The data were filtered using a bandpass filter of 5/18 to

45/50 Hz. These values represent sequentially the 0% and 100% points of the low-cut ramp, and the 100% and 0% points of the high-cut ramp. After resorting, 4649 CMP gathers were obtained. In order to enhance the amplitudes of reflection signals at deeper levels, an automatic gain control (AGC) was applied to the CMP gathers. The time window of the AGC was 1000 ms. A typical example of the preprocessed CMP gathers is shown in Figure 3.2. About 20 traces are located irregularly over the full offset range, which, accompanied by the low S/N ratio, leads to difficulties in identifying reflections.

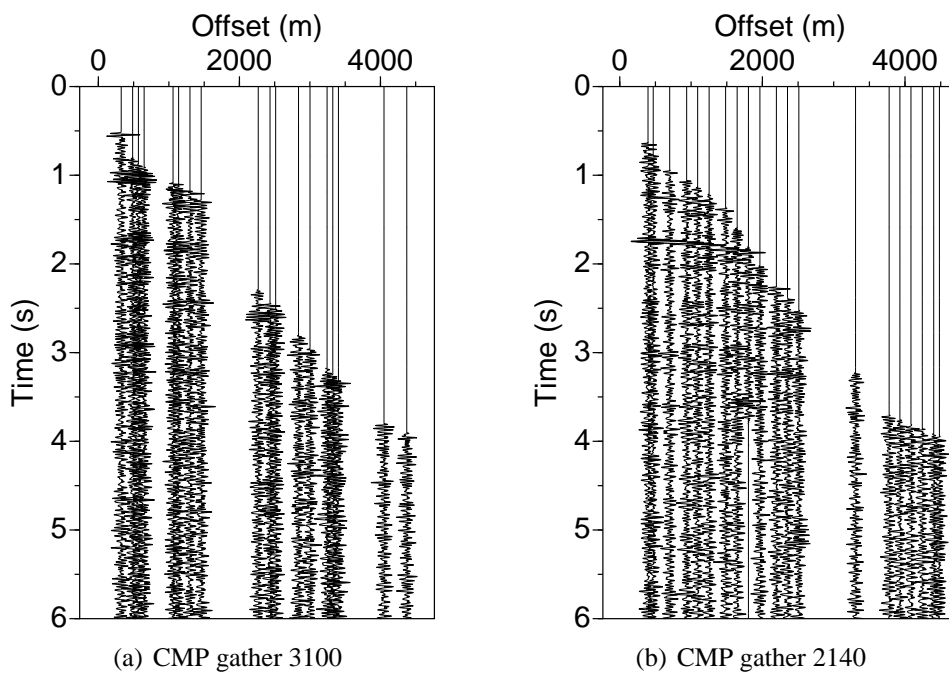
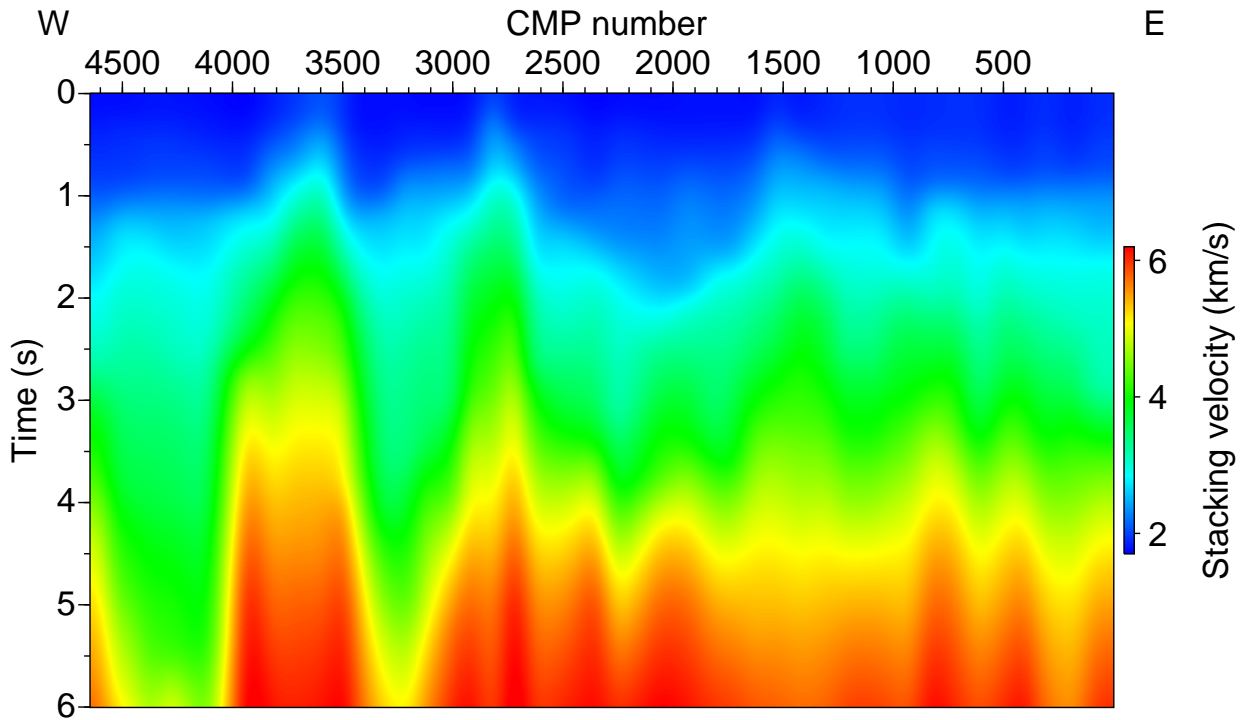
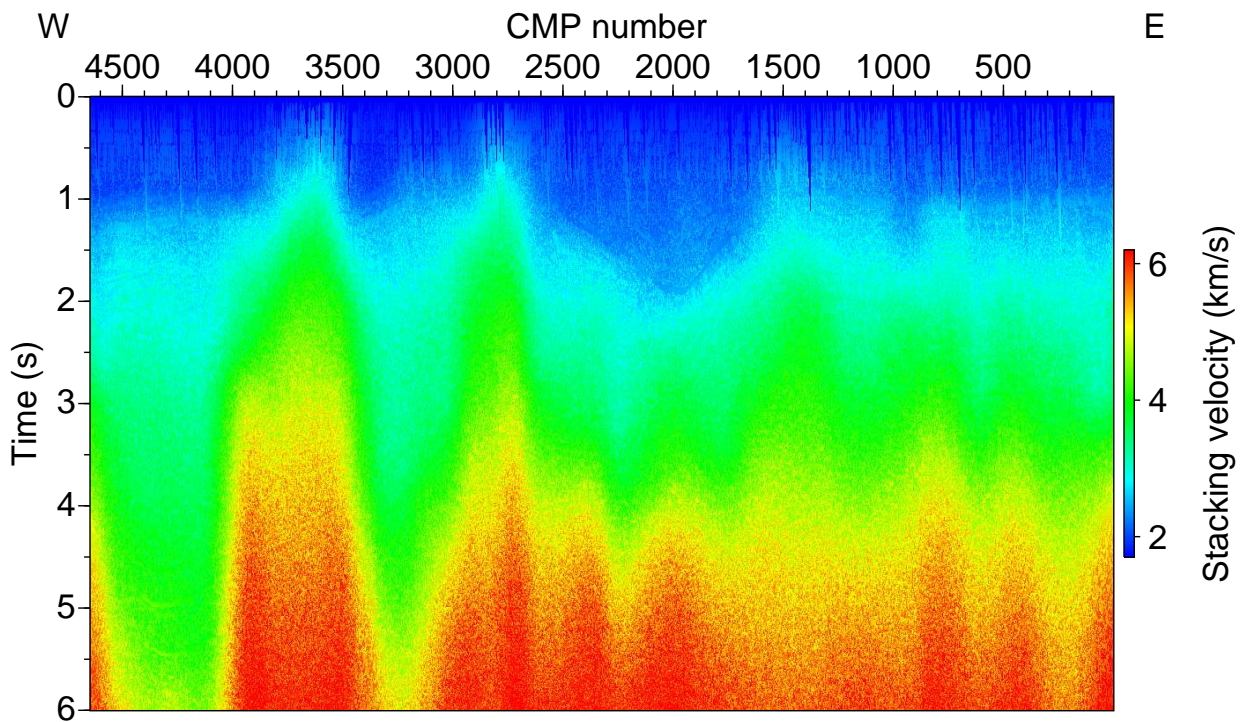


Figure 3.2: Land data: exemplarily chosen CMP gathers after preprocessing. The CMPs contain irregularly-spaced traces. Reflections are hardly visible; the S/N ratio is low.

Tables of stacking velocities for certain CMP positions (approximately every 100th CMP) were provided with the dataset. The velocities between the provided points were interpolated and smoothed to obtain a velocity model in the same way as for the marine data (in Chapter 2). The resulting model (Figure 3.3(a)) represents the stacking velocities for every point in the ZO domain. Strong lateral and vertical velocity variations are visible throughout the section. Starting from ~ 1.8 km/s at the surface, the velocity increases up to 5–6 km/s at 6 s TWT. The areas of the salt plugs between CMP 3500–4000 and 2700–3000 are characterised by increased velocities compared to the surrounding sediments.



(a) Model of stacking velocities provided by the industry



(b) Model of stacking velocities obtained after the automatic CMP stack

Figure 3.3: Land data: model of stacking velocities (a) provided by the industry and (b) obtained after the automatic CMP stack. The velocities provided by the industry were used as guide functions for the stacking velocity search, where 10% maximum deviation was allowed. The complexity of the interfaces with the presence of salt plugs and steep-dipping layers leads to strong lateral variations in the models.

Surface velocity	1750 m/s
Maximum deviation from reference velocity model	10%
Maximum dip angle	60°
Minimum offset aperture	40 m at 0 s
Maximum offset aperture	4800 m at 5 s
Minimum midpoint aperture	400 m at 0 s
Maximum midpoint aperture	2000 m at 5 s

Table 3.2: Land data: processing parameters for the automatic CRS stack.

3.3 CRS processing

The automatic search for CRS parameters was applied to the preprocessed CMP gathers. I used the same approach as for the marine data, which is based on three one-parameter search processes. In order to image near surface structures as well as deeper structures properly, different offset and midpoint apertures were tested. After a number of experiments, the offset aperture was defined between 40 m for near-surface times to 4800 m, i.e., full acquisition aperture, at 5 s TWT. The interpolation of the aperture in between is linear, whereas for later times the constant aperture of 4800 m was used. The midpoint aperture was defined from 400 m at the near-surface to 2000 m at 5 s TWT (see Table 3.2).

3.3.1 Automatic CMP stack

The stacking velocities provided by the industry were used as a guide during the stacking velocity search. The maximum deviation from the guide values was set to 10%. The resulting model is shown in Figure 3.3(b). Since the best fit value of velocity for every time sample is estimated during the search, the model appears less smooth than the guide model, but cares for the better stacking results.

The obtained velocities were used to generate the CMP stack section (Figure 3.4). The section provides a detailed image of the sedimentary part down to 3–4 s TWT. Salt plug areas with high velocities are visible around CMP 1500, 2500–3000 and 3500–4000. At CMP 1500, a steep fault is visible, which separates the East-Holstein Trough in the west from the Eastholstein-Mecklenburg block in the east (Maystrenko et al., 2005). Also, sharp parallel dipping reflections are observed in the upper crust between 4.5 and 5.5 s at TWT CMP 4000–4500 that can be correlated with two parallel dipping reflections between 3 to 4 s TWT at CMP 3000–3500. These reflections coincide with a high conductivity body observed in magnetotelluric data by

Hoffmann et al. (2005). In the deeper part of the section reflections are hardly visible due to energy loss in the salt and low S/N ratio.

3.3.2 Automatic CRS stack

After the CMP stack section was obtained, the automatic CRS parameter searches were carried out and the CRS stack section was generated. Figure 3.5 shows the result of the automatic CRS stack. Compared to the CMP stack, the CRS stack significantly increased the S/N ratio and generally improved the image quality of the section. The sedimentary cover and internal salt structures appear clearer and more detailed than in the CMP stack section. The CRS stack shows apparently different reflectivity patterns in the eastern part than in the western part of the profile. The section reveals a comparably highly reflective upper crust within a 3 to 4 s wide band in the eastern part. This might indicate that this area was tectonically less active than the area in the western part of the profile, where less reflectivity is observed.

Figure 3.6 shows enlarged images of the CMP and CRS stacked sections of the salt plug located in the middle part of the profile. Beside the general improvement of image quality, the CRS stack shows some details that are hardly visible in the CMP stack section. Internal salt reflections between CMP 2500 and 2800 at 1.5–2 s and at 2.5 s TWT are clearly identified. The salt-sediment boundaries are better imaged by the CRS stack, which is important for the interpretation of the data and for building of the geological model of the area.

Besides the ZO-stacked section, the CRS stack provided the sections of CRS parameters. Figure 3.7 shows the CRS semblance section. The salt-rich areas are characterised by low values of semblance due to the dispersal of reflection energy in the salt. The sedimentary boundaries have semblance values of up to 0.4. Because of energy loss and increasing noise the middle and the eastern parts of the section below 4 s TWT show only few coherent events. In the western part between CMP 4000 and 4500 from 3.5 to 5.5 s TWT a number of reflection events are visible that are also seen in the CMP and CRS stack sections.

Figure 3.8 shows the angle of emergence, α , clipped to $\pm 10^\circ$. These clip values emphasise the small angles in different parts of the section. Low values characterise the sediment cover in the eastern part of the section between CMP 0 and 1500 and in the western part between CMP 4000 and 4500. Inbetween, at the salt-sediments boundaries, the angle increases up to 10 degrees and more. The maximum absolute values of emergence angle are observed at the diffraction events around CMP 1500 and in intra-salt areas between CMP 2500–3000 and 3500–4000.

Figure 3.9 shows the radius of curvature of the NIP-wave, R_{NIP} . It increases smoothly with increasing recording time and reaches the values of 30 km at 6 s TWT. The complexity of the in-

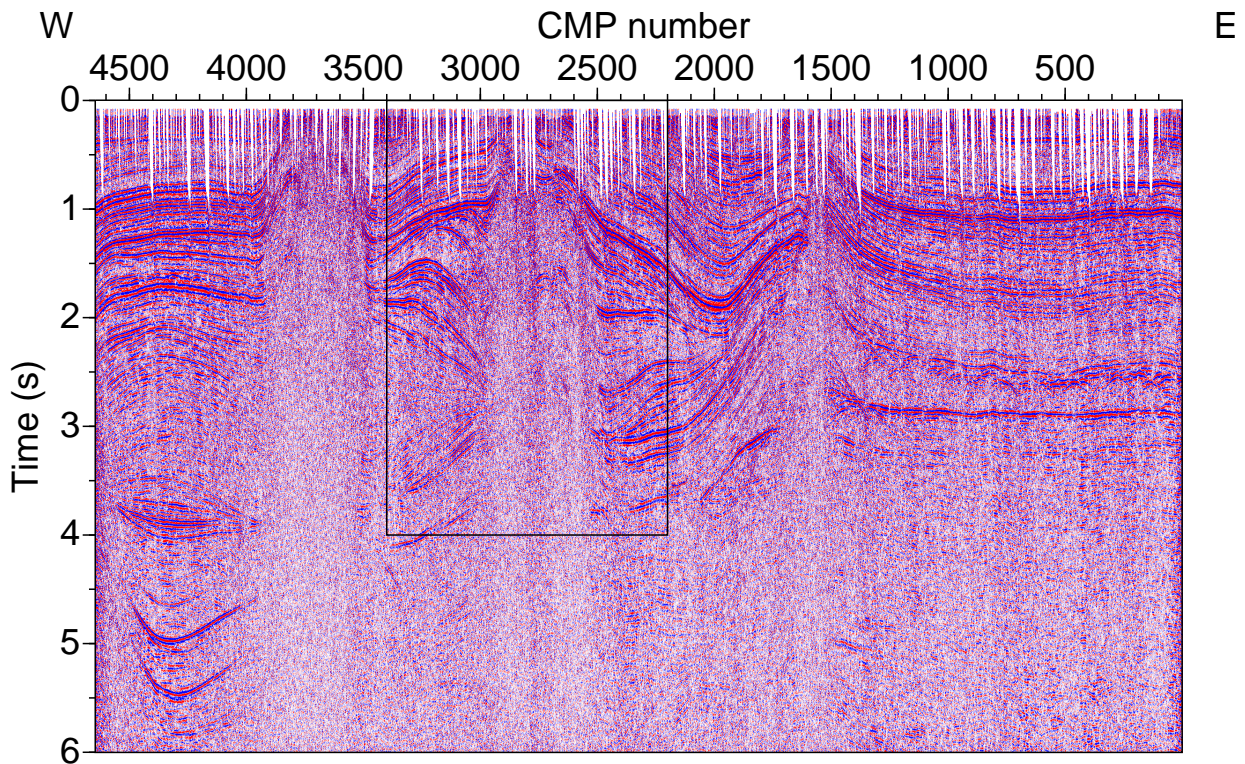


Figure 3.4: Land data: automatic CMP stack. The upper part (0–4 s TWT) of the sedimentary cover is well imaged, whereas the deeper structures are hardly visible. The S/N ratio is low. Irregular acquisition geometry leads to the data gaps in the shallow part of the section above 1 s TWT. Salt plugs are present around CMP 1500, between CMP 2500–3000 and 3500–4000. The area of the middle salt plug indicated by the rectangle is enlarged in Figure 3.6(a).

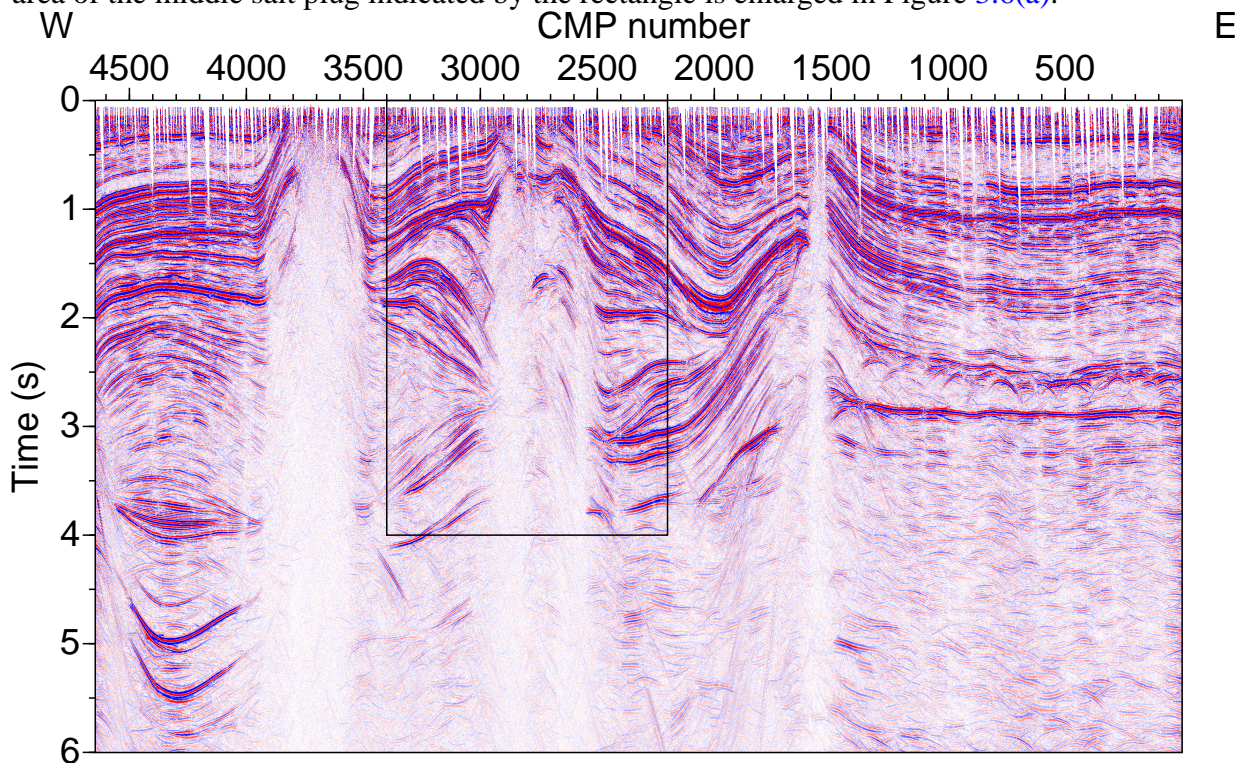


Figure 3.5: Land data: automatic CRS stack. The image shows pronounced reflections at all time levels. The S/N ratio is increased and the reflections appear more continuous compared to the CMP stack section (Figure 3.4). Diffraction events are also enhanced. The rectangle is enlarged in Figure 3.6(b).

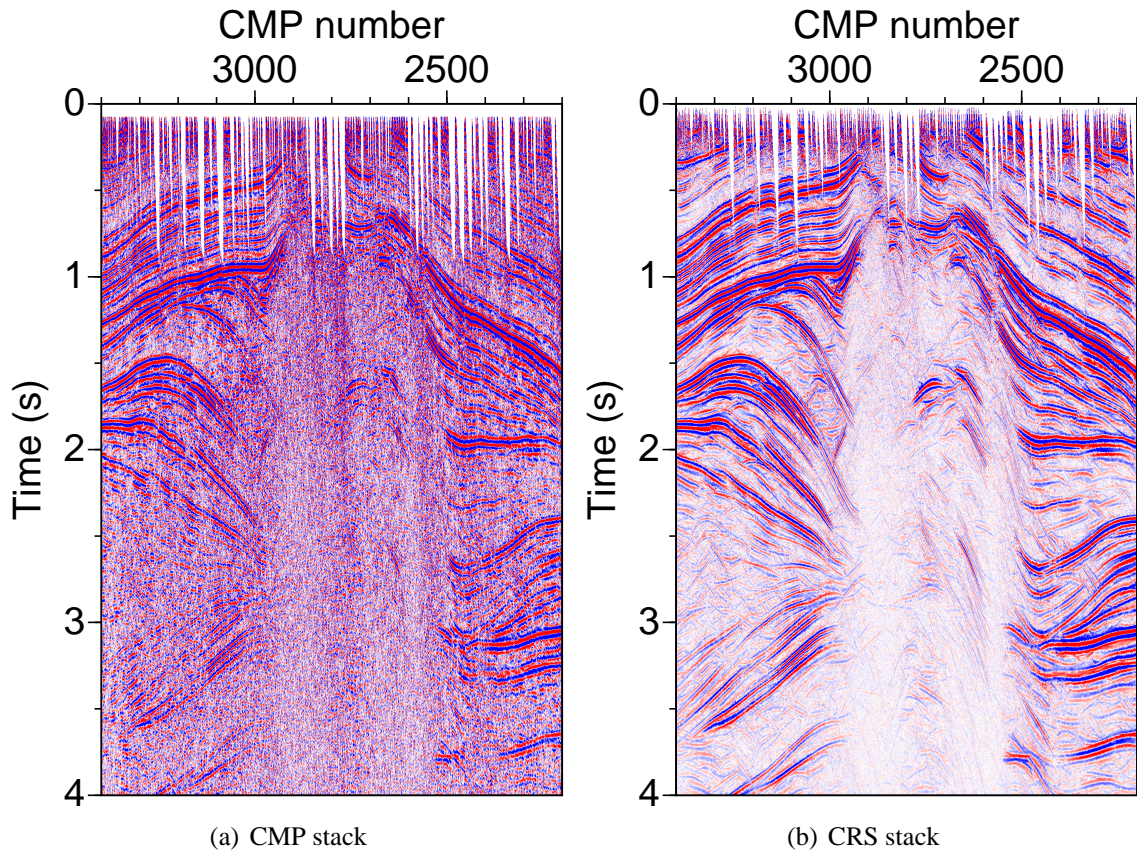


Figure 3.6: Land data: comparison of the CMP stack (a) and CRS stack (b) shows that the CRS stack significantly enhanced the internal salt reflections. Due to higher S/N ratio the reflections at deeper levels are better imaged in the CRS stack section, and the salt-sediment boundaries are easier identified.

interfaces with steeply-dipping salt-sediment boundaries accompanied by many diffraction events leads to values of R_{NIP} significantly larger than the expected depth of the corresponding sediments. NIP-wave tomographic inversion is, therefore, recommended to estimate the correct reflector depth.

Figure 3.10 depicts the radius of curvature of the N-wave, R_N . The section is shown using clip values from -20 to 20 km in order to emphasise the changes of this parameter at the flanks of the salt plugs. Inside the salt and in the upper part of the section, as well as in the areas of low S/N ratio, low values of R_N are observed. The eastern part of the section is characterised by comparably higher values than the western part, since almost flat reflections are present there.

The number of traces used by the automatic CRS stack to generate one ZO time sample is much higher than used by the CMP stack (compare Figures 3.11 a and b). Whereas the number of traces used by the automatic CMP stack is limited by the CMP fold of the data (about 20), the

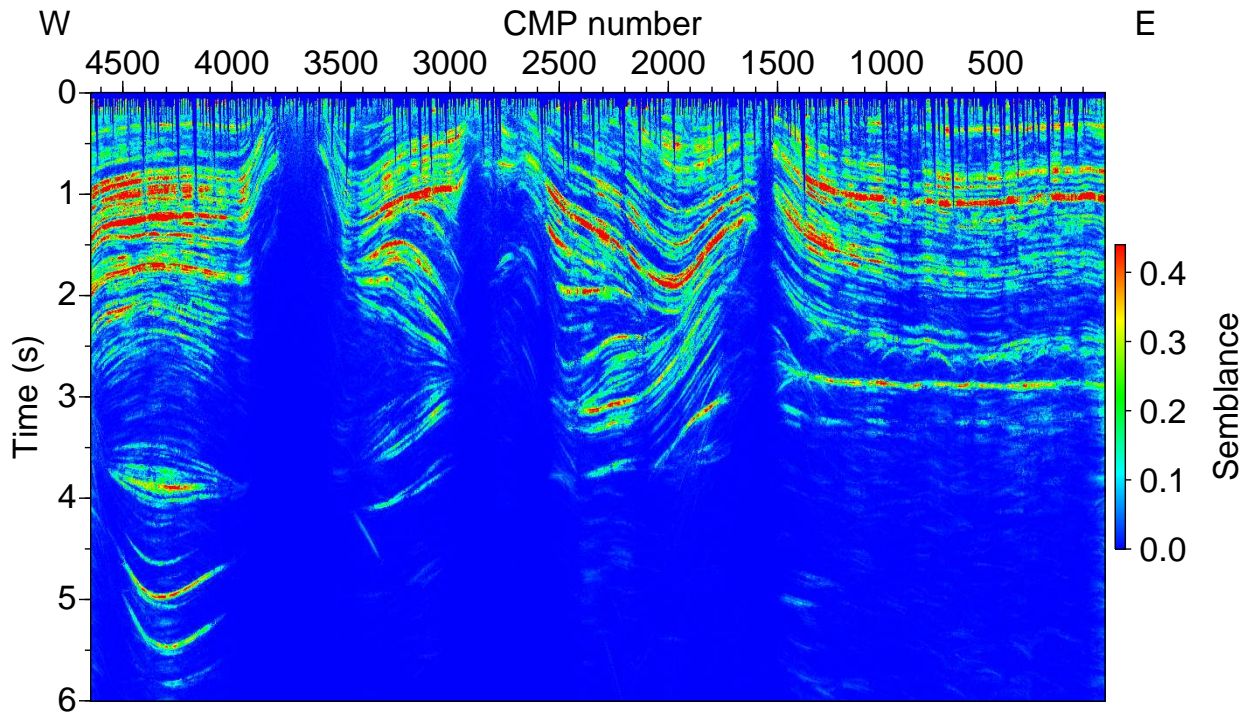
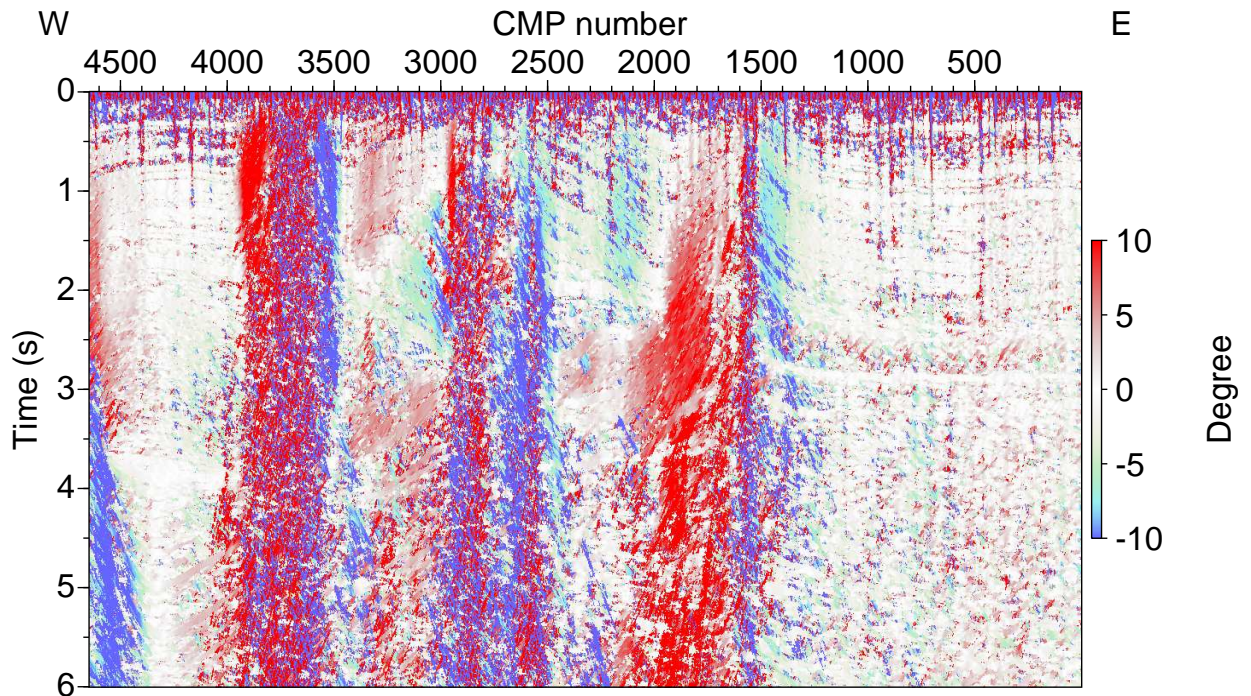
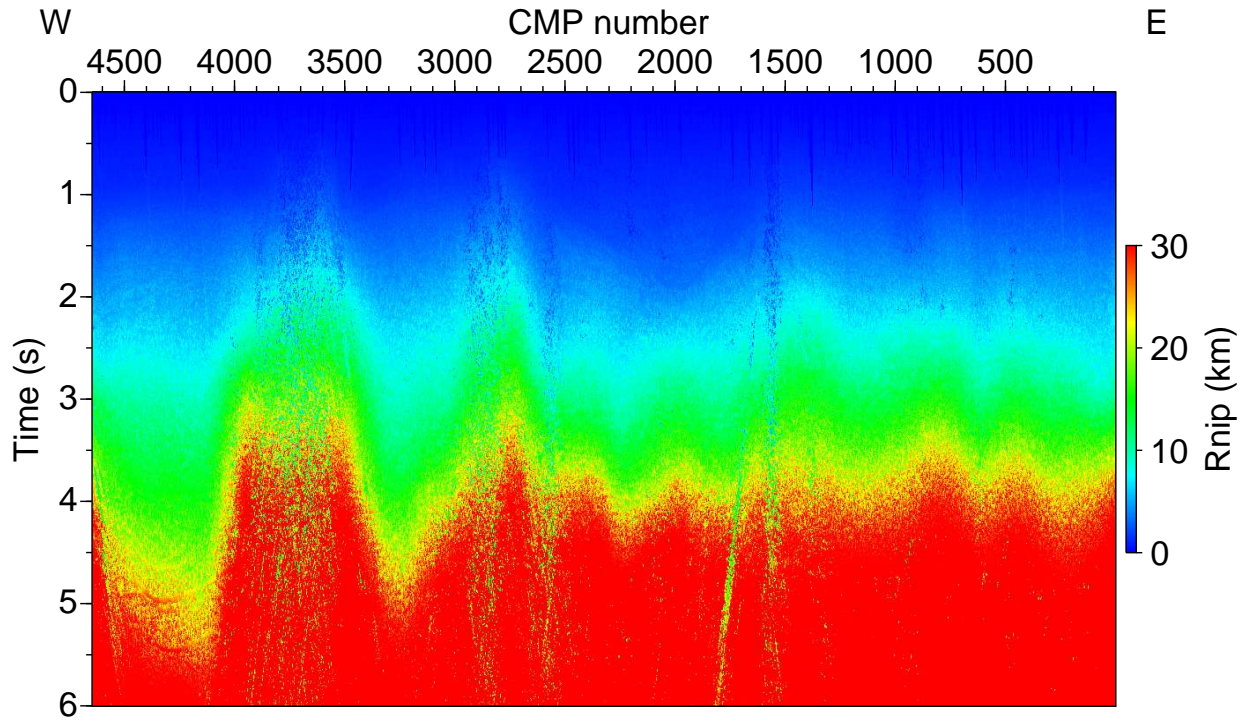
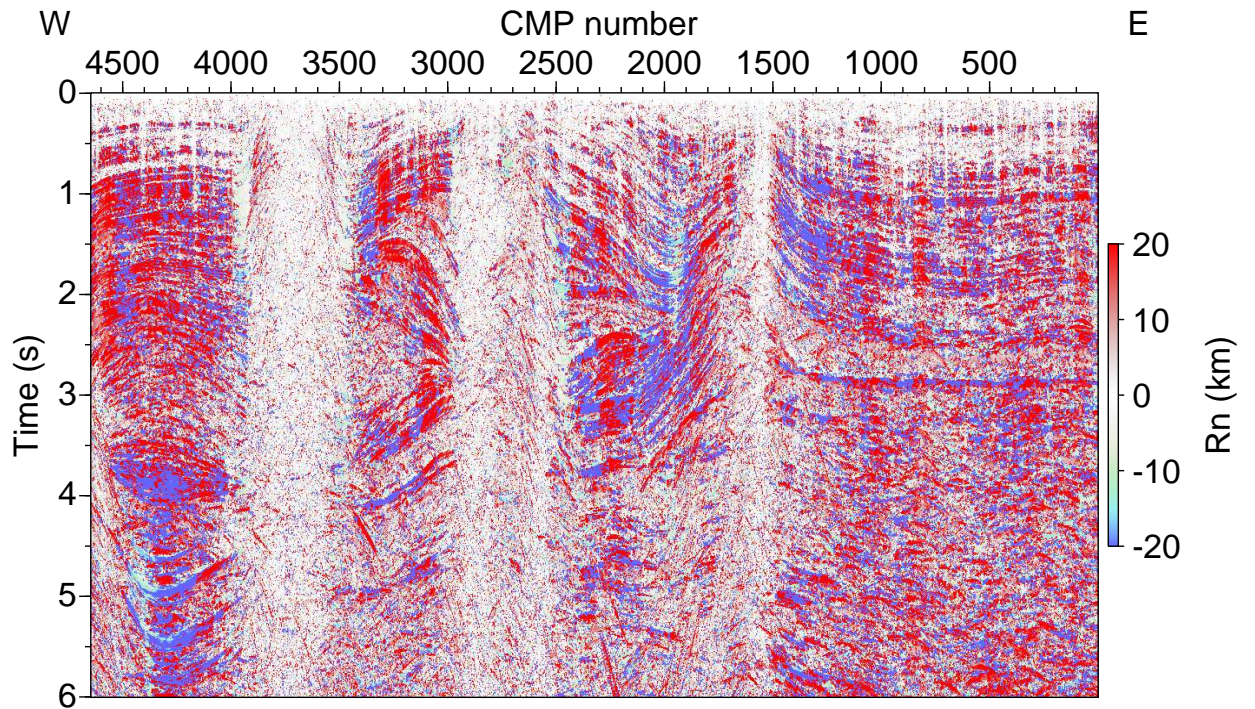


Figure 3.7: Land data: CRS semblance section.

Figure 3.8: Land data: angle of emergence, α .

Figure 3.9: Land data: radius of curvature of the NIP-wave, R_{NIP} .Figure 3.10: Land data: radius of curvature of the N-wave, R_N .

CRS technique uses up to 2000 traces for stacking.

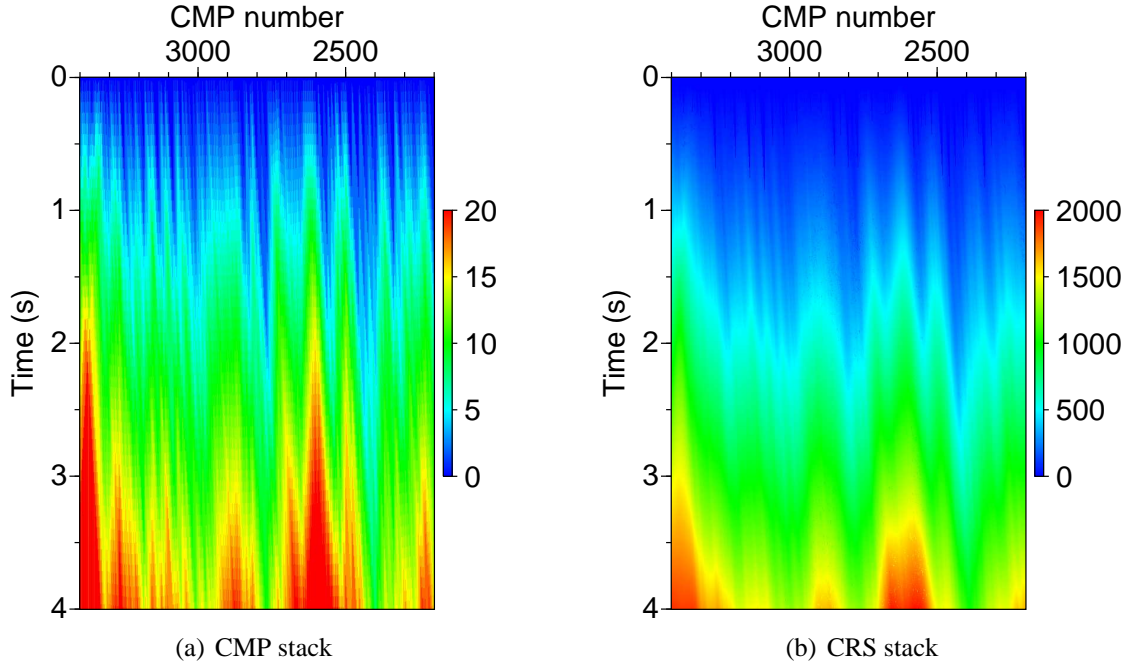


Figure 3.11: Land data: number of traces used by automatic CMP and CRS stacks to generate one ZO time sample. Note the different scales. Using about 100 times more traces during the CRS stack increases the S/N ratio of the stacked section and generates images of higher quality.

3.3.3 NIP-wave tomographic inversion

All required information for the tomographic inversion is contained in the CRS parameters obtained during the automatic CRS stack. In order to acquire the input data for NIP-wave tomography, a number of ZO points describing the primary events were picked (see Figure 3.12). The automatic picking software procedure provided the input data for inversion. The CRS semblance section presented in Figure 3.7 is used as a guidance for the coherency of the picks. After the picking of most coherent events, the wavefield attributes were extracted from the corresponding CRS parameter sections. Unlike the marine data, where the ZO points were picked per hand, the complex salt structures and lower quality of the time sections complicate the manual picking in these land data. Moreover, more picks are necessary to describe the complex reflection shape of the section.

The quality of the extracted CRS parameters was controlled with the plots of the parameter M_{NIP} and stacking velocities as a function of travelttime. First, the values deviating significantly from the main trend of stacking velocities were eliminated with the help of the plot presented in Figure 3.13(b). Then, the quality of picks was checked with respect to the corresponding M_{NIP} values

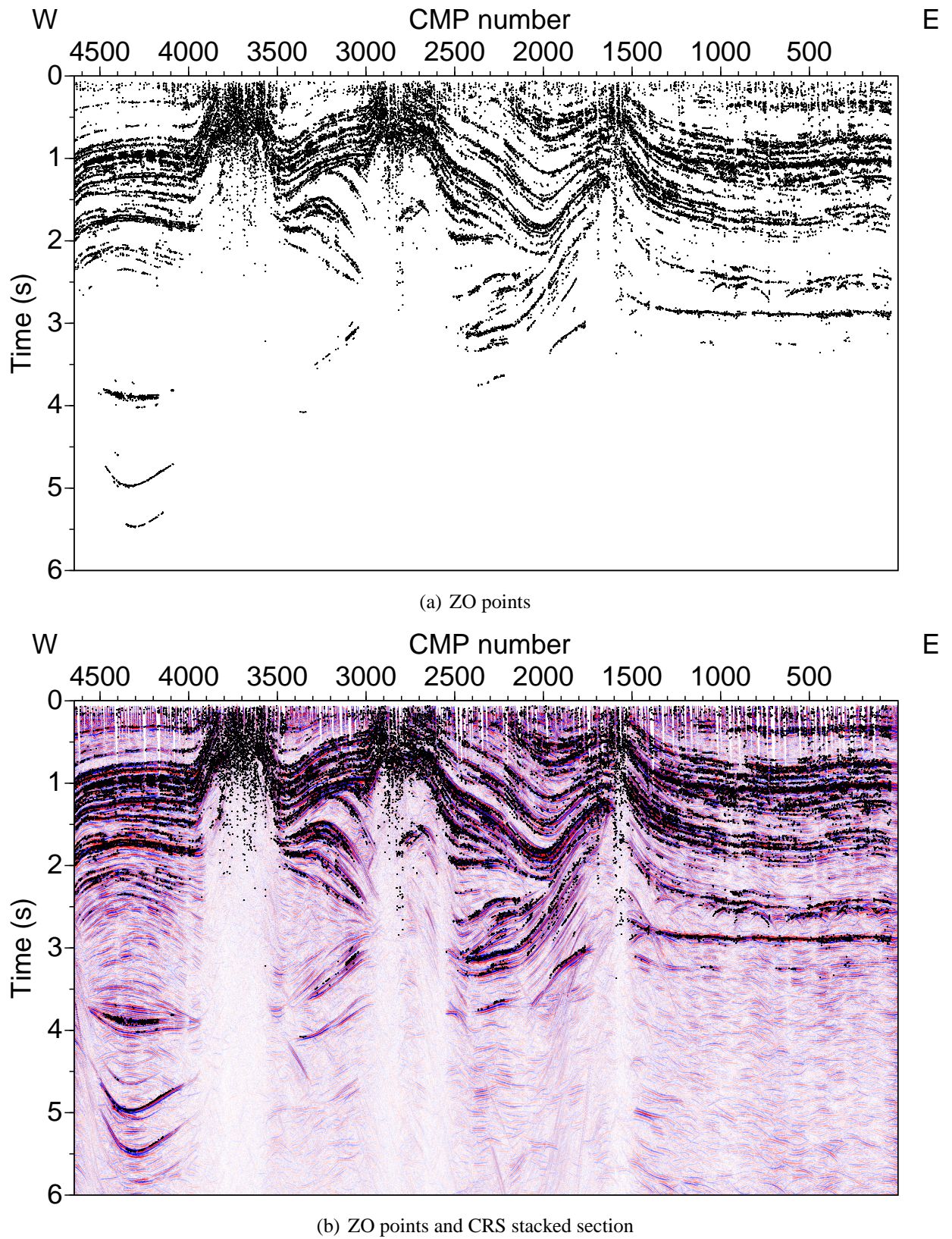


Figure 3.12: Land data. (a) Input picks (black dots) for the NIP-wave tomography obtained using the automatic picking based on semblance threshold. (b) The distribution of the picks coincides with the main geological structures of the CRS stacked section. Because of the low coherence the internal parts of the salt plugs contain less picks than the surrounding sediments.

(Figure 3.13(a)). The points are aligned along the main trend, without outliers. Finally, about 35000 picks along the entire profile remained for the inversion. The distribution of the picks is in good correlation with the main structures present in the CRS stack section (see combined plot in Figure 3.12(b)). Strong seismic impedance contrasts at the main seismic boundaries provide high coherency values and, therefore, reliable results of the automatic picking down to base Rotliegend. Also, the salt flanks and internal reflections in the salt body in the central part of the section (CMP 2600–2800, 1.5–2 s TWT) were picked.

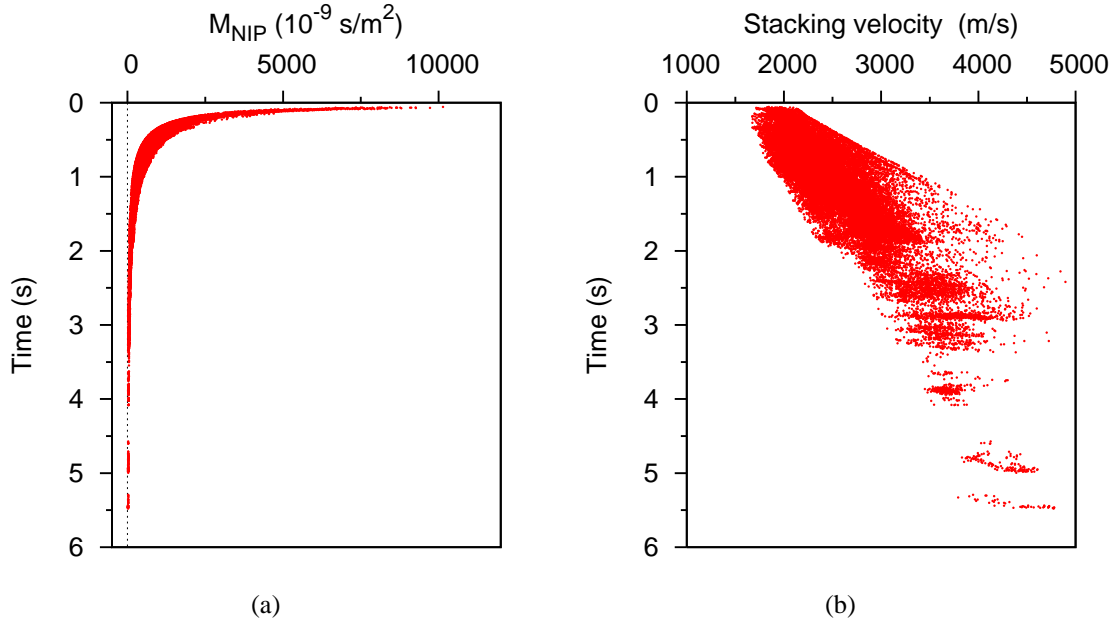


Figure 3.13: Land data: quality control of input picks for NIP-wave tomography after the removal of outliers. The parameter M_{NIP} (a) and stacking velocities (b) are computed for each ZO point from the corresponding CRS parameters.

The NIP-wave tomography model was determined on a grid consisting of 93 nodes in lateral and 41 nodes in vertical direction. The lateral grid spacing was 1000 m, the vertical grid spacing was 200 m. As an initial model a near-surface velocity of 1750 m/s with a constant velocity gradient of 0.5 s^{-1} was used. A priori velocity information from the well logs was not included to constrain the tomography. With these parameters, the inversion converged after a total of five iterations. Figure 3.14 shows the results of the NIP-wave tomography as a progress from initial gradient to the final model. The cost function S is outlined in Figure 3.15. It decreases with increasing iteration number, and after the fifth iteration remained unchanged. The sixth iteration did not decrease the regularisation function, and no changes in the velocity model were made. Therefore, the model obtained after the fifth iteration was considered the final result of tomographic inversion.

For depth migration, the obtained velocities were extrapolated constantly to 12 km depth. The resulting velocity section with corresponding back-propagated picks is outlined in Figure 3.16.

Lateral grid spacing	1000 m
Depth grid spacing	200 m
Number of nodes in lateral direction	93
Number of nodes in depth direction	41
Initial model:	
surface velocity	1750 m/s
gradient	0.5 s^{-1}
Number of tomographic iterations	6

Table 3.3: Land data: parameters of the NIP-wave tomographic inversion.

Velocities from 1.8 to 4.6 km/s are shown in order to emphasise the salt structures in the upper part of the model. The values of velocities and corresponding back-propagated picks are consistent with the input data. In the upper part of the model velocities vary between 1.8 and 3.5 km/s, which is typical for Tertiary sediments. At 3 km depth, two local velocity maxima reaching 4.5 km/s are present at CMP 2500–3000 and 3500–4000. These maxima correspond to the salt plugs visible in the time stacked sections. A high velocity area in the western part of the section between CMP 0 and 2000 at 2–4 km depth might indicate the presence of salt-rich sediments. Areas with only a few picks display minor deviations from the initial velocity model, e.g., in the region between CMP 3000–4500, 3–5 km depth, as well as in the deeper part of the section below 6 km depth.

3.4 Depth migration

Figure 3.16 shows the NIP-wave tomography model that was used for the depth migration of the dataset. The ProMAX software provided a poststack depth migration of the CRS stack section, as well as a prestack depth migration of the preprocessed CMP gathers. The CMP spacing of the depth migrated sections was defined to 20 m, the same as for the time stacked sections. The seismograms were migrated to maximum frequencies of 50 Hz and 12 km depth with a depth sampling interval of 10 m. Maximum amplitude ray tracing was used to produce the Green's functions. The maximum emergence angle was 70° . The migration aperture was set to 2400 m, which provided a compromise solution to obtain few migration artefacts and better continuity of reflector elements. The depth migration parameters are summarised in Table 3.4.

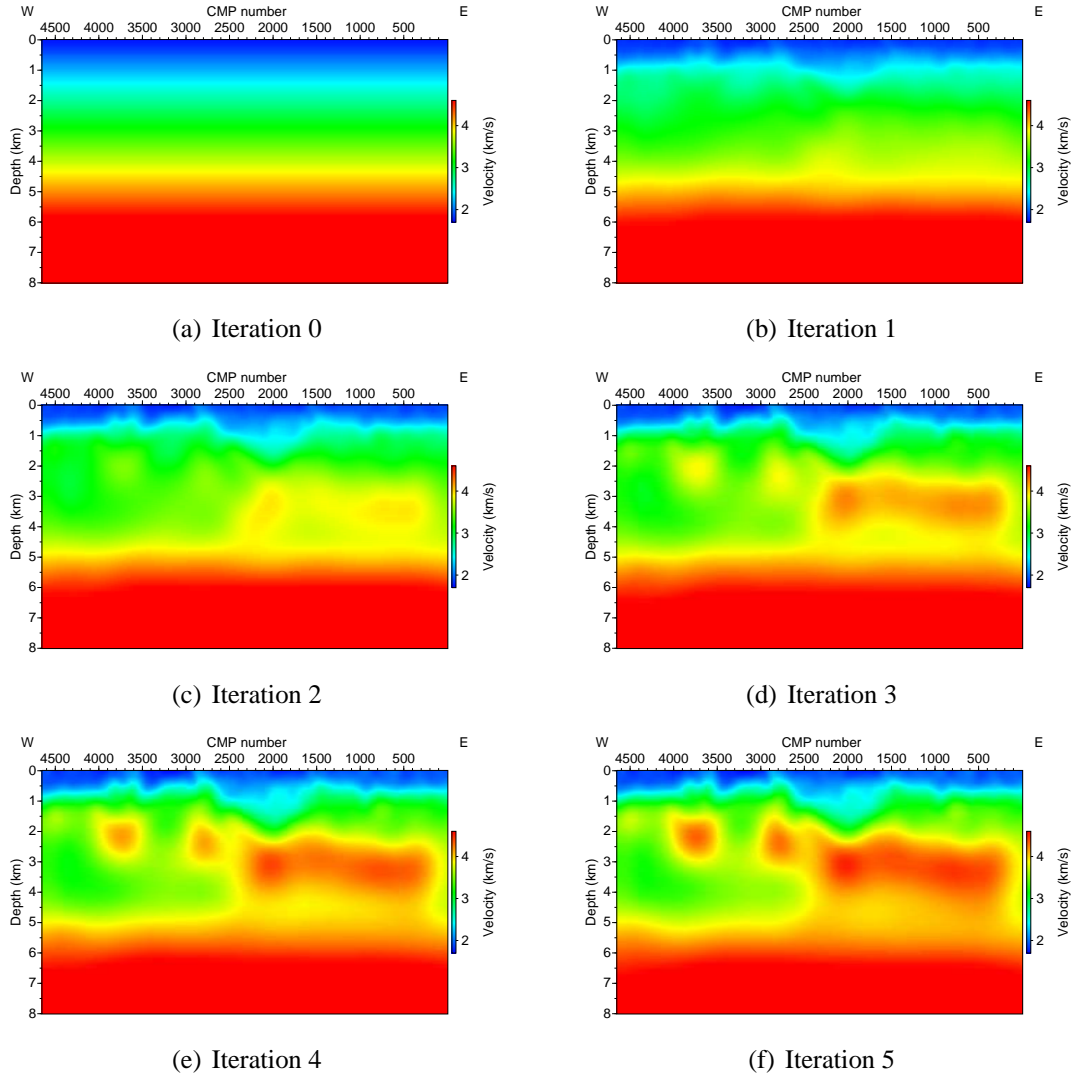


Figure 3.14: Land data: depth velocity models with corresponding back-propagated picks computed after every tomographic iteration. Starting from the initial gradient (a), the model is continuously updated, and the salt-rich structures become recognisable. The final model obtained after five iterations (f) is enlarged in Figure 3.16.

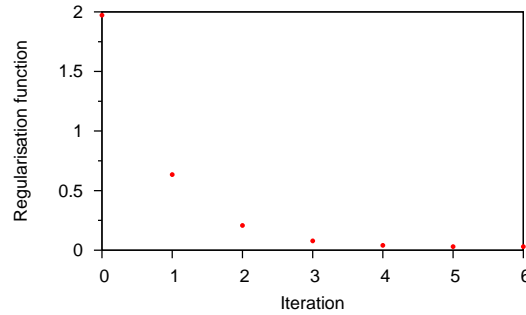
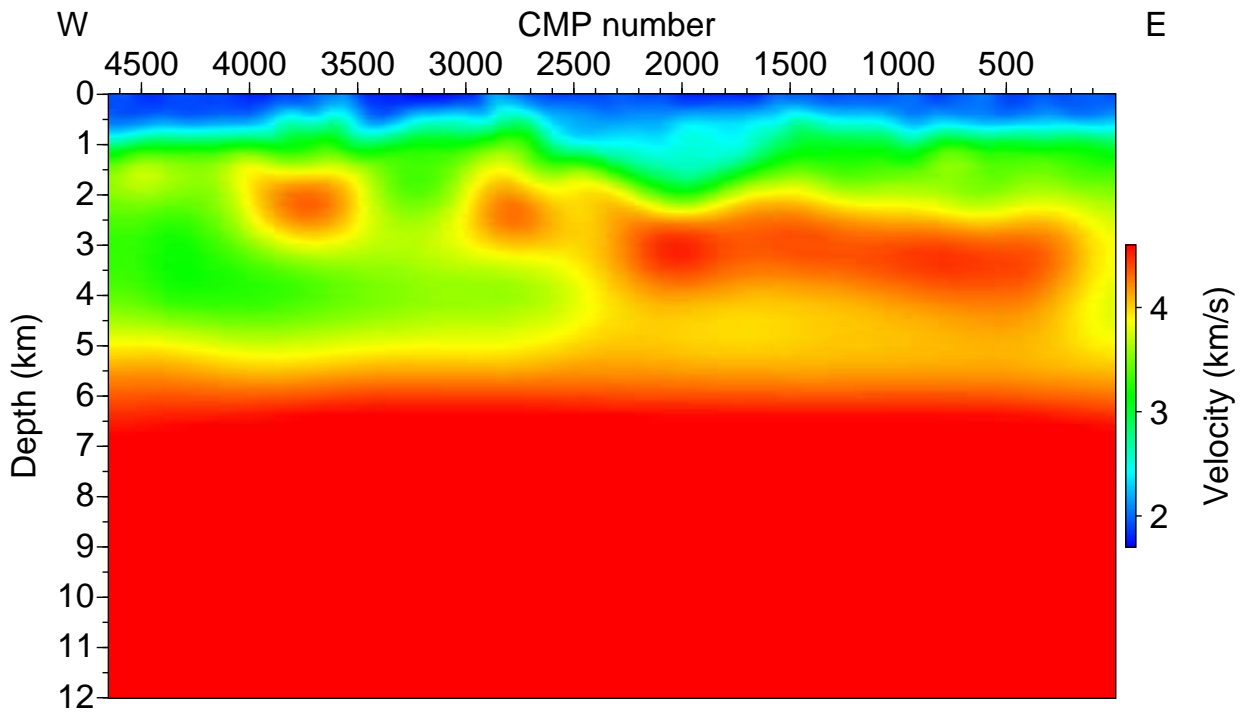
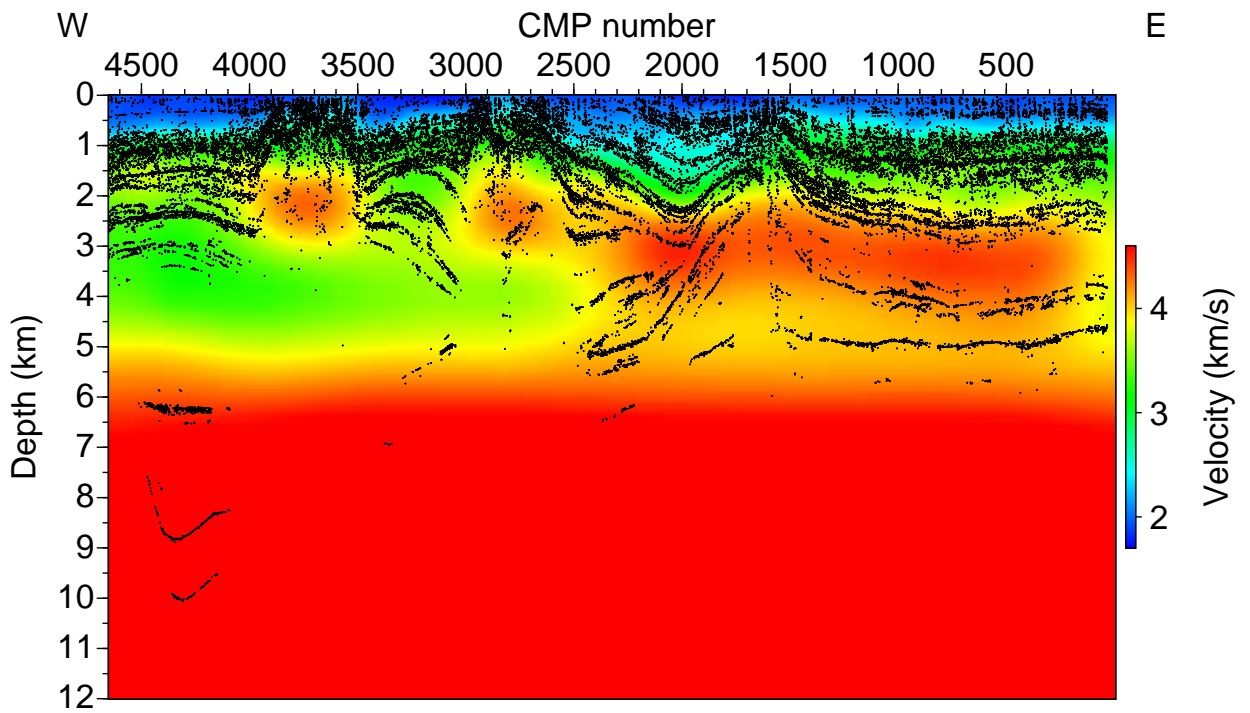


Figure 3.15: Land data: value of the cost function S computed after every tomographic iteration. The function decreases with increasing iteration number, and after the fifth iteration remained unchanged. The depth velocity model obtained after the fifth iteration was, therefore, considered as the final model.



(a) Depth velocity model



(b) Depth velocity model with back-propagated picks

Figure 3.16: Land data: reconstructed smooth velocity model with back-propagated picks obtained after five NIP-wave tomographic iterations. The velocities were extrapolated linearly from 8 to 12 km depth. Velocity maxima in the upper part of the section (1.5–4 km depth) correspond to the salt plugs and salt-rich areas. The model is used for depth migration of the data.

CDP spacing in output field	20 m
Maximum frequency	50 Hz
Depth sampling interval	10 m
Maximum depth to migrate	12000 m
Migration aperture	2400 m
Maximum emergence angle to trace rays	70°
Velocity model sample interval	100 m
Method for generating the Green's function	Maximum amplitude ray tracing

Table 3.4: Land data: processing parameters for depth migration.

3.4.1 Poststack depth migration of the CRS stack

Poststack depth migration was applied to the CRS stacked section. Figure 3.17 shows the resulting depth image down to 12 km. The PostSDM generated a depth section with high S/N ratio, comparable with the result of the CRS stack. Reflectors are clearly visible from 0 to 7 km depth throughout the entire image. In the western part of the section, two deep events are displayed at 8–10 km depth at CMP 4000–4500. The boundaries of the salt plugs appear at their corrected lateral position and diffractions are focused as compared to the time stacked sections. At ~9 km depth the images of reflector elements of the pre-Permian age are visible between CMP 2000–2500 and 3000–3500. These reflectors were not identified before.

The interior of the salt plug located in the middle part of the section is enlarged in Figure 3.19(a). The top of salt at about 1 km depth is clearly visible. The image shows a set of unique internal reflectors between CMP 2600 and 2900 at 2–5 km depth that can be associated with different kinds of salt of unknown age from Rotliegend to Keuper (see stratigraphic chart in Figure 2.2). All horizons down to base Rotliegend at 6.5–7 km depth are clearly visible.

PostSDM of the CRS stack can be used as complementary material to PreSDM for the interpretation of the salt-rich areas of Northern Germany. The depth image of the entire section reveals new details not identified before after conventional CMP processing, indicating an alternative geological interpretation of the salt structure and the underlying pre-Permian. The latter helps to evaluate the hydrocarbon systems in this area. This includes the structural setting as well as the distribution of source rocks, and possible migration pathways, which is discussed by Baykulov et al. (2009).

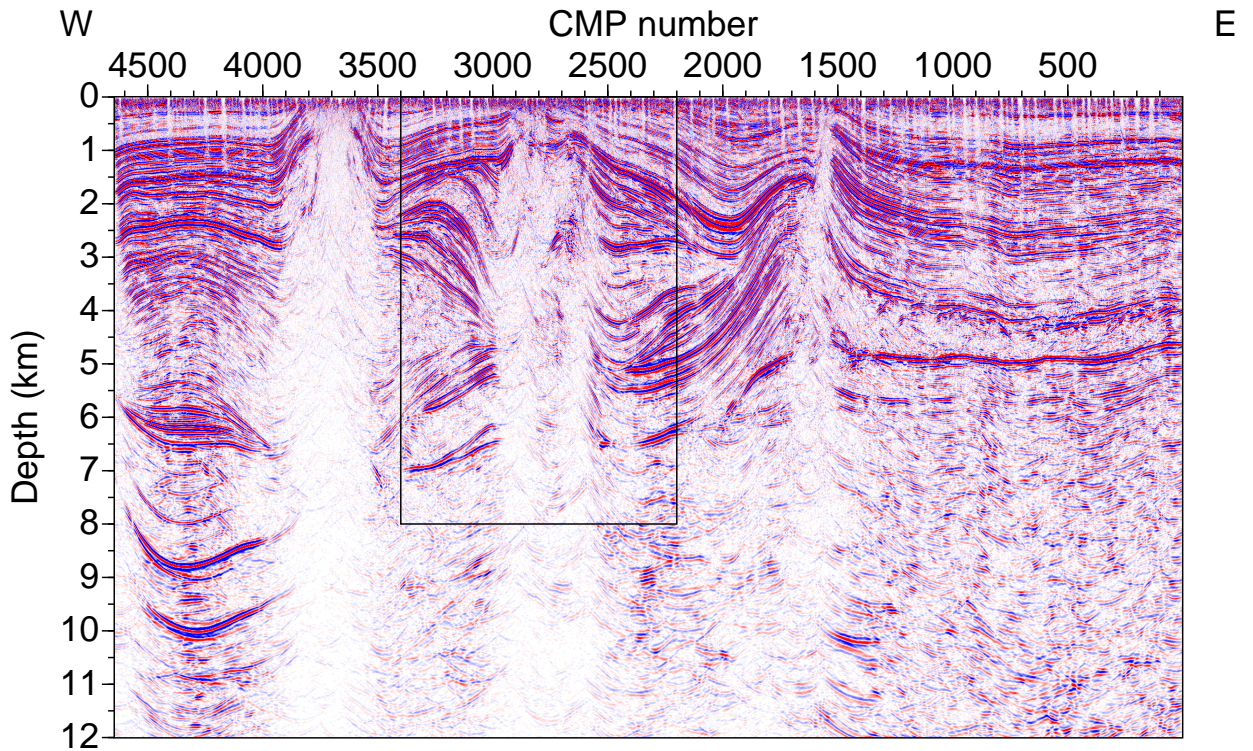


Figure 3.17: Land data: poststack depth migration of the CRS stack. The boundaries of the salt plugs are corrected for their lateral position and diffractions are focused as compared to the time stacked sections. Reflectors are clearly visible. The rectangle is enlarged in Figure 3.19(a).

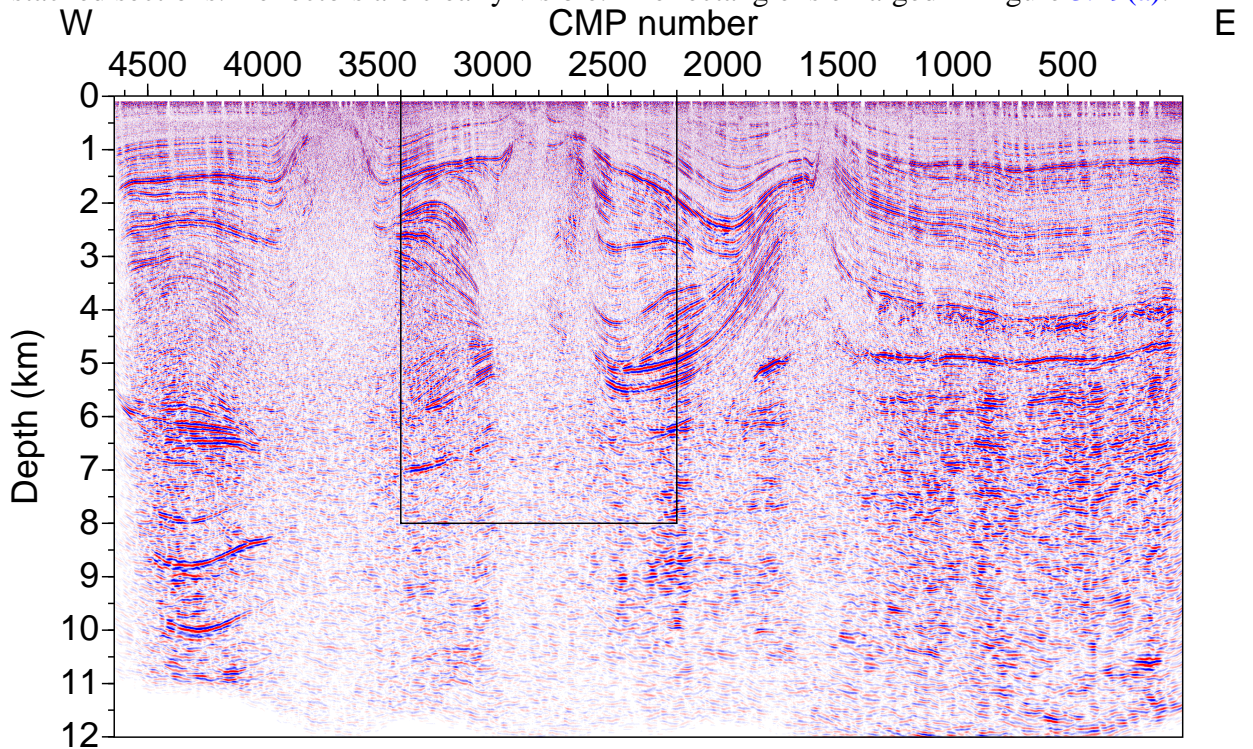


Figure 3.18: Land data: Kirchhoff prestack depth migration of the CMP gathers. The image quality is low compared to the PostSDM of the CRS stack (see Figure 3.17). Salt-sedimentary boundaries are hardly visible. The internal structure of the salt plug in the middle part of the section is poorly imaged. However, the PreSDM produced better images of pre-Permian sediments in the deeper part of the section between 0 and 3500 CMP at 5–8 km depth (below base Rotliegend). The rectangle is enlarged in Figure 3.19(b).

3.4.2 Prestack depth migration

Kirchhoff prestack depth migration was applied to the preprocessed CMP gathers. The PreSDM as applied here operates on common-offset gathers. Because of the irregular acquisition geometry, the seismograms were first resorted to obtain binned common-offset gathers with an offset bin spacing of 100 m. The migration result is shown in Figure 3.18. Low S/N ratio of the input CMP gathers and irregularity of traces lead to the low quality of the prestack depth migrated section. The upper part of the section from 0 to 5 km depth is poorly imaged. Strong lateral amplitude variations complicate the correlation of reflector elements. Salt-sediment boundaries are sometimes unclear compared to the PostSDM of the CRS stack. However, the deeper part of the section between 5 and 10 km depth at CMP 0–1500, contains a set of horizontal reflectors not clearly imaged in the PostSDM section. The prestack depth migration provides better vertical resolution than the migration after stack in this area. Reflectors appear more continuous and better suited for interpretation than the poststack depth migrated image of the same part of the section 3.17.

Comparison of the results of the CRS stack processing with the conventional processing in the area of the salt plug (Figure 3.19) shows a significant difference between the two images. Whereas the PostSDM of the CRS stack shows improved images of the internal salt reflectors and of the salt-sedimentary boundaries compared to the PreSDM, the latter shows improved images of the deeper part below base Rotliegend (>7 km depth).

Figure 3.20 shows the depth migrated CIGs. Only few irregularly located flat reflector elements are visible in the seismograms. Due to the low quality, the CIGs are only partially suited for the quality control of the migration velocities. In the noisy areas, where no reflectors are visible, the reliability of the model can not be confirmed by the CIGs. However, the part of data from 0 to 1500 CMP contains pronounced reflectors at 3 to 8 km depth that are almost flat. Also, in the western part, flat reflectors at CMP 4000 and 8 to 11 km depth are visible. In Chapter 4 of this work a method of improving the quality of prestack data is introduced, which generates CIGs of higher S/N ratio with the same velocity model. using that method, the correctness of the migration velocity model is confirmed using the new depth migrated gathers of higher quality, where much more horizontal reflector elements are visible.

3.5 Conclusions

Seismic processing using the CRS stack provided results that can help revise the structural setting and the evolution of salt plugs in the area of the Glückstadt Graben. The reprocessing of old seismic data clearly demonstrated the capability of the CRS technique to produce high-quality

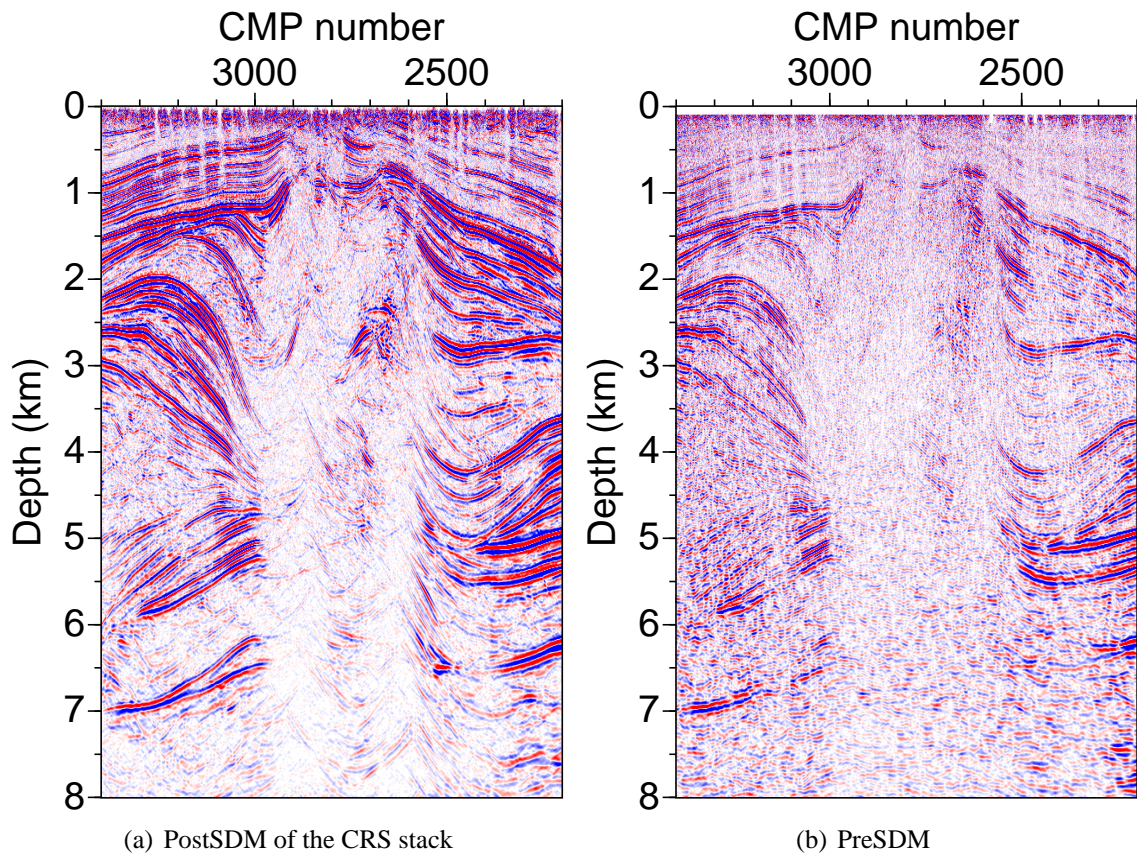


Figure 3.19: Land data: comparison of the PostSDM of the CRS stack (a) and the PreSDM of the CMP gathers (b). The enlarged images of the middle salt plug (see Figures 3.17 and 3.18) show the potential of the CRS technique to image low-fold data. Internal salt reflectors are clearly visible between CMP 2600 and 2900 at 2–5 km depth in PostSDM. Pronounced reflectors in the interval from 0 to 7 km depth are also better imaged in the PostSDM. However, the PreSDM shows the pre-Permian sediments below 7 km depth more continuously and a correlation of the sub-salt structures with the surrounding sediments can be performed more easily.

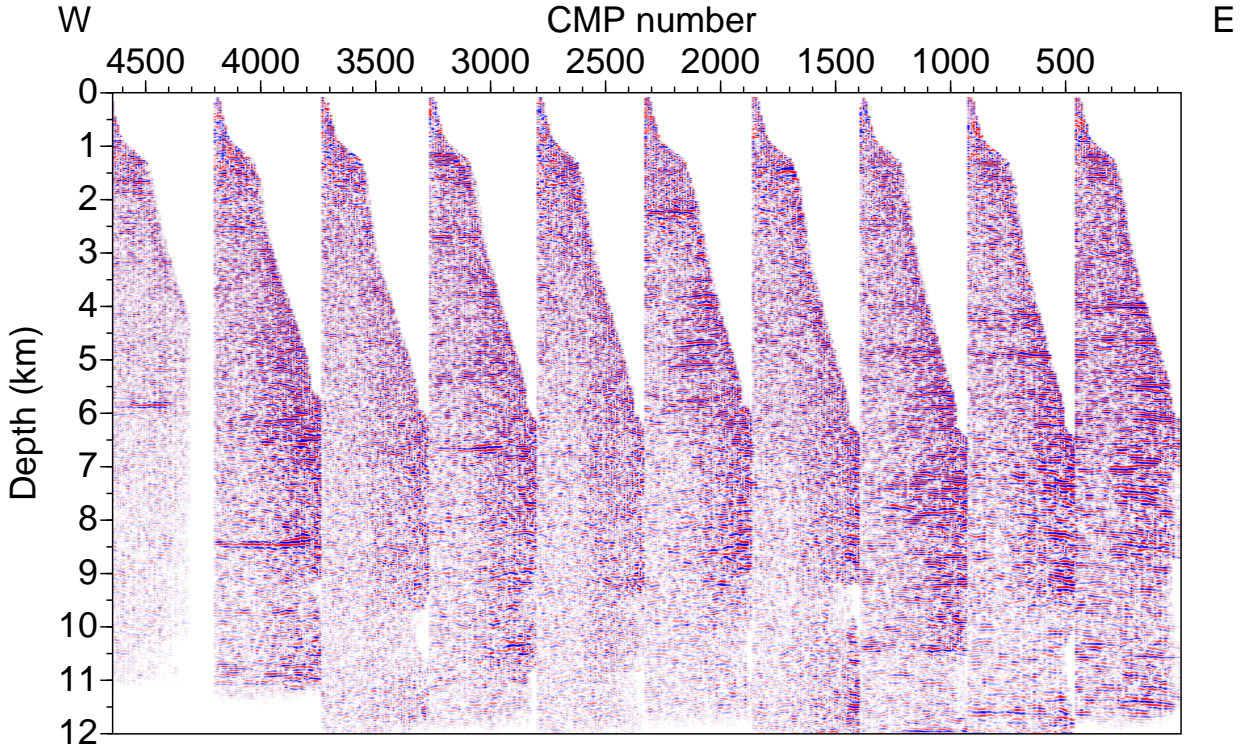


Figure 3.20: Land data: common image gathers obtained after PreSDM with the NIP-wave tomographic model. The irregular acquisition geometry and low S/N ratio of the CMP gathers result in the low quality of the depth-migrated gathers. Large residual moveout is not observed, which confirms the good quality of migration velocity model in the areas, where horizontal reflectors are visible.

images of low-fold data. The CRS stack section displays a considerably-improved S/N ratio and shows much more details than the CMP stack section. Moreover, a velocity model was built and depth migrated sections were obtained, which were so far not available for these data. Conventional velocity building methods based on residual moveout analysis of the CIGs are not well suited for these complex data since very few reflector elements are visible in the prestack gathers. In contrast reflections in the time-stacked domain with its higher S/N ratio are easily picked using the results of the CRS stack. These picks provide all necessary information for the tomographic inversion of the data. After several tomographic iterations, a smooth velocity model was obtained, which was used for the depth migration of the dataset.

Compared to conventional tomographic methods, the NIP-wave tomographic inversion does not need any user intervention after each iteration. The initial velocity model is automatically updated in order to decrease the misfit between computed and input data.

Poststack depth migration of the CRS stack provided a depth image with high S/N ratio, where some details not identified by the conventional processing are observed. The prestack depth mi-

grated section, however, has lower S/N ratio. Here, the identification of reflectors is complicated compared to the PostSDM section. The quality of the CIGs and consequently the PreSDM section can be improved by applying *the partial CRS stack* method on the original CMPs. This new method is described in the following chapter.

Chapter 4

Partial CRS stack

The quality of seismic reflection data is very important for processing. It depends on a number of factors, e.g., surface topography, the complexity of the subsurface, and the technical equipment used during the acquisition. The presence of natural and anthropogenic factors can also affect land seismic measurements (see, e.g., [Stolt, 2002](#); [Spitzer et al., 2003](#); [Chandola et al., 2004](#)). Inhomogeneities in the subsurface, the presence of fault structures and strong velocity contrasts like in the areas of salt plugs lead to a decrease of the S/N ratio, as it was shown in the land data examples in the previous chapter.

Quite often the quality of old seismic reflection data, which needs to be reprocessed, is comparably low because of the short maximum offsets, irregular acquisition, and low CMP fold. All these factors require a complex workflow to precondition the data for velocity analysis, velocity model building and other processes. The quality of time and depth migrated stacked sections is consequently poor. Furthermore, the prestack CMP gathers of real land data may contain sparse seismograms located irregularly over the short offset range. Regularisation of seismograms and filling the gaps in case of missing data is usually performed using different binning and interpolation techniques (see, e.g., [Brune et al., 1994](#); [Yilmaz, 2001](#); [Stolt, 2002](#); [Fomel, 2003](#); [Spitzer et al., 2003](#); [Chandola et al., 2004](#); [Herrmann et al., 2008](#)).

Chapters 2 and 3 demonstrated the application of the CRS stack to enhance the quality of *stacked* time sections and corresponding PostSDM. However, the PreSDM of noisy CMP gathers of land data produces depth migrated section of comparably lower quality than the PostSDM of the CRS stack. This chapter shows the potential of the CRS stack method to improve the quality of *prestack* data. The CRS traveltimes formula, where the dip of the reflector element is incorporated, is used to compute new partially-stacked CRS supergathers, where each trace is a result of summation of data along the CRS stacking surface. The number and location of traces in the produced supergathers can be defined, e.g., to fill in missing offsets. Since no interpolation but a

summation of data is performed, the method is very robust in the presence of non-coherent noise. Moreover, a regularisation of traces can be achieved with the partial CRS stack. As described in Müller (1999); Jäger et al. (2001), the CRS stacking surface approximates the traveltimes of seismic reflection data more precisely than the NMO/DMO stack. Therefore, the application of the CRS stacking surface to produce regularised data can be superior to the methods based on the conventional NMO/DMO and binning/interpolation techniques described, e.g., by Brune et al. (1994).

4.1 Basic idea of partial CRS stacks

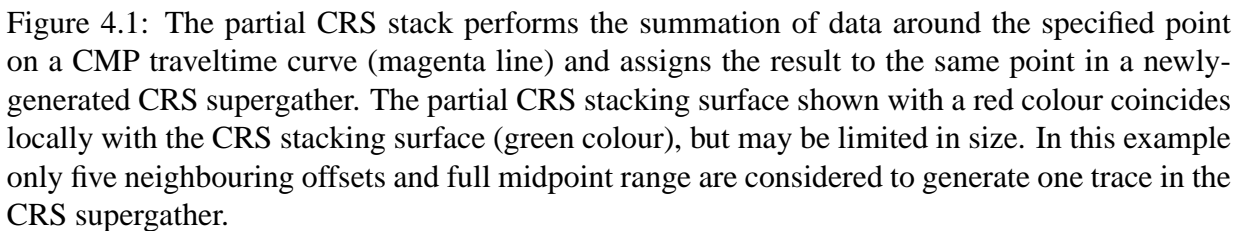
Partial CRS stacks (Baykulov and Gajewski, 2009, 2008) calculate a stacking surface around a specified point defined by its offset and traveltime coordinates in a chosen CMP location and perform the summation of data along that surface. The result of summation is assigned to a new sample with the same CMP, offset, and time coordinates. Repeating this procedure for all desired points generates a new gather that is called (*partially stacked*) *CRS supergather* in the following. In Figure 4.1, the partial CRS stack surface is shown as a red grid around the specified event (red point) in a selected CMP gather. That surface coincides locally with the CRS stack surface introduced in Chapter 1, but the size of the partial CRS stacking surface is smaller.

The partial CRS stacking surface is defined by the zero-offset (t_0) time of the considered point and the corresponding CRS parameters. The hyperbolic traveltime formula, introduced in Chapter 1, describes the traveltime as

$$t^2(m, h) = \left(t_0 + \frac{2 \sin \alpha}{V_0} m \right)^2 + \frac{2 t_0 \cos^2 \alpha}{V_0} \left(\frac{m^2}{R_n} + \frac{h^2}{R_{nip}} \right), \quad (4.1)$$

where h is half source-receiver offset, m is the midpoint displacement with respect to the considered CMP position, t_0 is the zero offset two-way traveltime, and α , R_n , and R_{nip} are the CRS parameters defined for that t_0 .

To use all available traces for partial stacking it is necessary to define the same size of the surface as it is used for the CRS stack. However, the maximum offset or midpoint distance from the selected CMP point may be smaller than that defined for the CRS stack surface. The measurements of the partial CRS stack surface in offset and midpoint dimensions, therefore, are called *partial CRS stack apertures* in the following. These apertures should be adjusted according to the aim of processing, and may enclose only some traces on the CRS stacking surface around the chosen point. Stacking more traces may be necessary to fill large data gaps present in the CMP gathers. In that case the information from the neighbouring CMPs or from the neighbouring offsets is used to generate a new trace in the CRS supergather.



The incorporation of the midpoint displacement m into the calculation of the partial CRS stacking surface acknowledges the reflector dip in the construction of CRS supergatherers. As a result, the partial CRS stack method is superior to the conventional CMP binning technique (for detail see, e.g., [Yilmaz, 2001](#)), where the dip of the structure is not considered. As shown in [Müller \(1999\)](#) and [Jäger et al. \(2001\)](#), the CRS stacking surface describes the reflection response better than the NMO/DMO stack. Therefore, the partial CRS stack should produce better results than the existing NMO/DMO interpolation schemes as described by [Brune et al. \(1994\)](#). Only if the shape of the true subsurface reflector is identical to the shape of the specific ZO isochrone, the

NMO/DMO stacking surface describes the data identical to the partial CRS stacking surface (see, e.g., Jäger et al., 2001).

Since the partial CRS stacking surface is calculated not only for the zero-offset trace but for every specified source-receiver offset and the result of partial stacking is assigned to the trace with the specified offset, the output gathers are not NMO-corrected. Therefore, the partial CRS stack supergathers may be used further in many standard processing steps, e.g., velocity analysis, stacking, or migration.

4.2 Calculation of partial CRS stacking surface

The partial CRS stacking surface is calculated in a selected CMP location for every specified sample $A(t_A, h_A)$, where t_A is two-way traveltimes, and h_A is half source-receiver offset. The accurate zero-offset time and the corresponding CRS parameters (α, R_n, R_{nip}) , describing this event, need to be found. In the course of this thesis a search algorithm was developed and optimised to find zero-offset traveltimes for offset locations h_A of the partial CRS stacking surface that exactly fits the sample A . The CRS parameters for each CMP location in the stacked volume need to be known. These CRS parameters are determined by the automatic search described by Müller (1999), Jäger et al. (2001) and Mann (2002).

The zero-offset traveltimes search is performed for every CMP location of the data independently. Since the CMP traveltimes curve is a special case of the CRS stack surface when the midpoint distance $m = 0$ (see equation 1.7), this search is simplified to find the CMP hyperbola that fits the event in A best. All zero-offset traveltimes within the range $[0; t_A]$ and the corresponding CRS parameters are tested to determine the hyperbola that has the minimum time deviation from t_A at the offset h_A . Following from equations 1.7 and 1.8, the traveltimes of best-fitting CMP curve is described as

$$t^2(h) = t_0'^2 + \frac{2t_0' \cos^2 \alpha}{V_0} \frac{h^2}{R_{nip}}, \quad (4.2)$$

where t_0' is the tested zero-offset traveltimes, and α and R_{nip} are the CRS parameters corresponding to that t_0' .

However, the defined hyperbola does not fit the event $A(t_A, h_A)$ exactly because only discrete values of zero-offset traveltimes may be tested. The determined t_0' , may, therefore not be used to describe the partial CRS stacking surface because the events would not be stacked coherently in that case. In conclusion, the CMP hyperbola has to be corrected to exactly fit the point A .

Assuming that α and R_{nip} are varying smoothly in the vicinity of the considered event A , these parameters are kept fixed in the equation 4.2. Setting the traveltime t_A and the offset h_A of the event A into equation 4.2 yields

$$t_A^2 = t_0^2 + \frac{2t_0 \cos^2 \alpha}{V_0} \frac{h_A^2}{R_{nip}}, \quad (4.3)$$

where t_0 is a zero-offset traveltime of a CMP traveltime curve that fits the event A exactly. Solving this quadratic equation with respect to t_0 and neglecting the negative solution results in

$$t_0 = -\frac{h_A^2 \cos^2 \alpha}{V_0 R_{nip}} + \sqrt{\left(\frac{h_A^2 \cos^2 \alpha}{V_0 R_{nip}}\right)^2 + t_A^2}, \quad (4.4)$$

where α and R_{nip} are defined for the traveltime t'_0 . Here, the R_{nip} , which is a measurement of a reflector depth, is assumed to be positive. Considering negative values of R_{nip} , which may occur in some situations, it will be necessary to take the second solution of the equation 4.3 into account. The such-defined t_0 is now used in equation 4.1 to construct the partial CRS stacking surface that exactly fits the considered event A . This surface is used to sum up the data coherently. The resulting sum is divided by the number of traces involved in the summation. So, the amplitudes of signal in the generated CRS supergather are comparable with the amplitudes of signal in the CMP gathers, whereas the noise is attenuated.

4.3 Synthetic data tests

In order to test the partial CRS stack method and to show its advantages, I applied it to the Sigsbee 2A synthetic dataset.

4.3.1 Noise-free Sigsbee 2A dataset

Sigsbee 2A is a constant density acoustic synthetic dataset released in 2001 by the "SMAART JV" consortium. It models the geologic setting found in the Sigsbee escarpment in the deep water Gulf of Mexico. In this study, I consider only that part of the dataset that does not contain the salt structure. The data do not contain free surface multiples and almost no internal multiples due to very low acoustic impedance contrasts. The interval velocity model used for the generation of

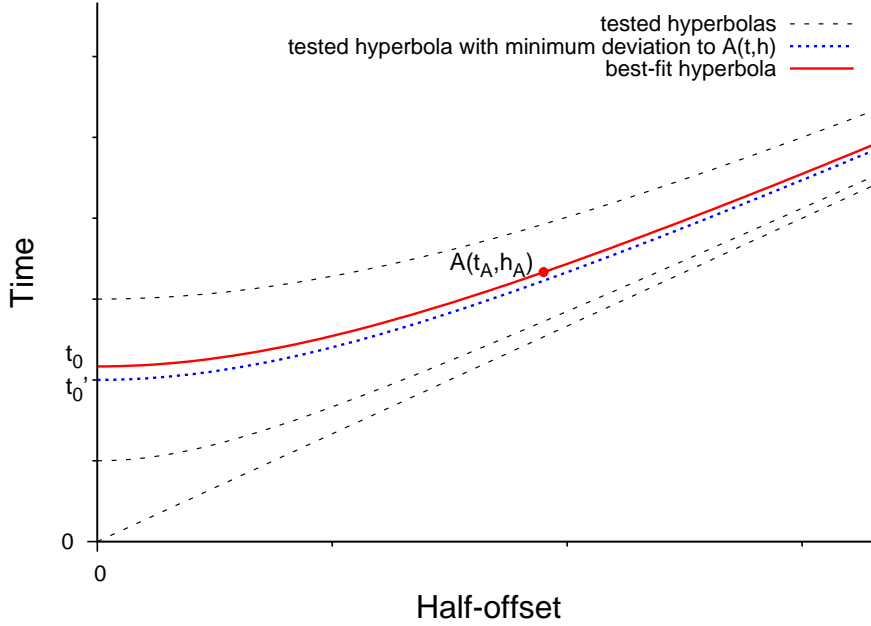


Figure 4.2: Tested travelttime curves in the search for the best-fit hyperbola for a sample $A(t_A, h_A)$ in the CRS supergather. The ticks on the vertical axis correspond to the time samples of the data.

seismograms is shown in Figure 4.3(a). The model has been computed as a linear velocity function with fluctuations of up to about 3%. The linear function of interval velocity V is described as

$$V(Z) = V_0 + 0.3(Z - Z_{seafloor}), \quad (4.5)$$

where V_0 is 1500 m/s, Z is depth, and $Z_{seafloor}$ is the depth of the water bottom. The reflection interfaces result of velocity contrasts that fluctuate within ± 100 m/s relative to the linear velocity function, enough to generate reflections.

A number of normal and thrust faults and diffractor points are present in the data. The shot spacing is 45.72 m with 348 channels per shot and a receiver spacing of 22.86 m. Therefore, the resulting CMP interval is 11.43 m, and the maximum CMP fold is 87. The data are sampled every 8 ms with a total recording time of 12 s. Figure 4.3(b) shows a typical CMP gather with up to 3500 m offset and TWT=10 s.

In total, I processed 500 CMP with the CRS stack method. First, the CRS parameters were estimated in a similar way as described in the previous chapters of the paper. I did not used a reference velocity model for the stacking velocity search for this data, i.e., only the surface velocity and the range of tested velocity values were defined. Table 4.1 shows the summarised processing parameters used during the automatic CRS searches. The maximum midpoint deviation m was set to 260 m at TWT=2.3 s and 900 m at TWT=11 s and interpolated linearly for intermediate

values. An offset range of 914 m at TWT=2.3 s and 3800 m at TWT=11 s was used and again interpolated linearly. Figure 4.4 shows the resulting sections of CRS stacking parameters.

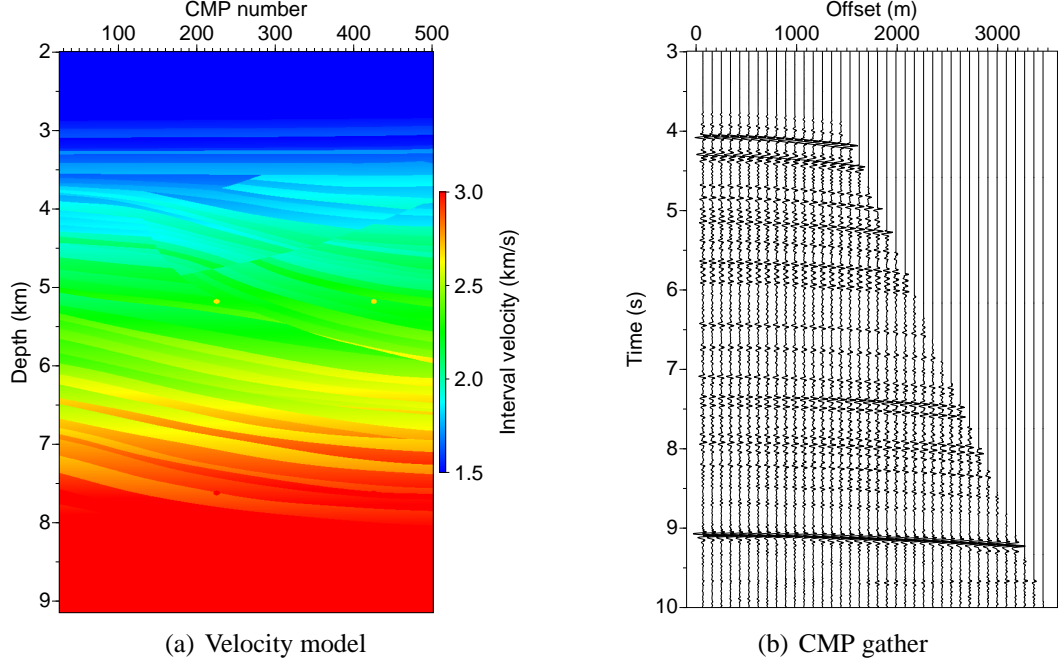


Figure 4.3: Sigsbee 2A data: the true interval velocity model (a) and a CMP gather (b). Fluctuations of interval velocities of up to ± 100 m/s from the gradient model produce the reflections in the CMP gather.

Surface velocity	1500 m/s
Reference velocity model	not used
Tested velocity range	[1400; 5000]
Maximum dip angle	60°
Minimum offset aperture	914 m at 2.3 s
Maximum offset aperture	3800 m at 11 s
Minimum midpoint aperture	260 m at 2.3 s
Maximum midpoint aperture	900 m at 11 s

Table 4.1: Sigsbee 2A data: processing parameters used for the automatic CRS search.

4.3.2 Sigsbee 2A data with sparse traces

In order to test the partial CRS stack method on sparse data, I randomly eliminated some traces from the CMP gather shown in Figure 4.3(b). As a result, only 20 seismograms spaced irregularly remained in the gather (see Figure 4.5(a)). The CRS parameters obtained during the automatic

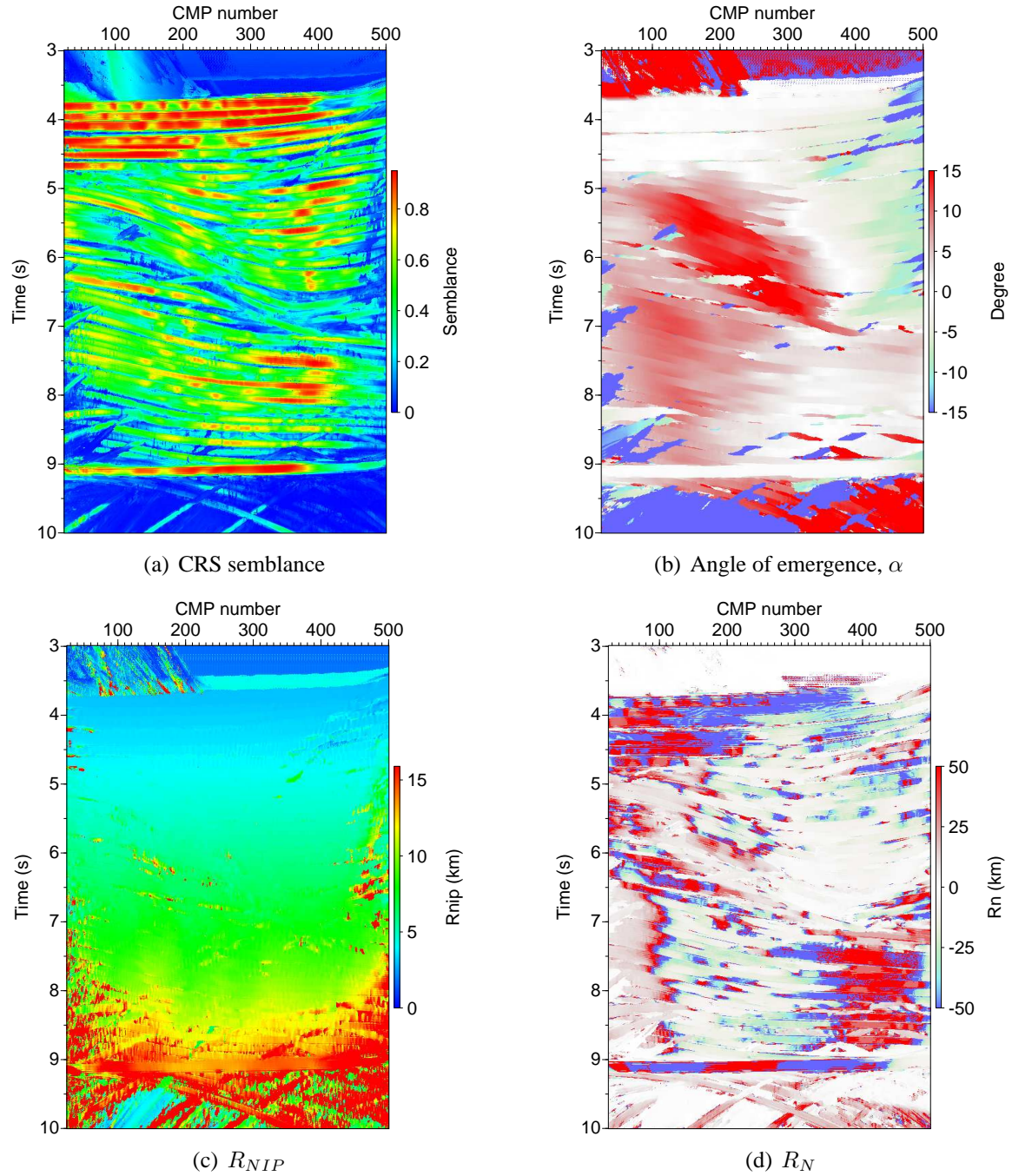


Figure 4.4: Sigsbee 2A data: results of the automatic CRS parameter searches.

searches from the original data were used to compute partial stacked CRS supergathers. The partial CRS stack aperture in offset dimension was limited to contain only one offset, corresponding to one common-offset red curve in Figure 4.1. In the midpoint direction the aperture was the same as for the CRS stack (see Table 4.1). The resulting CRS supergather is shown in Figure 4.5(b). It contains much more traces than the original sparse CMP gather. The areas of missed traces are filled using the information from the neighbouring CMPs located at the partial CRS stack surface. The gathers are muted according to the defined offset aperture used during the CRS parameters search. Because of the larger number of traces, reflections in the CRS supergathers appear sharper and can be better distinguished in comparison to the CMP gather (compare to Figure 4.3(b)).

CMP gathers and CRS supergathers were stacked with the same stacking velocity model obtained from the original data. It is possible to use the partial CRS stacked supergathers during the automatic CMP search to define a more reliable stacking velocity model and CRS parameters. However, this is not yet implemented, and will be a target of further investigations. This work emphasises the improvement of the data quality only due to the partial stacks, thus the CRS parameters determined for the original data were used.

Figure 4.7 depicts the resulting ZO stacked sections. The ZO CMP stack section (Figure 4.7(a)) displays a lower quality in the areas of fault structures and steep dipping layers. The CRS supergather stack (Figure 4.7(b)) shows better continuity of horizons at all time levels and produced a better image of conflicting dip areas.

Conflicting dips areas are a general problem to the CRS stack method. For crossing reflections only one dip is considered during the automatic parameter search with preference to the most coherent, i.e., strongest event. However, it is possible to analyse conflicting dips separately, which results in a number of different CRS stack parameters (α , R_n , R_{nip}) for every point t_0 in conflicting dip areas. Although the partial CRS stack method takes the information about different conflicting dips into account, the automatic parameter search for Sigsbee 2A data was adjusted to consider only one dip. Therefore, the primary events were preferred, but the diffractions were attenuated as it is seen by comparing Figures 4.7(a) and 4.7(b). Nevertheless, the stacked section of the CRS supergathers appears clearer and better suited for interpretation than the CMP stack section.

4.3.3 Sigsbee 2A data with noise

In order to show the advantages of applying the CRS supergather method to noisy data, I added Gaussian noise with $S/N=20$ to the original seismograms. The S/N ratio was computed with respect to a signal with the maximum amplitude. As a result, only the strongest events like the

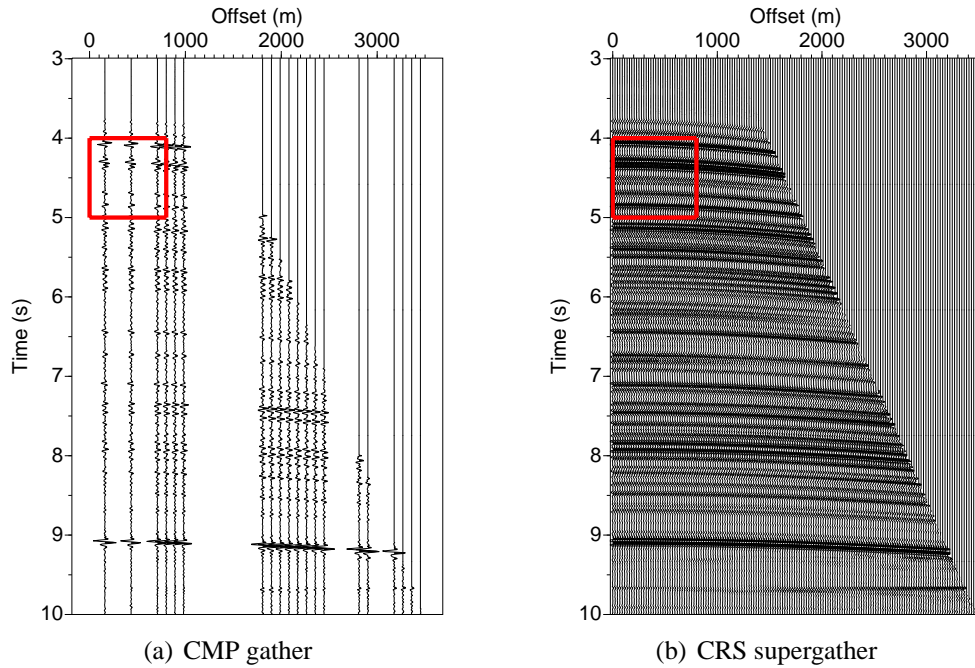


Figure 4.5: Sigsbee 2A sparse data: (a) the seismograms were randomly removed from the original CMP gather (Figure 4.3(b)) to obtain a sparse irregularly sampled gather. As a result, 20 traces remained. (b) CRS supergather. The partial CRS stacking increased the number of traces and filled the gaps using the information from neighbouring traces. The red rectangles are enlarged in Figure 4.6.

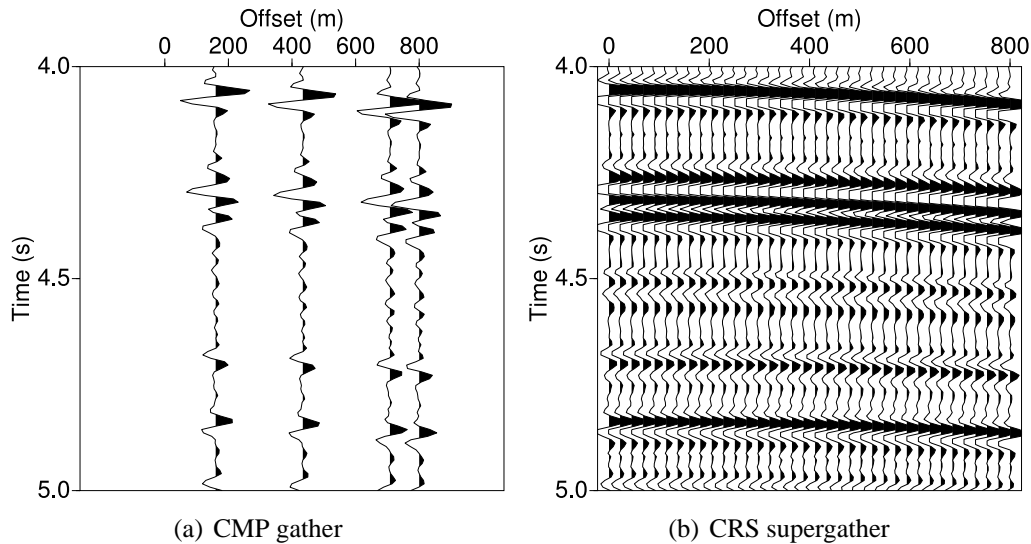


Figure 4.6: Sigsbee 2A sparse data: enlarged images of the CMP gather (a) and the CRS supergather (b).

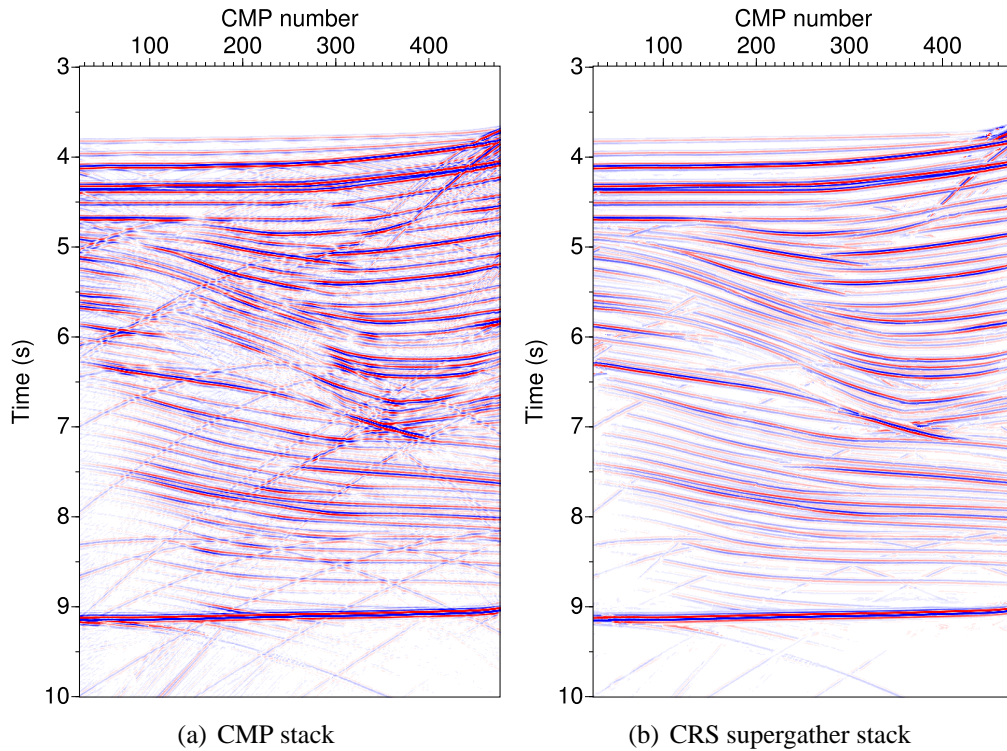


Figure 4.7: Sigsbee 2A sparse data: the conventional CMP stack (a) has lower quality in conflicting dips areas. In the CRS supergather stack (b), reflections are more continuous and appear clearer. Diffractions are attenuated.

reflection from the water bottom (4 s TWT) and the bottom of the model (9 s TWT) are visible in the CMP gather (Figure 4.8(a)). Since the amplitudes of all other reflections are lower, they are almost not visible. An automatic CRS parameter search was carried out for the noisy seismograms. The obtained CRS parameters were used to build the partial stacked CRS supergathers. The result is shown in Figure 4.8(b) and as a close-up in Figure 4.9. Compared to the CMP gather, the reflections in the CRS supergather are clearly visible at all times. The noise is still present, but the S/N is significantly increased.

Figure 4.10 demonstrates the advantage of CRS supergathers for the stacking. Whereas the CMP stack of the noisy seismograms (Figure 4.10(a)) has a lower S/N ratio than the CMP stack in Figure 4.7(a), the stacked CRS supergathers (Figure 4.10(b)) show almost no visible differences to the stacked supergathers without noise (Figure 4.7(b)). This means that the partial CRS stack is very stable in the presence of non-coherent noise. This advantage, however, requires a reliable determination of the CRS parameters (α , R_n , R_{nip}).

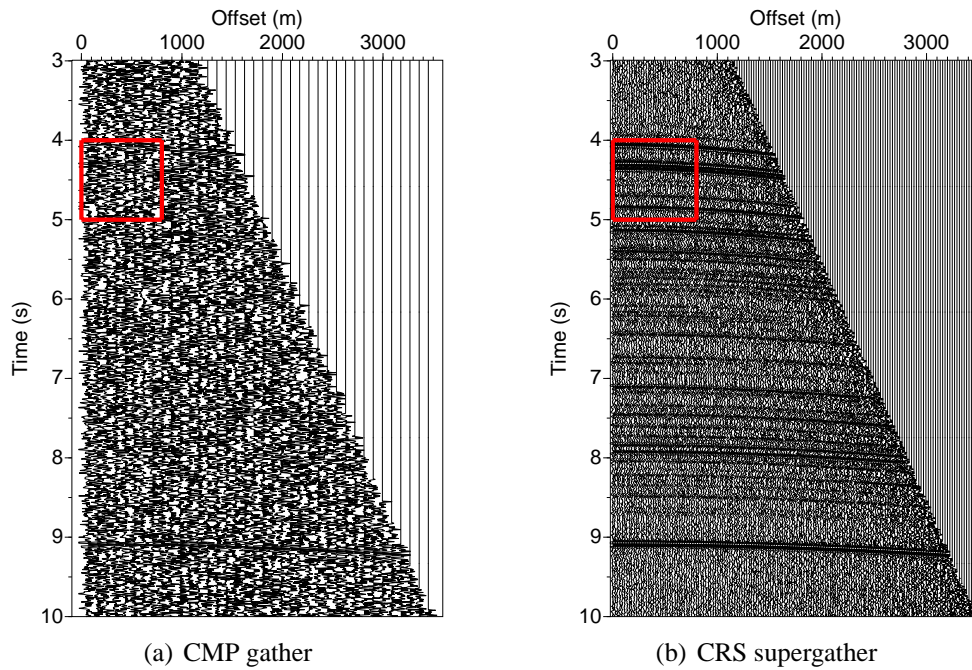


Figure 4.8: Sigsbee 2A data with noise: the CMP gather (a) contains less traces than the partial stacked CRS supergather (b). Reflections in the CMP gather are hardly visible. The CRS supergather displays a significantly increased S/N and reflections are clearly visible from 4 to 9 s TWT. The red rectangles are enlarged in Figure 4.9

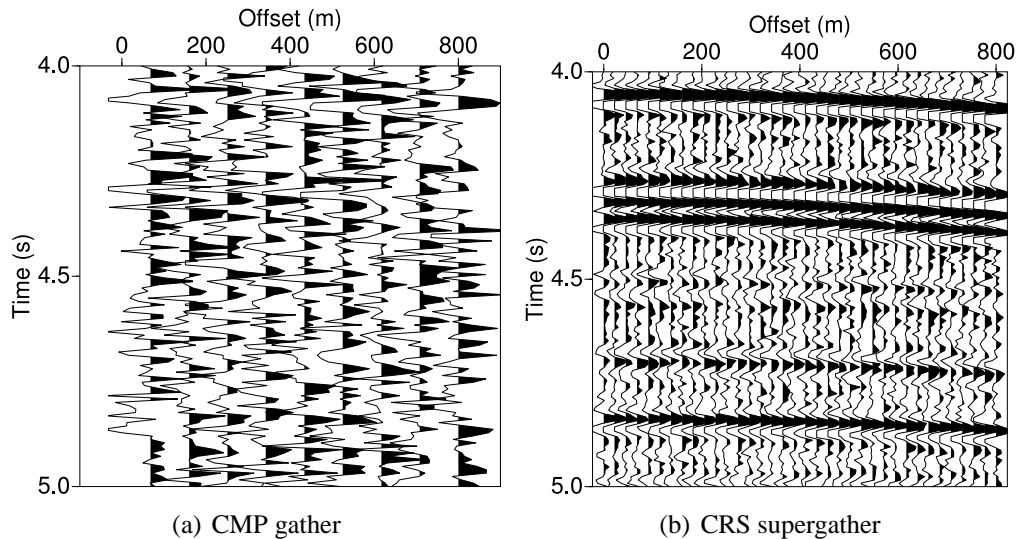


Figure 4.9: Sigsbee 2A data with noise: enlarged images of the CMP gather and the CRS supergather as shown in Figure 4.8.

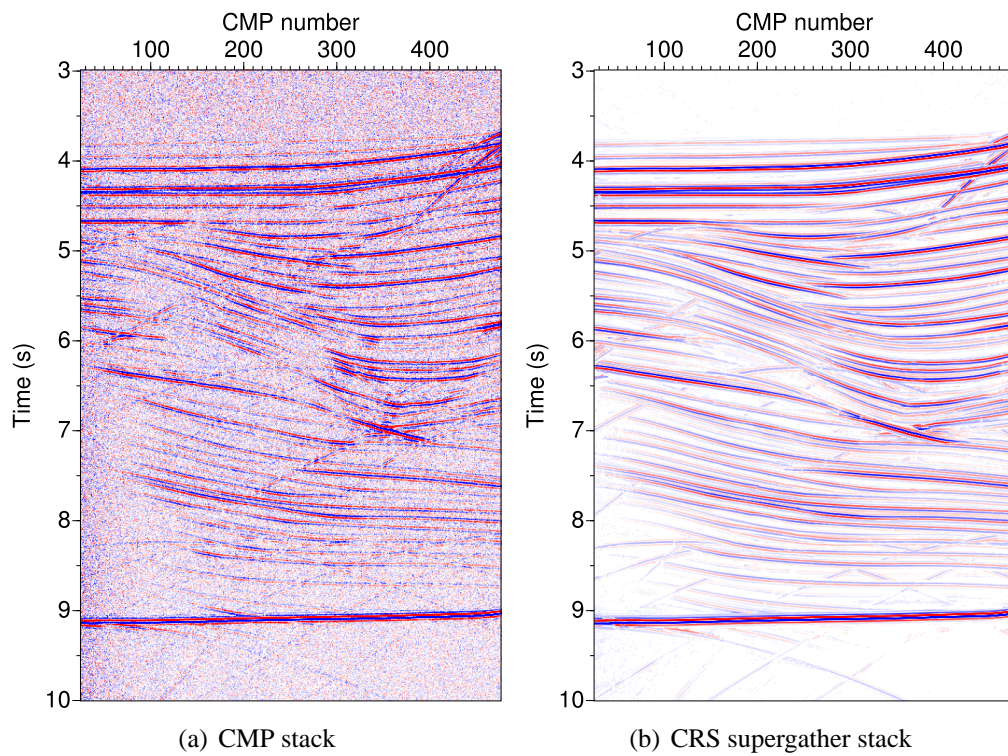


Figure 4.10: Sigsbee 2A data with noise: the conventional CMP stack (a) has lower S/N ratio than the CMP stack section without noise (Figure 4.7(a)). The CRS supergather stack (b) shows almost no visual differences to the stacked section without noise (Figure 4.7(b)).

4.4 Application to land data and depth migration

After successful tests of the partial CRS stack on the synthetic dataset, I applied it to the low-fold land data from Northern Germany introduced in Chapter 3. Figure 4.11(a) shows a typical CMP gather of the data. Although preprocessing was applied, the S/N ratio of the seismograms is low. About 20 traces are distributed irregularly over the full offset range, leading to difficulties in identifying reflections.

Conventional binning of neighbouring CMP gathers into a new gather does not yield the desirable quality enhancement of the prestack data because merging of data without the correction for the dip of the layers leads to smearing. Figure 4.11(b) shows a binned gather obtained by combining ten CMPs, corresponding to a bin size of 200 m. The resulting CMP bin provides a better coherency of the reflection events in the upper part, but it does not completely fill the data gaps at certain offsets (around 2000 m and 3700 m). Combining 20 CMPs together (bin size 400 m) as shown in Figure 4.11(c) fills these gaps but decreases the energy of reflection events. Combining more CMPs would further decrease the coherency of the reflection events.

Since the CRS parameters were already estimated for the dataset (see Chapter 3, Figures 3.7 to 3.10) they were used to generate the partial stacked CRS supergathers. The partial CRS stack aperture m was set to 400 m at the surface and 2000 m at 5 s TWT, which is the same as used during the CRS parameter search. Regularisation of traces was applied to the dataset with the partial CRS stack aperture in offset dimension adjusted to 100 m.

An example of the resulting CRS supergathers is shown in Figure 4.11(d). A significantly larger number of traces is present in the CRS supergather than in the original CMP gather. The traces are well distributed and fill the gaps in Figure 4.11(a). Reflections are clearly visible at all times down to 4 s TWT. Also, some events at TWT = 4.5–5 s, 1000–2000 m offset can be observed. Compared to the binned CMP gathers (Figures 4.11(b) and 4.11(c)), the CRS supergather provides a better S/N ratio and shows a better continuity of reflections at all time levels.

4.4.1 PreSDM of CRS supergathers

Prestack Kirchhoff depth migration was applied to the CRS supergathers with the same parameters as used for the original CMPs (see Table 3.4). In order to demonstrate the benefits of the partial CRS stack only, the NIP-wave tomography model derived from the original data (see Figure 3.16) was used to migrate both sets of original and partial stacked gathers. The improvement of the migration velocity model using the partial stacked CRS supergather for the NIP-wave tomographic inversion may be the target of further investigations. Performing a PreSDM with the

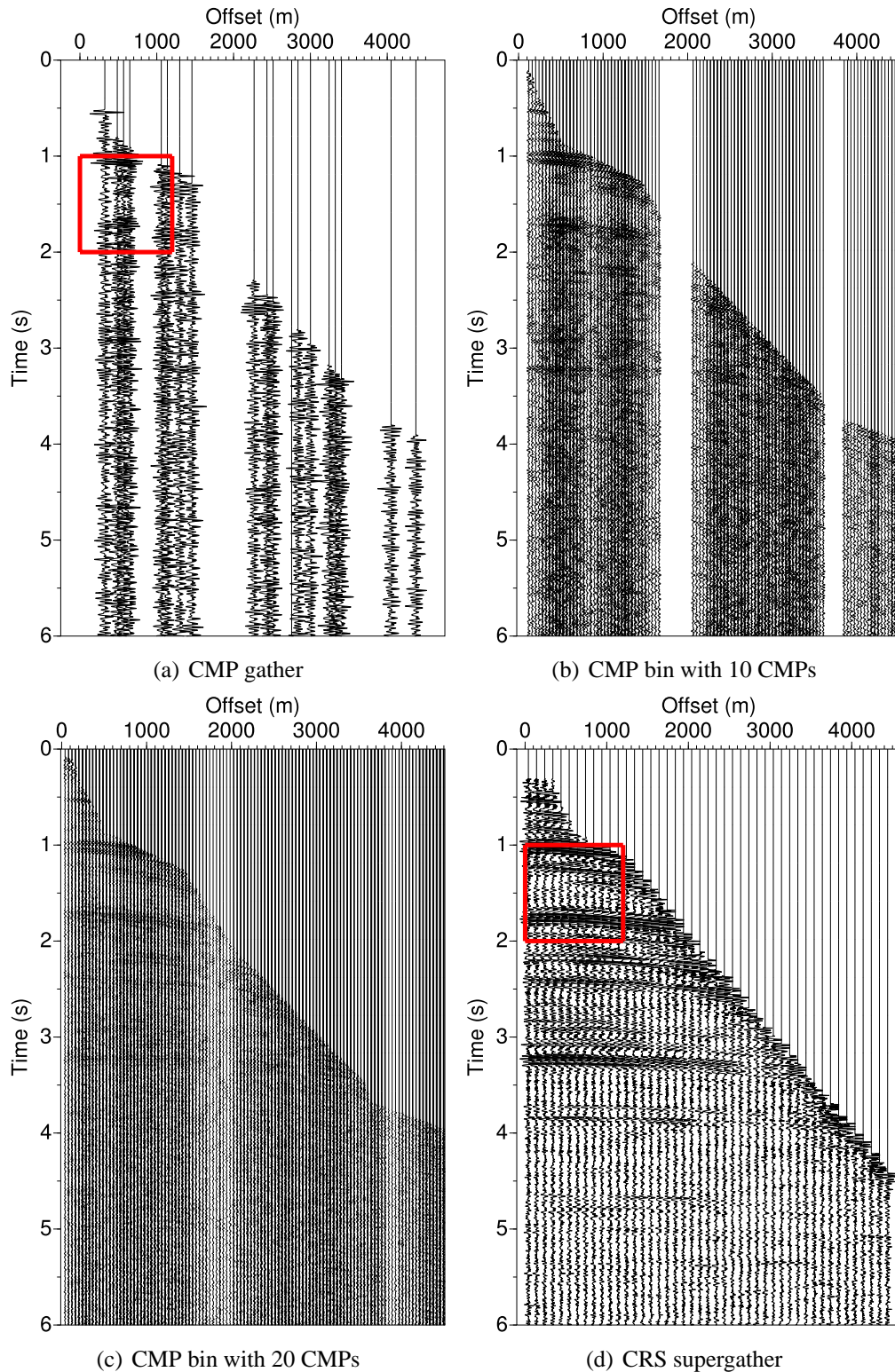


Figure 4.11: Real land data from Northern Germany: the CMP gather (a) has about 20 traces distributed irregularly and is not well suited for advanced seismic processing as coherent reflection events can not be observed. Combination of more CMP gathers into a new one, ten CMPs for (b) and 20 CMPs for (c), increases the coherence of events, but does not increase the S/N ratio. The CRS supergather (d) provides significantly increased S/N ratio and increased reflection continuity since the information about reflector dips is incorporated in the partial stacks during the formation of supergathers. The red rectangles are enlarged in Figure 4.12.

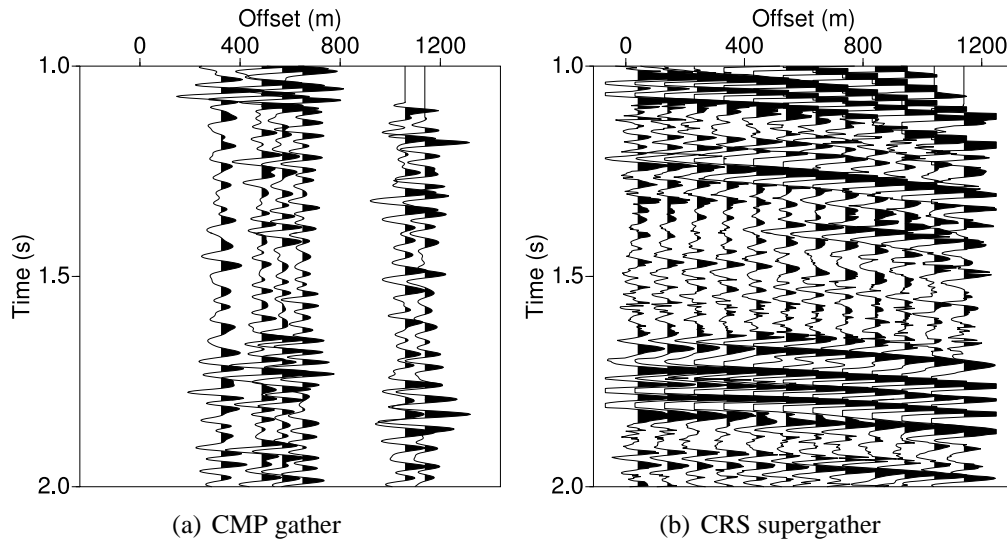


Figure 4.12: Close-up of real land data from Northern Germany presented in Figure 4.11. (a) the CMP gather contains only a few traces with irregular spacings. Reflections are not visible, the S/N ratio is low. (b) The partial stacked CRS supergather contains more traces with higher S/N ratio than the CMP gather. The CRS supergather is regularised, and the data gaps present in the CMP gather are filled. Reflections are clearly visible and can be used for further processing steps, e.g., velocity analysis or migration.

original data yields the depth-migrated section with low S/N ratio shown in Figure 3.18. Exemplarily chosen CIGs shown in Figures 4.13(a) and 4.13(c) are only partially suited for residual moveout analysis and quality control. Only the strongest reflector at 1.2 km depth can be seen in Figure 4.13(a) and at 2, 4, 5, and 6 km depth in Figure 4.13(c).

The PreSDM section obtained from CRS supergather is shown in Figure 4.15. It shows a significant improvement of image quality (compare enlarged images of the middle salt plug in Figures 4.17 and 4.16). Horizons are more continuous and a higher S/N ratio is obtained. PreSDM of CRS supergather provides better resolution than the original CIGs (see Figures 4.13 and 4.14). Reflectors in the improved gathers are clearly visible and can be easily identified in Figure 4.19.

The zoomed images of internal salt structure presented in Figure 4.18 show that the PreSDM of CRS supergather produced a depth section with a quality comparable to the PostSDM of the CRS stack. This result is very important for the geological interpretation in the study area. The horizontal depth migrated CRS supergather (4.19) confirm the consistency of the velocity model used for migration with the data, which was hardly possible using the conventional CIGs.

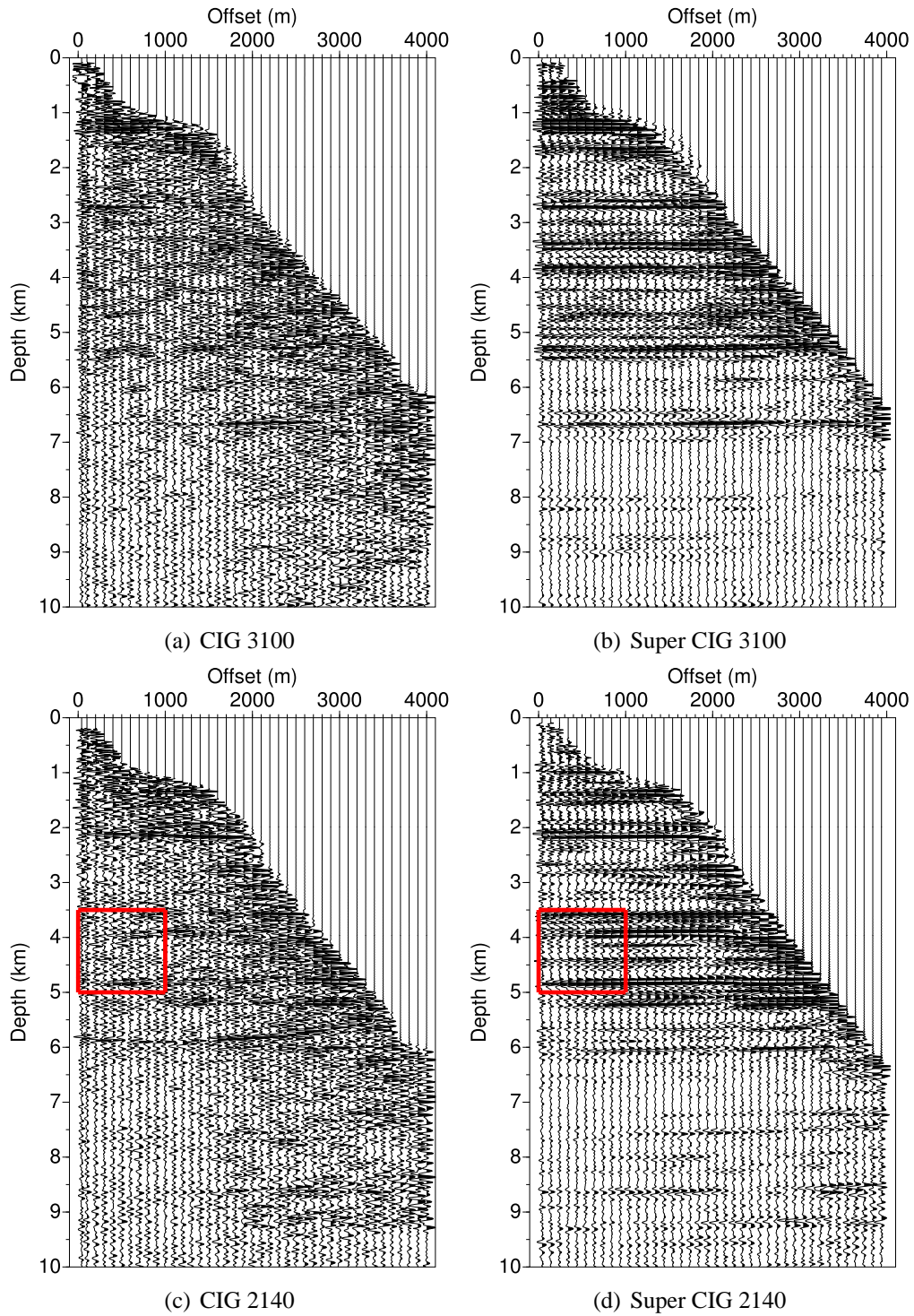


Figure 4.13: CIGs of real land data located to the left and right of the salt plug (see Figure 4.16 and Figure 4.17). The conventional CIGs display only the strongest reflectors at 1.2 km depth for CIG 3100 (a) and at 2 to 6 km depth for CIG 2140 (c). The corresponding depth migrated CRS supergather (b, d) have an increased S/N ratio and reflectors at depths down to 9–10 km are visible. The red rectangles are enlarged in Figure 4.14.

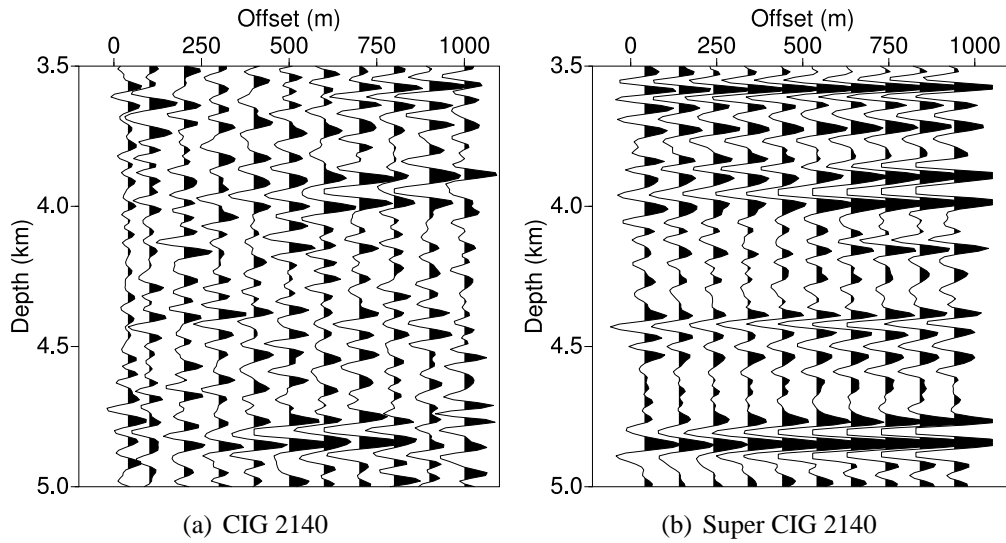


Figure 4.14: Zoom of prestack depth migrated CIGs of real land data as presented in Figure 4.13. The conventional CIG (a) is not suited for residual velocity analysis and quality control since the reflectors are hardly visible. The PreSDM of the partial stacked CRS supergather (b) shows much more reflector elements, which allows further residual moveout analysis and quality control of the depth velocity model.

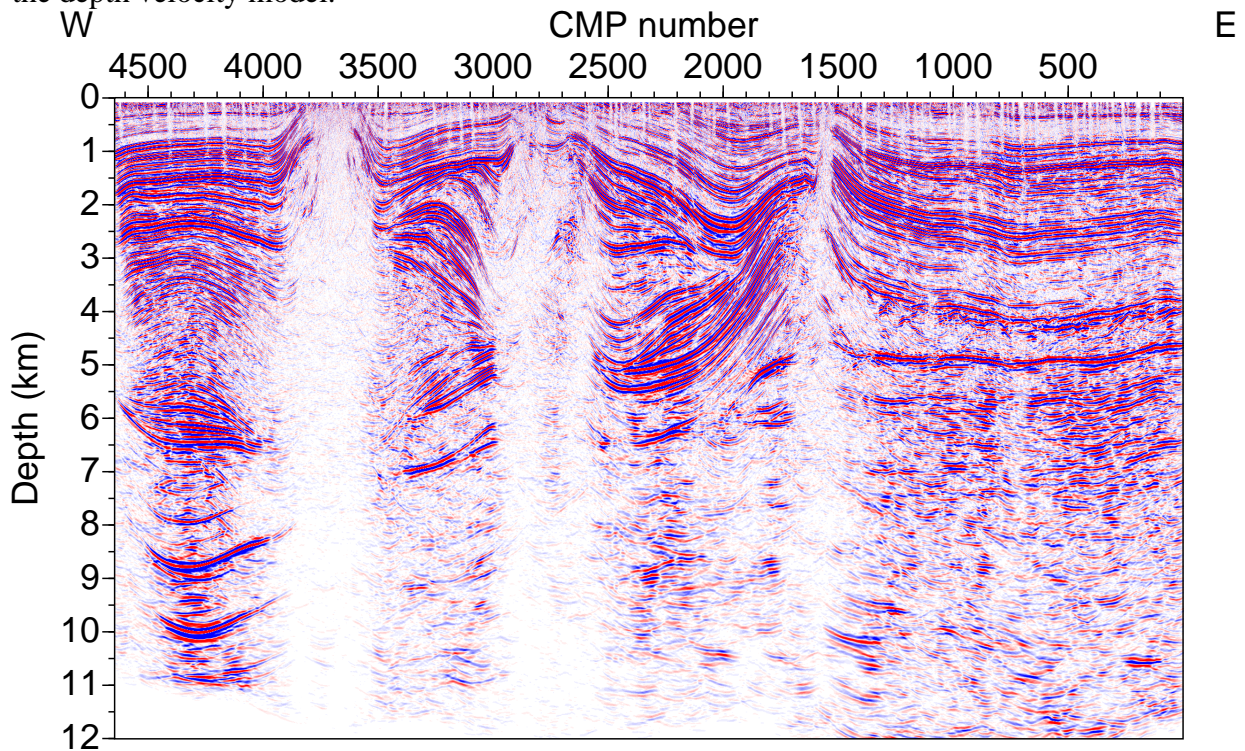


Figure 4.15: Kirchhoff prestack depth migration of the CRS supergathers. The image quality is high compared to the original PreSDM section (see Figure 3.18). Salt-sedimentary boundaries are clearly visible. The internal structure of the salt plug in the middle part of the section is significantly improved.

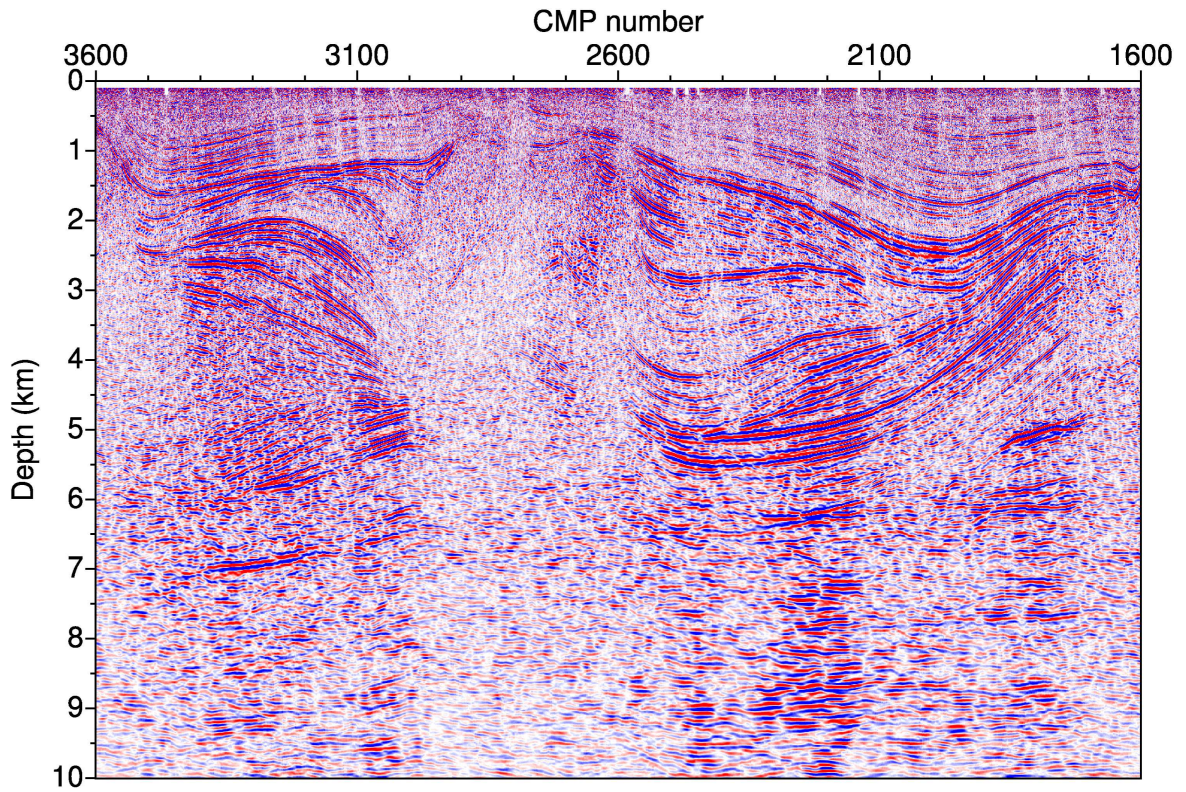


Figure 4.16: Land data: conventional PreSDM section in the salt plug area. The S/N ratio is low. Reflectors are not continuous. The internal structure of the salt plug and the reflectors below 7 km depth are hardly visible.

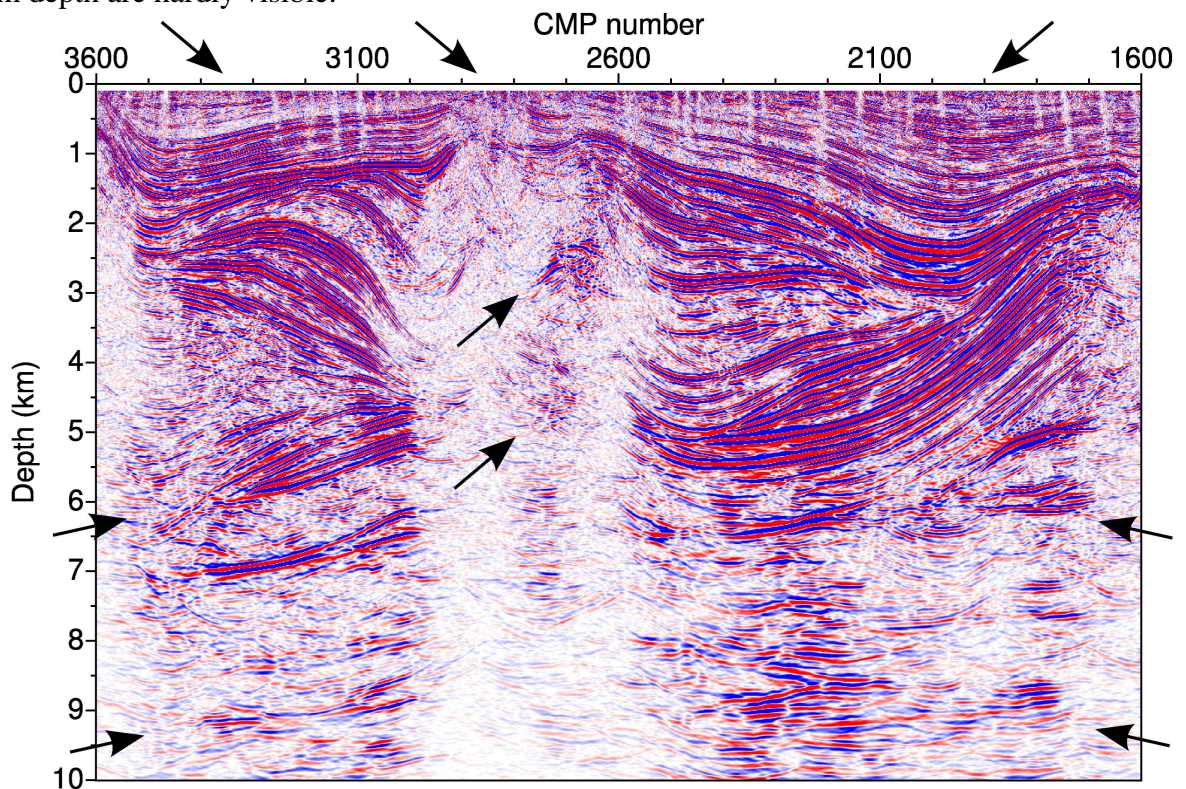


Figure 4.17: Land data: PreSDM section of CRS supergathers in the salt plug area. The image quality is significantly enhanced compared to Figure 4.16. The horizons are more continuous and the S/N ratio is enhanced. Internal salt reflectors between 2600 and 2800 CMP at 2-6 km depth are clearly visible. Also, the images of the sub-salt areas of the section below 7 km are improved. The areas of improvement are shown with the black arrows.

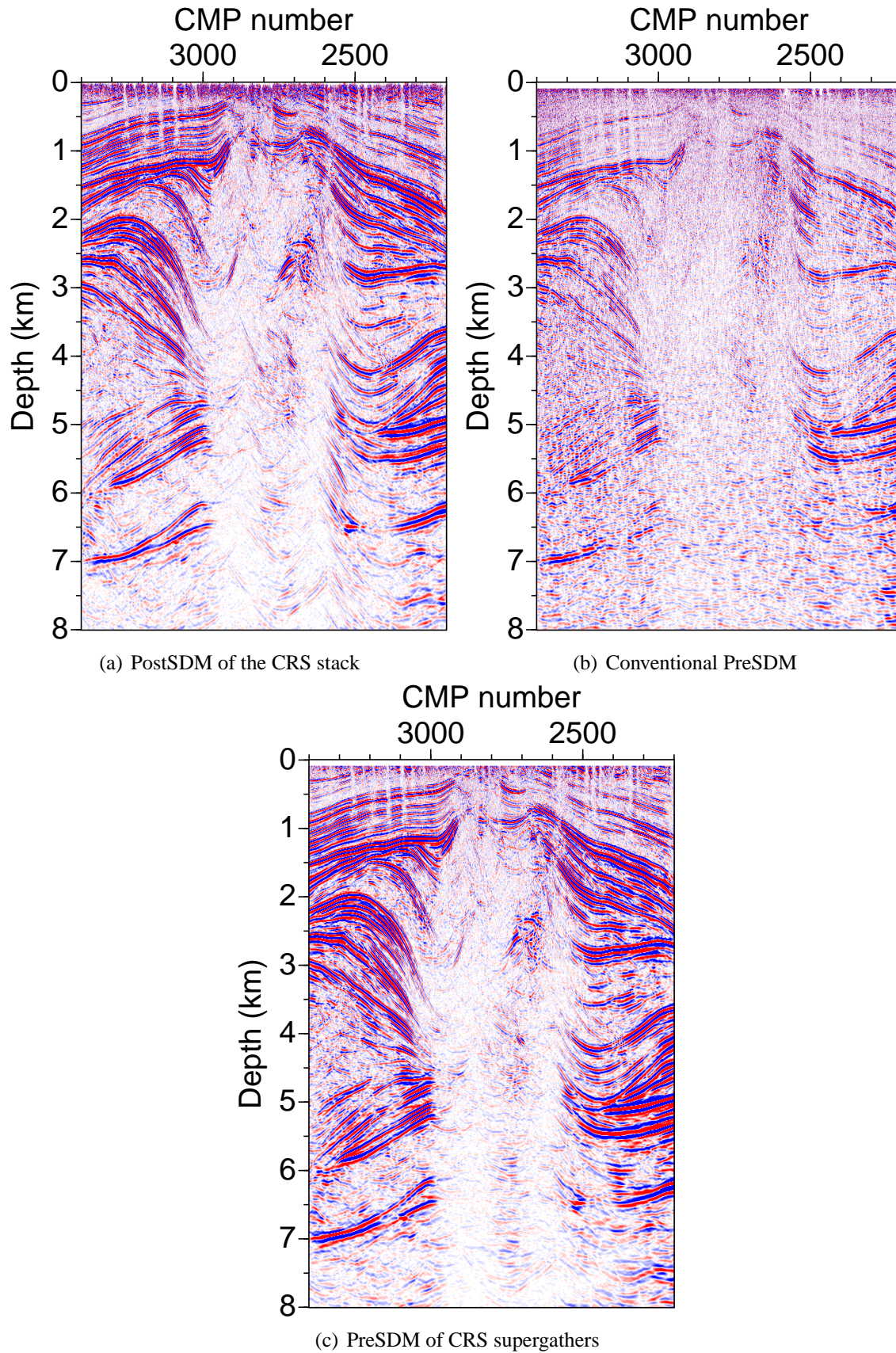


Figure 4.18: Land data: comparison of depth migrated sections in the salt-rich area. Whereas the quality of the conventional PreSDM section (b) is low, the PreSDM of CRS supergathers (c) produced an image with a quality comparable to the PostSDM of the CRS stack (a).

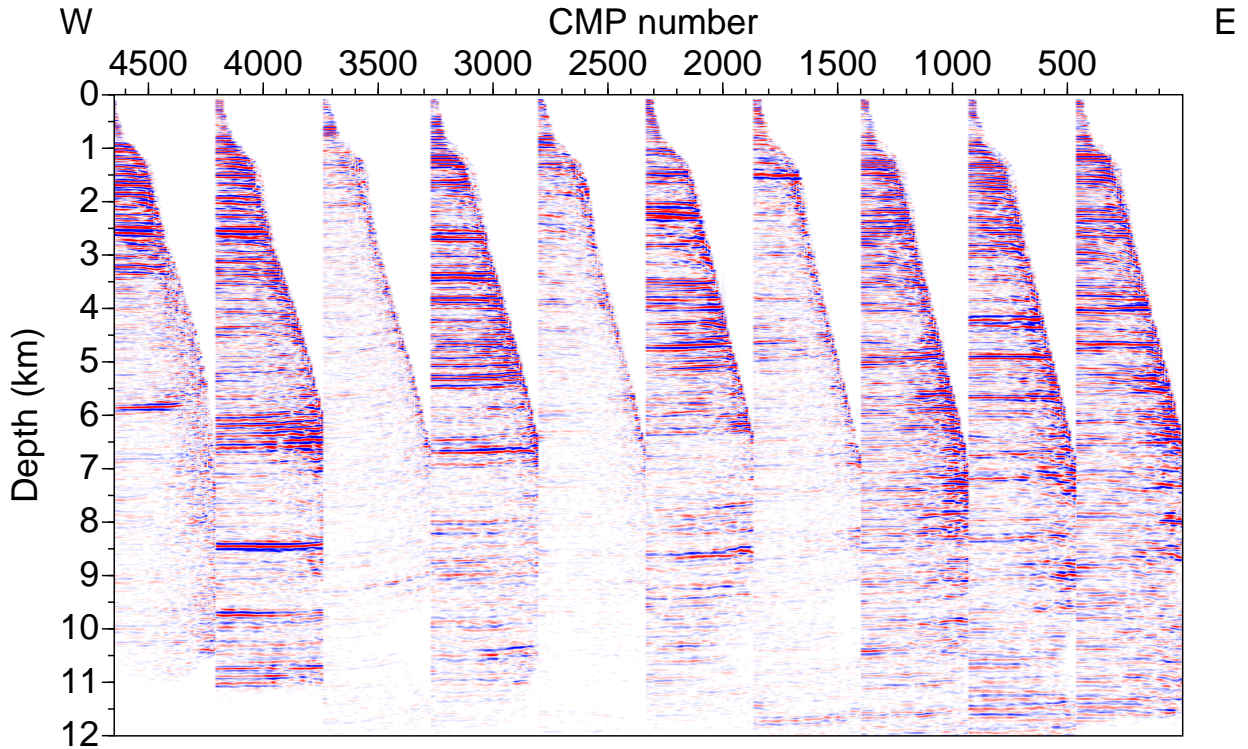


Figure 4.19: Land data: CIGs of CRS supergathers. The image quality is significantly enhanced compared to the conventional CIGs as presented in Figure 3.20. The gathers are flat almost everywhere. Only the CIG 3600, located close to the salt-sedimentary boundary, shows residual moveout at 8.5 to 10 km depth.

4.5 Discussion and Conclusion

The developed partial CRS stack technique has shown the potential to enhance the quality of 2D prestack seismic data. The program generates new regularised gathers of higher quality. In this study, the method was successfully implemented and applied to 2D synthetic data and to low-fold land data. The synthetic examples confirm potential of the method to increase the S/N ratio of seismograms and the regularity of traces. The sparse land data were regularised and the S/N ratio of seismograms was increased. Prestack depth migrated CRS supergathers of land data allowed a reliable quality control of the velocity model used for migration, which was not possible after conventional processing. The new depth migrated images of improved quality may be useful as a supplementary information for better geological interpretation.

Similar to the CRS stack, the partial CRS stack takes the information from conflicting dips into account. To use this option the proper CRS parameter set must be estimated. This results in a number of different stacking surfaces for one sample of seismic data. The automatic search of CRS parameters for conflicting dips is already implemented in 2D and can be applied for partial

CRS stacks.

The usage of partially stacked CRS supergathers instead of conventional CMPs in seismic processing is advantageous especially for sparse data of low quality. Results of velocity analysis, stacking and depth migration may be improved using the gathers generated by the new approach. The new gathers can also be useful for the optimisation of the CRS parameter search. The improved CRS parameter sets will probably provide a basis for stable NIP-wave tomographic inversion. Finally, the CRS supergathers may also contribute to improve multiple attenuation techniques, as used by [Dümmong and Gajewski \(2008\)](#).

Compared to the conventional CMP stack, the CRS stack in general requires more CPU time. For example, the automatic CMP stack of the real land data used in this work took about 10 min, whereas the CRS stacking needed about 10 hours to complete when one CPU with 2.6 GHz and 1 GB RAM was used. More significant is the CPU time needed to estimate the CRS parameters, which took more than 10 days on the hardware mentioned above. The computation time, however, may vary depending on the apertures used by the CRS parameter search, the number of conflicting dips, and other factors. Much more difficult is to estimate the time that a user needs for testing the apertures, thresholds etc. Nevertheless, the CRS stack is an automatic approach that needs only minor human interaction, if the processing parameters are known for the dataset. In this case, the total time costs might be even less than the turnaround time of the conventional CMP processing. The partial CRS stack of the land dataset took about 30 hours, which is fast compared to the CRS parameter search. It is important to mention that the CRS stack is an independent process for each sample and is well suited for parallelisation. Using a computer cluster (a group of processors) the computation time for the CRS parameter search and the partial CRS stack can be significantly reduced. Due to the independence of each time sample, no communication of nodes is required. The decrease of CPU time should scale almost linearly with the number of nodes on a parallel system.

Chapter 5

Summary and Outlook

5.1 Summary

The CRS stack used in this work allows to enhance the quality of poststack and prestack seismic reflection data in complex geological settings. Due to the increased number of traces used by stacking in comparison to the conventional CMP stack, the resulting CRS stack sections have a higher S/N ratio, thus providing clearer images of the subsurface. Moreover, information about the shape of seismic reflectors, i.e., dip and curvature, is taken into account by the CRS stack, further improving stacking results. Especially in the areas of complex salt tectonics with the presence of steeply dipping layers the CRS stack provides more detailed images of the geological structure than the conventional CMP stack method. Additional benefit of the method is that the stacking and velocity model building is carried out in an automatic mode with moderate human interaction. The CRS stack allows to perform a complete processing workflow that starts with generating an automatically stacked CMP section and ends with prestack depth migration of partially stacked CRS supergathers.

The results of the CRS stack processing applied to two datasets from Northern Germany and from the North Sea provided supplementary information for further interpretation of the data. Neither depth velocity model nor depth migrated sections of the land data presented in this work were so far available. The reprocessing of old low-fold data with the CRS stack method outlined new features not identified before. The presented results may lead to a new view of the geological understanding of the region. The resulting time and depth images partly contributed to the special project of the German Research Foundation SPP 1135 "Dynamics of Sedimentary Systems".

The *partial CRS stack* developed in this work allows to generate prestack seismic data of better

quality than the original CMP gathers. The method uses the CRS traveltime formula for partially stacking the seismograms without the application of the normal moveout (NMO) correction. As a result, partially stacked CRS supergathers of higher S/N ratio are obtained. Moreover, the method allows to regularise irregularly-acquired data. Partial stacking fills in missing traces and creates seismograms which are equally spaced. Partially stacked CRS supergathers can be used in conventional processing like velocity analysis or migration instead of the original data. The partial CRS stack method allows to enhance seismic events that were not recognisable in original low-quality data.

The partial CRS stack method was tested on a synthetic dataset for sparse and noisy data. For sparse data, the partial CRS stack filled in the missing offsets in an exemplarily-chosen CMP gather with the information from neighbouring CMPs. The resulting gather showed parts of reflections which were not visible in the input CMP gather. The second synthetic example demonstrated the possibility of the partial CRS stack to improve the S/N ratio of seismograms. Gaussian noise was added to the seismic traces until the reflections became almost not visible. In the generated CRS supergather these reflections could again be easily identified.

The partial CRS stack method was then applied to low-fold land data in order to improve the quality of the prestack depth migrated gathers. First, the partially-stacked CRS supergathers were generated. The result showed greatly improved prestack data of higher S/N ratio, where continuous reflections were clearly visible. Then, the improved data were depth migrated using the velocity model derived from the original data. Reflectors in the depth migrated CRS supergathers are clearly visible and almost horizontal at all depth levels. The latter confirms that the depth velocity model used by migration is consistent with the data, and that the results of migration can be used for geological interpretation. Reliable quality control of the migration result was so far not possible using the original data. The prestack depth migrated section obtained from the CRS supergathers has higher S/N ratio than the conventional PreSDM section, and the reflectors appear more continuous, supporting further geological interpretation.

5.2 Outlook

The partial CRS stack method based on the CRS traveltime formula provides a hyperbolic approximation of the reflection response. Therefore, the apertures of stacking in both offset and midpoint directions must be chosen carefully with respect to the complexity of the subsurface. However, the developed search algorithm allows to find the best fit hyperbolic formula for the non-hyperbolic events as well. I suppose, therefore, that the robust summation in the midpoint direction used to generate the supergathers would produce reliable results also for non-hyperbolic events. This point, however, needs further investigations. Also, the conflicting dip problem indicated in the discussion of partial CRS stack method may be the target of future work.

Since the partial CRS stack performs summation of data, amplitude variation with offset is not taken into account. However, by means of the CRS parameters it is possible to estimate the geometrical spreading factor required in true amplitude imaging. The application of the CRS stack for improved AVO analysis has already been presented by [Pruessmann et al. \(2004\)](#). Preservation of amplitudes in the partial stacks will be addressed in future work efforts.

Here, the method was implemented for the 2D case only. The first examples of the 3D CRS stack on real 3D land data were presented by [Bergler et al. \(2002\)](#). They indicated some of the possible applications of the kinematic wavefront attributes estimated during the 3D CRS stack. Beyond the outlined applications, the partial CRS stacking surface can be computed for the 3D data as well, which is the aim of further investigations. Interpolation of data in missing CMP locations might be useful in the 3D case. The parallelisation of the software and the application of the partial CRS stack on 3D data are important targets of further work.

Used software

In the course of this thesis several computers running the free GNU/Linux operation system were used.

The partial CRS stack method developed during this work was written in C++. The program is based on the 2D ZO CRS stack code as implemented by [Mann \(2002\)](#).

For simple processing and visualisation of the data, the free Seismic Un*x (SU) package was used. Additional figures were generated using gnuplot, inkscape and gimp. Preprocessing of the seismic data was carried out with Paradigm FOCUS software. Poststack and prestack depth migrations were performed using ProMAX of Halliburton.

The Wave Inversion Technology (WIT) consortium provided further software for the CRS processing:

- 2D ZO CRS stack (implemented by Jürgen Mann)
- Automatic picking of input data for tomographic inversion (by Tilman Klüver)
- 2D NIP-wave tomography (by Eric Duveneck)

The thesis itself was written on a PC with the free operating system Debian GNU/Linux with the typesetting system \LaTeX .

Acknowledgements

I am grateful to **Prof. Dr. Dirk Gajewski** for the supervision of this work and for help in any kind of occurring questions and problems. He gave me the opportunity to study in the Institute of Geophysics at the University of Hamburg, which I really enjoy.

Many thanks to **Dr. Claudia Vanelle** for the help concerning the full range of theoretical and technical questions. Special thank for the proofreading of this thesis.

I gratefully acknowledge the enthusiasm of **Dr. Heinz-Jürgen Brink** during the collaborative work within the project SPP 1135 "Dynamics of Sedimentary Systems". His competence in the geological structure of Northern Germany and steady interest for new processing results helped me many times during the work. I also thank **Dr. Yuriy Maystrenko** and other members of the GFZ working group (Potsdam) for interesting discussions during the SPP 1135 meetings.

I would like to thank following colleagues and students of the Institute of Geophysics, University of Hamburg, who contributed to this study:

- **Dr. Axel Ehrhardt** and **Lea Scharff** gave me a quick and effective introduction in seismic processing with the FOCUS software.
- **Dr. habil. Christian Hübscher** and **Dr. Ekkehart Teßmer** were always ready to help with diverse problems occurred during the study. Their support in computer administration, licenses updates, seismic processing and interpretation are appreciated.
- I thank **Dr. Mi-Kyung Yoon** for helpful advice and suggestions in the course of the study, and for the proofreading of the thesis. Her constructive criticism helped me a lot to improve the results of the work.
- Discussions with **Stefan Dümmer** were always interesting and fruitful. He gave me many useful ideas and provided a lot of codes and scripts used in this thesis. His competence in the CRS processing and his assistance were very helpful for me during the study.

- My special thanks go to **Christel Mynarik** for the assistance in administration. Her steady optimism and good mood bring me every time some more energy for working.

I enjoyed the friendship with **André Koopmann**, **Manuel Beitz** and **Maja Tisljar** very much. We had a great time working together in the Institute of Geophysics, and playing kicker in free time. I hope, we will see each other again in "Haus 73".

The synthetic dataset for numerical tests was kindly provided by the **SMAART JV** consortium. The marine data is the property of **BP**. I thank **Lutz Lüdenbach** and **Ulrich Georg** (RWE Dea, Hamburg) for the assistance with the processing of the marine data. The real land data were kindly provided by **WEG** through the technical management of the German Society for Petroleum and Coal Science and Technology (**DGMK**). Many thanks to **Paul Krajewski** for the help with the datasets.

The WIT consortium provided a lot of CRS software used in this study, including the automatic CRS stack and NIP-wave tomography. Many thanks to **Dr. Jürgen Mann**, **Dr. Tilman Klüver**, and other members of the University of Karlsruhe for the assistance with the program codes.

I would like to thank **GNU/Linux** and **Debian** projects for the amazing variety of free software, and for the interesting reading of the manuals.

I gratefully acknowledge the **University of Hamburg**, the Wave Inversion Technology (**WIT**) consortium, and the German Research Foundation (**DFG**) for the financial support during the study.

Finally, I thank my wife **Kerstin Metzler** and our daughter **Nicole** for their patience and support. I am grateful to the parents of Kerstin, **Josefina** and **Alex Metzler**, for the enormous help during the period of my study.

References

- Bayer, U., Gajewski, D., and Littke, R. (2008). Sedimentary basin evolution: subsidence, salt dynamics, fluid flow and deformation. *Int J Earth Sci.* DOI:10.1007/s00531-008-0300-9.
- Baykulov, M., Brink, H.-J., Gajewski, D., and Yoon, M.-K. (2009). Revisiting the structural setting of the Glueckstadt Graben salt stock family, North German Basin. *Tectonophysics*, 470:162–172. DOI:10.1016/j.tecto.2008.05.027.
- Baykulov, M. and Gajewski, D. (2008). Seismic data enhancement with Common Reflection Surface (CRS) stack method. *Soc. Expl. Geophys. Expanded Abstracts*. DOI:10.1190/1.3063882.
- Baykulov, M. and Gajewski, D. (2009). Prestack seismic data enhancement with partial Common Reflection Surface (CRS) stack. *Geophysics*. In press.
- Bergler, S., Hubral, P., Marchetti, P., Cristini, A., and Cardone, G. (2002). 3D common-reflection-surface stack and kinematic wavefield attributes. *The Leading Edge*, 21:1010–1015. DOI:10.1190/1.1518438.
- Berkovitch, A., Belfer, I., and Landa, E. (2008). Multifocusing as a method of improving sub-surface imaging. *The Leading Edge*, 27:250–256. DOI:10.1190/1.2840374.
- Bleistein, N., Cohen, J., and Stockwell, J. (2000). *Mathematics of Multidimensional Seismic Imaging, Migration, and Inversion*. Springer.
- Brink, H.-J. (1984). Die Salzstockverteilung in Nordwestdeutschland. *Geowissenschaften in unserer Zeit*, 2. Jahrgang, 5:160–166.
- Brink, H.-J. (1986). Salzwirbel im Untergrund Norddeutschlands. *Geowissenschaften in unserer Zeit*, 4. Jahrgang, 3:81–86.
- Brink, H.-J. (1987). Salzwirbel oder instabile Dichtebeschichtung? *Geowissenschaften in unserer Zeit*, 5. Jahrgang, 4:144–145.
- Brink, H.-J., Dürschner, H., and Trappe, H. (1992). Some Aspects of the Late- and Post-Variscan Development of the NW-German Basin. *Tectonophysics*, 207:65–95. DOI:10.1016/0040-1951(92)90472-I.

- Brune, R. H., O'Sullivan, B., and Lu, L. (1994). Comprehensive analysis of marine 3-D bin coverage. *The Leading Edge*, 13:757–762. DOI:10.1190/1.1437034.
- Červený, V. (2001). *Seismic ray theory*. Cambridge University press.
- Chandola, S. K., Singh, V., Saha, A., Sarma, P. L. N., Rao, M. P., and Ramakrishna, K. (2004). Seismic surveying in an urban setting. *The Leading Edge*, 23:1078–1082. DOI:10.1190/1.1813356.
- Coman, R. and Gajewski, D. (2001). Estimation of multivalued arrivals in 3-D models using wavefront ray tracing. *Soc. Expl. Geophys. Expanded Abstracts*. DOI:10.1190/1.1816324.
- Dümmong, S. and Gajewski, D. (2008). A multiple suppression method via CRS attributes. *Soc. Expl. Geophys. Expanded Abstracts*. DOI:10.1190/1.3063869.
- Duveneck, E. (2004). Velocity model estimation with data-derived wavefront attributes. *Geophysics*, 69:265–274. DOI:10.1190/1.1649394.
- Eisenberg-Klein, G., Pruessmann, J., Gierse, G., and Trappe, H. (2008). Noise reduction in 2D and 3D seismic imaging by the CRS method. *The Leading Edge*, 27:258–265. DOI:10.1190/1.2840375.
- Ettrich, N. and Gajewski, D. (1998). Traveltime computation by perturbation with FD-eikonal solvers in isotropic and weakly anisotropic media. *Geophysics*, 63:1066–1078. DOI:10.1190/1.1444385.
- Fomel, S. (2003). Seismic reflection data interpolation with differential offset and shot continuation. *Geophysics*, 68:733–744. DOI:10.1190/1.1567243.
- Gurevich, B. and Landa, E. (2002). Multifocusing imaging with controlled reflection-point dispersal. *Geophysics*, 67:1586–1592. DOI:10.1190/1.1512804.
- Herrmann, F. J., Wang, D., Hennenfent, G., and Moghaddam, P. P. (2008). Curvelet-based seismic data processing: A multiscale and nonlinear approach. *Geophysics*, 73:A1–A5. DOI:10.1190/1.2799517s.
- Heye, D. (1978). Experimente mit viskosen Flüssigkeiten zur Nachahmung von Salzstrukturen. *Geol. Jb.*, E12:31–51.
- Hoffmann, N., Jödicke, H., and Horejschi, L. (2005). Regional Distribution of the Lower Carboniferous Culm and Carboniferous Limestone Facies in the North German Basin - Derived from Magnetotelluric Soundings. *Z. dt. Ges. Geowiss.*, 156/2:323–339.
- Hubral, P. (1983). Computing true amplitude reflections in a laterally inhomogeneous earth. *Geophysics*, 48:1051–1062. DOI:10.1190/1.1441528.
- Hubral, P. and Krey, T. (1980). *Interval velocities from seismic reflection traveltime measurements*. Soc. Expl. Geophys.

- Hudec, M. and Jackson, M. (2007). Terra infirma: Understanding salt tectonics. *Earth Science Reviews*, 82:1–28.
- Hunsche, U. (1978). Modellrechnungen zur Entstehung von Salzstockfamilien. *Geol. Jb.*, E12:53–107.
- Jäger, R., Mann, J., Höcht, G., and Hubral, P. (2001). Common-reflection-surface stack: Image and attributes. *Geophysics*, 66:97–109. DOI:10.1190/1.1444927.
- Jaritz, W. (1973). Zur Entstehung der Salzstrukturen Nordwestdeutschlands. *Geol. Jb.*, A10:3–77.
- Landa, E., Gurevich, B., Keydar, S., and Trachtman, P. (1999). Application of multifocusing method for subsurface imaging. *Journal of Applied Geophysics*, 42, 3-4:283–300. DOI:10.1016/S0926-9851(99)00041-5.
- Loewenthal, D., Roberson, R., Sherwood, J., and Lu, L. (1976). The wave equation applied to migration. *Geophysical Prospecting*, 24:380 – 399. DOI:10.1111/j.1365-2478.1976.tb00934.x.
- Mann, J. (2002). *Extensions and Applications of the Common-Reflection-Surface Stack Method*. PhD thesis, University of Karlsruhe.
- Mayne, W. H. (1962). Common reflection point horizontal data stacking techniques. *Geophysics*, 27:927–938. DOI:10.1190/1.1439118.
- Maystrenko, Y., Bayer, U., and Scheck-Wenderoth, M. (2005). Structure and evolution of the Glueckstadt Graben due to salt movements. *Int J Earth Sci*, 94:799–814. DOI:10.1007/s00531-005-0003-4.
- Mohr, M., Kukla, P. A., Urai, J. L., and Bresser, G. (2005). Multiphase salt tectonic evolution in NW Germany: seismic interpretation and retro-deformation. *Int J Earth Sci*, 94:917–940. DOI:10.1007/s00531-005-0039-5.
- Müller, T. (1999). *The Common Reflection Surface Stack Method: Seismic Imaging without explicit knowledge of the velocity model*. PhD thesis, University of Karlsruhe.
- Pruessmann, J., Coman, R., Endres, H., and Trappe, H. (2004). Improved imaging and AVO analysis of a shallow gas reservoir by CRS. *The Leading Edge*, 23:915–918. DOI:10.1190/1.1803503.
- Pruessmann, J., Frehers, S., Ballesteros, R., Caballero, A., and Clemente, G. (2008). CRS-based depth model building and imaging of 3D seismic data from the Gulf of Mexico Coast. *Geophysics*, 73:VE303–VE311. DOI:10.1190/1.2968691.
- Reshef, M. and Kosloff, D. (1986). Migration of common shot gathers. *Geophysics*, 51:324–331. DOI:10.1190/1.1442091.

- Sannemann, D. (1968). Salt-stock families in northwestern Germany. In Braunstein, J. and O'Brein, G. D. (eds) Diapirism and Diapirs. *American Association of Petroleum Geologists, Tulsa, Memoir*, 8:261–270.
- Schleicher, J., Hubral, P., Tygel, M., and Jaya, M. S. (1997). Minimum apertures and Fresnel zones in migration and demigration. *Geophysics*, 62:183–194. DOI:10.1190/1.1444118.
- Schleicher, J., Tygel, M., and Hubral, P. (1993). 3-D true-amplitude finite-offset migration. *Geophysics*, 58:1112–1126. DOI:10.1190/1.1443495.
- Schneider, W. A. (1978). Integral formulation for migration in two and three dimensions. *Geophysics*, 43:49–76. DOI:10.1190/1.1440828.
- Sheriff, R. E. and Geldart, L. P. (1995). *Exploration Seismology, 2nd edition*. Cambridge University Press.
- Spitzer, R., Nitsche, F. O., Green, A. G., and Horstmeyer, H. (2003). Efficient acquisition, processing, and interpretation strategy for shallow 3D seismic surveying: A Case Study. *Geophysics*, 68:1792–1806. DOI:10.1190/1.1635032.
- Stolt, R. H. (2002). Seismic data mapping and reconstruction. *Geophysics*, 67:890–908. DOI:10.1190/1.1484532.
- Stolt, R. H. and Benson, A. K. (2001). *Seismic migration. Theory and practice*. Geophysical press.
- Trusheim, F. (1957). Über Halokinese und ihre Bedeutung für die strukturelle Entwicklung Norddeutschlands. *Z. Dtsch. Geol. Ges.*, 109:111–151.
- Vanelle, C., Spinner, M., Hertweck, T., Jäger, C., and Gajewski, D. (2006). Traveltime-based true-amplitude migration. *Geophysics*, 71:S251–S259. DOI:10.1190/1.2356091.
- Vinje, V., Iversen, E., and Gjøystdal, H. (1993). Traveltime and amplitude estimation using wavefront construction. *Geophysics*, 58:1157–1166. DOI:10.1190/1.1443499.
- Yilmaz, O. (2001). *Seismic data analysis - Processing, inversion, and interpretation of seismic data*. Soc. Expl. Geophys.
- Yoon, M.-K., Baykulov, M., Dümmong, S., Brink, H.-J., and Gajewski, D. (2008a). New insights into the crustal structure of the North German Basin from reprocessing of seismic reflection data using the Common Reflection Surface stack. *Int J Earth Sci*. DOI:10.1007/s00531-007-0252-5.
- Yoon, M.-K., Baykulov, M., Dümmong, S., Brink, H.-J., and Gajewski, D. (2008b). Reprocessing of deep seismic reflection data from the North German Basin with the Common Reflection Surface stack. *Tectonophysics*. DOI:10.1016/j.tecto.2008.05.010.
- Ziegler, P. (1990). *Geological Atlas of Western and Central Europe, 2nd edition*. Shell, The Hague.

Erklärung

Hiermit versichere ich, die vorliegende Arbeit selbstständig angefertigt und nur die angegebenen Hilfsmittel verwendet zu haben.

Diese Arbeit hat in gleicher oder ähnlicher Form noch keiner Prüfungsbehörde vorgelegen.

Der Veröffentlichung in der Bibliothek stimme ich zu.

Hamburg, den 6. Mai 2009.

Personal details

Name	Mikhail Baykulov
Date of Birth	24.03.1980
Place of Birth	Saratov, Russia
Nationality	Russian
Email	mikhail.baykulov@zmaw.de

Education

1987 – 1993	Elementary school, Russia
1993 – 1997	Lyceum of Applied Sciences, Saratov
July 1997	Graduation (school leaving certificate)
1997 – 2000	Study of Physics, Saratov State University
2000 – 2004	Study of Geophysics, Saratov State University
May 2004	Graduation (Diploma) at Saratov State University. The Diploma thesis concerned techniques of velocity model building and depth imaging of seismic data
October 2004 – March 2005	Study of Geophysics, University of Hamburg
April 2005 – May 2009	PhD Study in Geophysics, University of Hamburg

**Scientific interests
and experiences**

Applied geophysics: seismic data processing,
inversion, reflection tomography, depth migration

Languages

English (fluent),
German (fluent),
Russian (native language)